Kim Lynge Sørensen

Autonomous Icing Protection Solution for Small Unmanned Aircraft

An Icing Detection, Anti-Icing and De-Icing Solution

Kim Lynge Sørensen

Doctoral Thesis

Doctoral theses at NTNU, 2016:275

NTNU
Norwegian University of
Science and Technology
Faculty of Information Technology,
Mathematics and Electrical Engineering
Department of Engineering Cybernetics

NTNU
Norwegian University of
Science and Technology

NTNU

NTNU
Norwegian University of
Science and Technology

Kim Lynge Sørensen

Autonomous Icing Protection Solution for Small Unmanned Aircraft

An Icing Detection, Anti-Icing and De-Icing Solution

Thesis for the degree of Philosophiae Doctor

Trondheim, September 2016

Norwegian University of Science and Technology
Faculty of Information Technology,
Mathematics and Electrical Engineering
Department of Engineering Cybernetics

NTNU
Norwegian University of
Science and Technology

To my family

Summary

This monograph is motivated by the lack of an autonomous icing protection solution for small unmanned aerial vehicles.

The atmospheric phenomenon commonly referred to as aircraft icing is one the most dangerous weather hazards to all of aviation. When an aircraft operates in atmospheric conditions that sustain icing, a potential of ice forming on exposed aircraft surfaces arises. The most significant of these surfaces are the leading edge of aircraft wings, stabilisers, and various control surfaces. This monograph focusses on icing as it forms on the leading edge of wings. The consequences of icing range from insignificant to dire, even fatal. For unmanned aerial vehicles, as is the case for conventional aircraft, the impact of icing primarily relates to controllability of the aircraft. Once icing forms on the wings the aerodynamic shape is altered. Typically this leads to changes in the aerodynamic characteristics of the wing, i.e. maximum lift can decrease by as much as 80% and drag can increase by more than 60%.

For small unmanned aerial vehicles there are no commercially available icing mitigating solutions, aside from grounded operations. This monograph is a presentation of just such a solution. The icing protection solution is based on three primary elements, 1) an electro-thermal source, 2) an intelligent control unit, and 3) a power source. In essence the solution provides according to the following; the control unit is primed by an on-board atmospheric sensor package, measuring ambient environmental conditions. Once the risk of icing is established, two ice detection algorithms - working in parallel - are activated. This approach ensures robustness and accuracy. If icing is detected, control algorithms trigger the power supplied to the electro-thermal source, thereby achieving temperature control of the thermal source.

For conventional aircraft, icing detection is usually performed by larger optical sensors or a pilots visual inspection. For UAVs icing detection is a relatively new research topic. In this monograph two markedly different approaches to icing detection for UAVs are proposed. Common for both is the objective of detecting icing as it forms on the leading edge of aircraft wings.

One icing protection solution presented in this monograph is denoted the *model-based icing detection algorithm*. It addresses the issue in a fault diagnosis framework by generating residuals used to detect aircraft surface faults (that is aerodynamic changes), indicating that icing is forming on the leading edge of the aircraft wings. The proposed algorithm relies on estimates of aerodynamic parameters - obtained under nominal flight conditions - and the aerodynamic model of the aircraft. Should these parameters change unexpectedly a surface fault has occurred, i.e. icing is

forming on the wings of the aircraft. The proposed algorithm has been validated through numerical analyses.

The second icing detection algorithm proposed is denoted the *electro-thermal-based icing detection algorithm*. It also addresses the issue of icing detection in a fault diagnosis framework, but where the prior algorithm uses the aerodynamic model of the aircraft to accomplish this, the latter algorithm applies a model of the thermodynamic system surrounding the aircraft wings and the electro-thermal source. The electro-thermal-based icing detection algorithm uses temperature gradients, obtained from the electro-thermal source, and unexpected changes in these to detect changes in the thermodynamic system. A change could be an added element as a layer of ice. The proposed approach has been validated through a simulation study.

To evaluate the electro-thermal source layout and area size, several thermodynamic analyses are conducted. Simulations are conducted to determine the relationship between area size and power consumption, while responses from other simulations are used to investigate and evaluate the thermal distribution differences of electro-thermal sources applied to various UAV platforms.

To demonstrate the feasibility of the proposed icing detection solution wind tunnel experiments and flight tests have been conducted. Preliminary integration procedures are developed to ensure little to no negative aerodynamic impact, while abiding by requirements for airworthiness and safe flight operations.

Wind icing tunnel experiments have been conducted for various required icing protection program routines, i.e. icing detection, de-icing, and anti-icing. Experiments have been conducted in atmospheric conditions ranging from non-icing to varying severity degrees of icing.

Preliminary flights include the worlds first flight for any UAV fitted with an autonomous icing protection solution, completed in a collaboration between NTNU-AMOS and NASA Ames Research Center and conducted in Anchorage, Alaska.

Operational flights have been conducted at Ny-Ålesund, Svalbard, where the aforementioned icing protection program routines have been tested, verifying the icing protection solution.

Contents

List of figures

List of tables

Preface

This monograph is submitted in partial fulfilment of the requirements for the degree of philosophiae doctor (Ph.D.) at the Norwegian University of Science and Technology (NTNU).

The work presented herein has been completed at the centre for Autonomous Marine Operations and Systems (AMOS), department of engineering cybernetics, in the period June 2013 to July 2016. My supervisors have been Professor Tor Arne Johansen of NTNU-AMOS , and Professor Mogens Blanke of the Technical University of Denmark (DTU).

During my Ph.D. studies I had the privilege of working as a visiting researcher at NASA Ames Research Center under the supervision of Matthew Fladeland, chief of operations at the Airborne Science Division, NASA Ames Research Center, Moffet Field, Mountain View, California, United States. This research stay has had a tremendous impact on the development I have experienced both personally and professionally.

Acknowledgements

Attaining the degree of Ph.D. is generally considered a life in solitude. However, my experience has - most of the time - been the contrary. Therefore, I have a ridiculous amount of people I feel gratitude towards that have in one way or another contributed to me finishing my monograph and obtaining the title of "doctor" (don't call on me if you have a heart attack).

While I will thank a lot of people in the following, there are most likely some I will forget. To them, I extend my sincerest apologies.

First, I would especially like to thank my supervisor Professor Tor Arne Johansen. You are without a doubt the smartest person I have ever met. You are

capable of pushing, encouraging, and inspiring me to achieve things I never thought possible. I look forward to continuing and expanding our collaboration.

I would like to thank my co-supervisor Professor Mogens Blanke from the department of Electrical Engineering at the Technical University of Denmark (DTU). For his advice and support, prior and during my Ph.D. studies. Thank you for pointing me in the direction of Ph.D. studies at NTNU. It has changed my life for the better.

I also need to thank my former Masters supervisor Associate Professor Roberto Galeazzi from the department of Electrical Engineering at DTU. You were the first to ever show me what hard work really is, and that it could get me further than I thought possible. Your guidance, insight, and revelations are a cornerstone of the mindset that has taken me towards the career path I am pursuing.

Phil McGillivary, Science Liaison at the U.S. Coast Guard PACAREA, Department of Homeland Security. I need to thank you for your advice, encouragement, and of course your constant flow of emails; the root of many interesting mutual ideas and solutions.

I would like to convey my deepest gratitude to Matthew Fladeland, chief of operations at the Airborne Science Division, NASA Ames Research Center. You made me feel welcome and at home when I visited Ames, and now you are a constant source of encouragement and advice, as we together pursue common objectives.

I am bound to express my deepest and sincerest gratitude to the permanent staff of of the department of Engineering Cybernetics. They need to be named, because I am confident that without their help, I would not be here, writing a preface as the final contribution to this monograph. Eva Amdahl, Unni Johansen, Janne Karin Hagen, and Anne Sofie Kvål, Stefano Bertelli, Jan Leistad, Åsmund Stavdahl, and Gunnar Aske. Your help, can-do spirits, and positive attitudes are what shines the brightest in the highly successful department that is the Engineering Cybernetics department of NTNU. In the same group of people I have someone that require special mentioning. Tove Kristin Blomset Johnsen, Bente Seem Lindquist, Terje Haugen, Glenn Angell, Daniel Bogen, and especially Lars Semb and Pål Kvaløy. You have had a huge positive impact on not just my time at the department, but contributed actively to me finishing my studies. I cannot thank you all enough.

I would like to thank my closest family, my parents, my sister and brothers, their families, and a few select friends, for their support and enthusiasm. Where you guys are at, I will always call home.

Tor Moe, Anita Lysgaard Moe, Solveig Lysgaard, Einar Lysgaard, and Eva Søraa Moe, my girlfriends closest family. Thank you for allowing me into the warm inner circle of your lovely family.

Second to last I need to express my deepest gratitude to my "partners in crime" Jakob Mahler Hansen and Kasper Trolle Borup, both my co-habitants of the house now knows as the 'Danish Asylum', and dear friends. You guys... It has been one of the greatest privileges of my life to go through this period along side amazing fellows such as yourselves. From frustrations to (a few) shared celebrations of triumph, you have always been their to support, assist, and share advice. My vocabulary does not hold words that will enable me to express how much this has meant to me. So I'll simply say thank you.

Finally, my fiancée, Signe Moe. You are everything to me. Friend, partner, and companion. Your support through not just my studies, but in life, has been and is exceptional. When I am down you pick me up, when I am unable to keep my feet on the ground (which rarely happens) you gracefully supply me with perspective. I would never have completed this without you. I find myself truly fortunate that our shared life is at its very beginning.

Chapter 1

List of Abbreviations

Glossery

AFSRB Airworthiness & Flight Safety Review Board
AOA Angle of Attack
CNT Carbon Nanotube
EMI Electromagnetic Interference
EPO Expanded Polyolefine
EPS Expanded Polystyrene
GLRT Generalised Likelihood Ratio Test
GNSS Global Navigation Satellite System
IMU Inertial Measurement navigations Unit
IPS Icing Protection Solution (or Icing Protection System)
LIRL LeClerc Icing Research Laboratory
LPV Linear Parameter Varying
MOSFET Metal–Oxide–Semiconductor Field-Effect Transistor
NED North-East-Down reference frame
NORUT Northern Research Institute
NRL Naval Research Laboratory
NTNU Norwegian University of Science and Technology
PCB Printed Circuit Board
PWM Pulse-Width-Modulation
RPAS Remotely Piloted Aircraft Systems
SLW Supercooled Liquid Water
SS Sideslip Angle
UAF University of Alaska Fairbanks
UAS Unmanned Aircraft System
UAV Unmanned Aerial Vehicle
VF Virtual Fuselage

Nomenclature

A Area [m^2]

α Angle-of-attack [rad]

a_x, a_y, a_z Body acceleration [m/s^2]

α_d Thermal diffusivity [m^2/s]

B Ice layer thickness [m]

β Sideslip angle [rad]

β_c Local collection efficiency

C_D, C_L Drag and Lift coefficients

c_p Specific heat capacity [J/(kg·K)]

$c_{p,w}$ Specific heat capacity of water [J/(kg·K)]

C_x and C_z Aerodynamic coefficients

δ Fluid boundary layer thickness [m]

δ_t Thermal boundary layer thickness [m]

ρ Density [kg/m^3]

ρ_∞ Density of the free airflow [kg/m^3]

ϵ Emissivity

e_0 Saturation vapour pressure constant

E Radiative energy emission [W]

$e(T)$ Evaporation function

ϕ, θ, ψ Euler angles [rad]

F_{a_x}, F_{a_y}, F_{a_z} Aerodynamic forces in the BODY frame [N]

F_t Thrust force [N]

f_x, f_y, f_z Specific force decomposed in the BODY frame [m/s^2]

g Gravitational constant [m/s^2]

h Convective heat transfer coefficient [W/(m^2·K)]

$\bar{h}$ Average convective heat transfer coefficient [W/(m^2·K)]

k Thermal conductivity [W/(m·K)]

k_f Thermal conductivity of specific fluid [W/(m·K)]

L_e Latent heat constant for evaporation [J/kg]

L_f Latent heat of fusion constant [J/kg]

L_s Latent heat constant for sublimation [J/kg]

LWC, (G) Liquid water content [g/m^3]

m Body mass [g]

MVD Median volume droplet diameter [μm]

Nu Nusselt number

ω_p Propeller angular velocity [rad/s]

Pr Prandtl number

$p,\ q,\ r$ Angular rates [rad/s]

$\dot{q}$ Heat transfer rate [W]

$\dot{Q}$ Heat flux [W/m^2]

$\dot{Q}_C$ Convective heat transfer [W/m^2]

$\dot{Q}_d$ Incomming liquid water droplet heat flux [W/m^2]

$\vec{r}$ Position vector (thermal conductivity)

r_a Adiabatic recovery factor

ρ_i Density of ice [kg/m^3]

R_n^b Rotation matrix from North-East-Down to BODY frame

Re Reynolds number

S Wing surface area [m^2]

σ Stefan Boltzmans constant $[\mathrm{W}/(\,\mathrm{m}^2\cdot K)\,]$

$S_p,\ C_p,\ k_p$ Propeller coefficients

T Temperature [K]

T_∞ Free airflow temperature [K]

ΔT Temperature difference [K]

T_{ETS} Electro-thermal source temperature [K]

T_∞ Free flow temperature [K]

∇T Temperature gradient [K/m]

T_s Surface temperature [K]

$u,\ v,\ w$ Body velocities in North-East-Down reference frame [m/s]

$u_r,\ v_r,\ w_r$ Relative body velocities in the BODY frame [m/s]

V_a Relative airspeed [m/s]

$\hat{V}_a$ Estimated relative airspeed [m/s]

V_∞ Free stream flow [m/s]

$\vec{v}_g$ Ground velocity vector [m/s]

$\vec{v}_g^b$ Ground velocity vector in Earth-fixed local North-East-Down reference frame [m/w]

$\vec{v}_r$ Relative body velocity vector in the North-East-Down frame [m/s]

ν Kinematic viscosity of a fluid [m^2/s]

$\vec{v}_w$ Wind velocity vector [m/s]

$\mathcal{X}_e$ Evaporative coefficient

$\mathcal{X}_s$ Sublimation coefficient

x_c Specific linear dimension [m]

y Distance normal to surface of specific solid [m]

Chapter 2

Introduction

This monograph represents the work conducted during the development of an icing protection solution (IPS) for small unmanned aircraft. It includes thermodynamic investigations, a full description of the developed system in its current form, experimental results, and discussions thereof.

The subsequent introduction will include background information that will motivate, illuminate, and serve as base for the work presented. The topics addressed in this introductory chapter will be; the atmospheric phenomenon known as icing; unmanned aircraft; aircraft icing protection systems; an introduction to the test beds used for the development of the present IPS prototype; the fundamental processes in thermodynamics; icing aero-thermodynamics; a listed overview of relevant publications that form the base of this document; and finally, an introduction to the structure of the remaining monograph.

2.1 Motivation

Motivation for the work presented herein is twofold; First, as a consequence of multiple factors - the primary one being technological advances - the application of small unmanned aircraft (or unmanned aerial vehicles - UAVs) is ever increasing. The requirement for robust operations necessitate intelligent solutions to one of the largest hazards to not only UAV operations, but to aviation safety itself. Second, present mitigating solutions to this hazard exist for large commercial aircraft only and these are typically heavy, structurally invasive, expensive, and environmentally harmful. The hazard itself is of course aircraft icing.

2.1.1 Icing

To fully comprehend the phenomenon of aircraft icing and its consequences, an introduction to various atmospheric phenomena is a necessity.

Contrary to common belief, droplets of liquid water in the atmosphere do not readily freeze at $0°C$, but often remain in a liquid form at colder temperatures in a 'supercooled' and unstable state. Freezing of the liquid water droplet can occur by either ice nuclei, or in a homogeneous fashion if the droplet contains no foreign

Figure 2.1: Rime ice provoke a temporary de-activation of Äppelbo wind farm (Sweden). Pictures taken from the nacelle, January 2004. Photos: Kjell Jansson, Malungs Elnät AB.

particle (i.e. the liquid water droplet is 'pure'). Homogeneous nucleation occurs at -35°C to -41°C depending on the volume of the droplet. As such homogeneous nucleation of this type exists in high altitude clouds only [3]. If the supercooled liquid water droplet is not pure, but 'polluted', it is said to freeze by heterogeneous nucleation, which typically occurs at temperature above -20°C [4]. One form of such pollution is when the droplet comes into contact with foreign objects. As such icing can occur when these droplets come into contact with man made structures such as telecommunication towers, ships, oil rigs, etc. For wind turbines icing leads to not only a reduction in harvested energy, and imposes structural fatigue, but also poses a safety risk (see Figure 2.1) [1, 5]. Much of the same is true when it comes to ice forming on power lines, as is demonstrated in Figure 2.2 [6].

Atmospheric icing affects man-made structures in many countries. Generally icing is known to occur in northern countries like Japan, Canada, United Kingdom, Iceland, Finland, Hungary, Norway, Czech Republic, Romania, Russia, etc. [6]. However, according to [7, 8] the icing phenomenon is a not confined to these parts of the World, instead it is established as a global one, with icing occurrences identified in most parts of Asia, Europe, Northern and Southern America, and even in parts of Africa.

Whether icing occurs or not naturally depends heavily on the atmospheric conditions at a given site or location.

2.1.2   Atmospheric Conditions Sustaining Icing

Generally atmospheric icing can be divided into two main categories, 1) precipitation icing, and 2) in-cloud icing. Both categories can be severely hazardous to the structures mentioned previously and aircraft.

Figure 2.2: Rime icing on a 22kW electric power line in Norway, April 1961, 1400m above sea level. The ice load was measured to 305kg/m [1].

Precipitation Icing

Precipitation icing could result in glaze ice, wet snow, or dry snow, depending on temperature variations during droplet descent. Icing of this type occurs in locations experiencing precipitation and freezing temperatures. The most relevant and hazardous to aircraft is freezing rain that typically results in glaze ice formation.

For freezing rain to occur a specific temperature distribution, as a function of altitude, is required. This distribution is in the field of meteorology denoted temperature inversion. Inversion signifies a deviation from the normal change in atmospheric properties with altitude, hence temperature inversion is the moniker used to describe the deviating temperature distribution of an increase with altitude. I.e. if the temperature at the very top of the inversion is high and the melting layer is deep then snowflakes can melt and form liquid water droplets (raindrops). When these droplets descend into a freezing layer they develop into supercooled liquid water droplets and can remain in a liquid form until they come into contact with objects in the airflow or the ground. As long as they are in the liquid state the droplets freeze more or less immediately upon impact with any object.

In-Cloud Icing

In-cloud icing can only occur within clouds that consists of supercooled liquid water (SLW) droplets, i.e. droplets that remain in a liquid state below freezing. The type of icing that forms as a result of in-cloud icing depends on various atmospheric

parameters, such as liquid water content (LWC, (G)), temperature and wind speed (perpendicular to any impinged object). Intensity and duration of in-cloud icing strongly depends on the flux of liquid water in the specific cloud, which itself is dependant on temperature, wind speed, stability, depth, height above cloud base, and distance from coastline, to name a few.

Generally, all clouds sustained at freezing temperatures have in-cloud icing potential. However, droplet distribution (i.e. LWC) and droplet size (usually quantified by the denotion median volume droplet diameter - MVD) influence ice formation. Further, the potential for in-cloud icing does not necessitate actual icing ever occurring.

Atmospheric conditions that include a high amount of large supercooled liquid water droplets induce very hazardous icing. Conversely, a lesser amount of droplets, or smaller sized droplets, favour a slower rate of icing. Smaller water droplets typically occur in fog and lower-altitude clouds. The most common type of icing found in lower-altitude stratus clouds is rime.

Cumuliform clouds are generally recognised as a cloud type that is favourable for the formation and support of many large liquid water droplets. Relating this to aircraft and aircraft icing, when entering the heavy water concentration found in cumuli clouds, the large liquid water droplets rupture and spread rapidly over exposed aircraft surfaces forming a layer of water. If temperatures are below 0°C the water layer freezes rapidly to form a solid sheet of clear ice.

2.1.3   Aircraft Icing

The potential for icing exists when there is an extended volume in the atmosphere containing SLW. Such an environment can come about in a variety of ways and is very common in the lower 10 km of the atmosphere, hence, aircraft can readily encounter icing conditions in this part of the atmosphere [9].

Unfortunately, while it is evident that icing represents one of the largest weather hazards to aviation, it is by no means trivial to forecast. It is a highly complex phenomenon whose physics is not fully understood that depends on a number of parameters, many of which have highly intricate and nonlinear relationships [9]. These have been introduced previously, but will be reiterated here for clarity. Icing severity depend heavily on air temperature and pressure, liquid water droplet size and distribution, wind speed, and finally airspeed [9–12]. While these parameters hold information on the potential icing severity related to atmospheric conditions, isolated, they reveal little of how, when, and where icing could form on an object such as an aircraft in flight.

Ice formation (or ice accretion) on an aircraft can be divided into two parts. The first part concerns the rate at which liquid water droplets impinge the exposed surfaces of the aircraft body. A body's ability to collect these water droplets is typically denoted collection efficiency and depends on liquid water droplet distribution and size, airspeed, but primarily the shape of the aircraft including incidence. The second part of ice accretion involves the rate at which the impinging liquid water droplets freeze to form icing. This part is primarily governed by the heat transfer from the surface of the aircraft, a topic addressed in a subsequent section in this introductory chapter.

As mentioned in the preceding subsection, various types of icing can form on exposed aircraft surfaces. The following is an introduction to the two primary types of aircraft icing.

When a supercooled liquid water droplet strikes the aircraft surface, part of the droplet freezes instantaneously. Thermal energy, through latent heat of fusion, is released in this phase changing process increasing the temperature of the remaining liquid part of the droplet. Other thermodynamic effects may freeze the remaining liquid water droplet, and it is the circumstances surrounding the phase change of the remaining liquid droplet that decides which type of icing forms. Clear ice accretion is typically the result of a freezing process, where the remaining liquid part of the droplet freeze gradually in to a smooth and solid layer of ice. This type of icing is generally a hazard when conducting aircraft operations in cumuli clouds with a high concentration of large liquid water droplets. Rime ice may form as the remaining liquid part of the droplet freezes rapidly trapping small air pockets within, which gives this type of icing an opaque appearance. Icing of this type typically has an irregular shape and a rough surface, with alarming consequences to the aerodynamic capabilities of the aircraft. Rime icing primarily occurs in stratus clouds, where the median volume droplet diameter of the liquid water droplets is small[13, 14]. Figures 2.3(a) and 2.3(b) illustrate clear (or glaze) icing and rime icing as it can form on an aerofoil, and Figure 2.3(c) show how clear icing can form into was is denoted horn ice accretion (i.e. severe ice formation).

Depending on atmospheric conditions a hybrid (denoted mixed icing) of the two primary types of icing can form. Mixed icing can form when the liquid water droplets vary in size or when they are intermingled with snow or ice particles, conditions found in many operational scenarios [13, 15].

A quick aside about a third type of icing. Due to various circumstances liquid water droplets can continue to run back over the wings towards the control surfaces at the rear of the wings. This type of icing is fittingly denominated runback water/icing. It is only mentioned here as side note, as it is generally not considered as hazardous as the primary icing types that form on the leading edge of the wings.

All types of icing generally form on forward facing elements of aircraft and typically on surfaces with small diameters, i.e. the leading edge of wings or stabilisers, which have been identified as the most sensitive region concerning aircraft performance degradation [16, 17]. Icing can also form on propellers, rotors, control surfaces, carburettors, exposed sensory equipment, antennas, etc. However, for the remainder if this monograph focus is limited to icing on the leading edge of aircraft wings.

2.1.4 Aircraft Icing - Consequences

Ice accretion on the leading edge of aircraft wings can have a significant negative impact on aerodynamic characteristics. The severity of this impact varies with type of icing, icing location, and aerofoil geometry. Assessing icing impact has, since the beginning of aircraft icing research, been conducted by investigating changes in aerodynamic lift and drag.

In the years prior to the second World War researchers conducted experiments, with results revealing up to a 25% reduction in maximum lift and a 90% increase in

(a) Typical rime ice accretion on wing surface. **(b)** Typical clear ice accretion on wing surface.

(c) Severe clear ice accretion on wing surface.
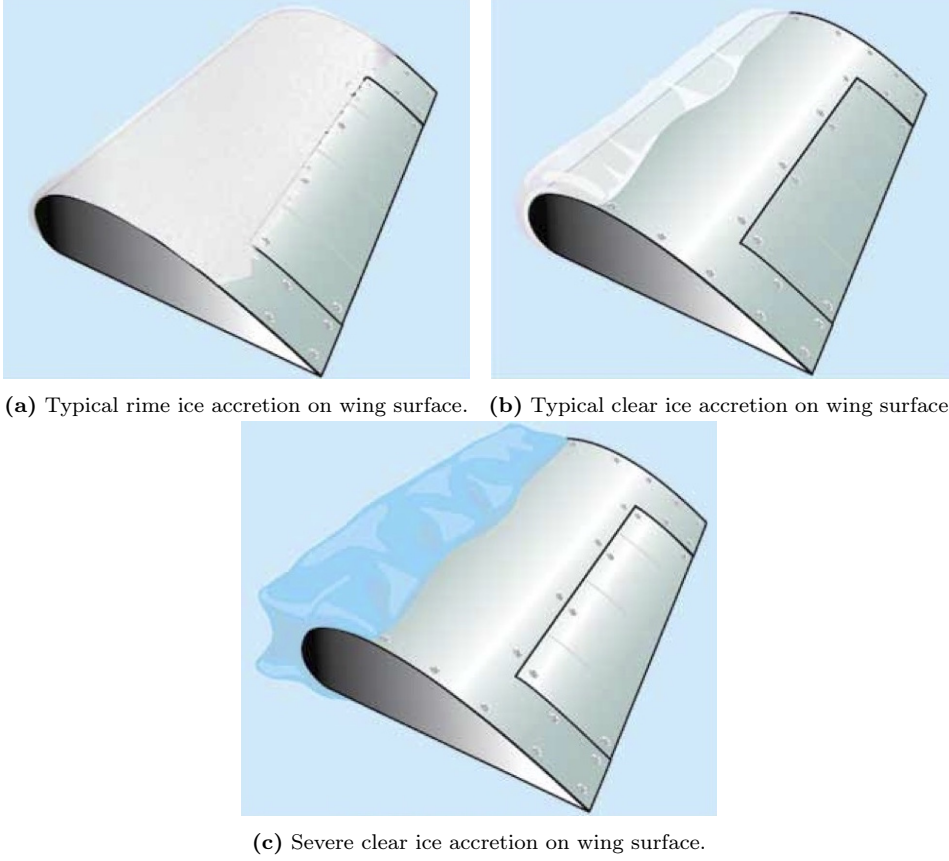
Figure 2.3: Rime icing, clear, and severe clear icing on aerofoil.

drag for a specific aerofoil geometry and icing type [18]. More recent experiments have since corroborated these early findings. Investigations performed on glaze icing in 2000 and 2001 revealed that maximum lift losses approached 60% for a specific aerofoil element, and that a *significant impact on maximum lift and stall angle was detected after 2 minutes* [19, 20]. It was also reported that initial low-Reynolds number experimental results indicated the possibility of maximum lift losses in excess of 80% for some aerofoil geometries [20]. Figure 2.4 illustrates the typical aerofoil icing penalties for lift and drag forces.

The aerodynamic consequences of icing (an increase in drag and a decrease in lift) further results in an increase in required power but a decrease in speed margin, endurance, control, fuel efficiency and rate of climb. Further, the consequences greatly influence a phenomenon known as stall. In fixed wing aviation stall is defined as a condition wherein the angle-of-attack (AOA) increases beyond a certain level such that lift begins to decrease. When leading edge icing is present the airflow around the aerofoil is disrupted, i.e. critical flow separation occurs at lower AOAs.

There is no doubt that icing poses a huge risk for UAV operations [9, 21].
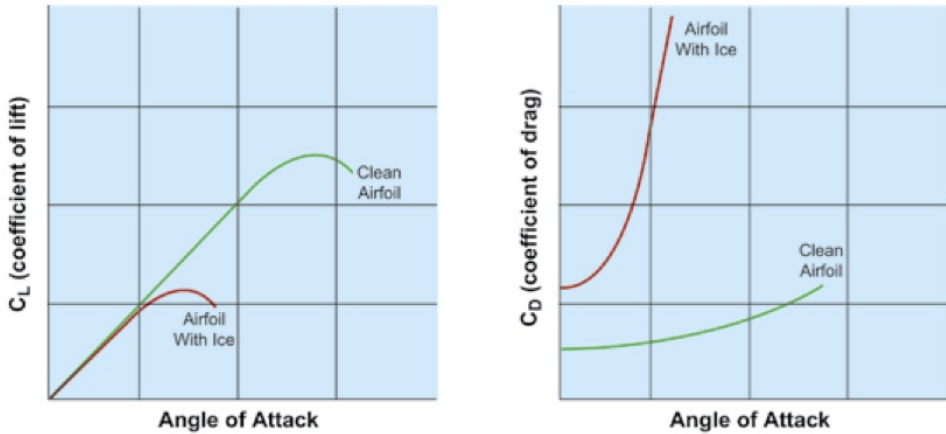
Figure 2.4: Common aerofoil icing effects on lift and drag forces.

Research that can quantify the impact icing can have on UAVs is still ongoing, therefore it is yet undetermined whether the mentioned icing penalties for conventional aircraft will be similar for UAVs, especially small UAVs.

Presently, the risk of icing alters flight plans and causes delays, as one icing mitigating procedure is to avoid icing conditions altogether. The consequences of flying in icing conditions without appropriate countermeasures can be dire as the following section describes.

2.1.5   A Review of Aircraft Icing Incidents

Aircraft icing and its consequences has led to incidents ever since the early beginnings of aviation. Most studies conducted of these are confined to U.S. related incidents alone, as such the review presented here, will only include incidents from this region. The review is based on the work presented in [14, 22–25].

In the period between 1978 to 2002 at least 645 aircraft icing related accidents or incidents occurred, according to Green's findings presented in [24]. Green also found that *the predominant flight phase for the initial encounter with icing conditions is cruise* and that the *principal outcome of these events, in 51% of the cases, is in-flight collision with the ground/water*. Here it should be noted that these statements are tightly linked to type and size of aircraft. Finally Green notes that freezing precipitation was involved in 33% of the events (for which precipitation data was available).

While icing incidents rarely end with fatalities, they do happen. One of the more recent commercial icing incidents that had a fatal outcome occurred at the Clarence Center, New York, on February 12th, 2009. Fifty people lost their lives in the incident involving a Bombardier DHC-8-400. Going back a little further to January 9th, 1997, an Embraer EMB 12RT collided with terrain at Monroe, Michigan. 29 people lost there lives as a thin rough glaze/mixed ice layer formed on the leading edge of the wings. In aircraft icing a pivotal moment is what is known as the Roselawn accident (or ATR accident). On October 31st, 1994, a twin

engine Regional Air Transport ATR-72-212 en route to Chicagos O'Hare airport, lost control and suddenly rotated approximately 70 degrees starboard followed by a rapid descent ending in an impact with the ground. 68 people were killed in the accident. This accident incited resolve to address aircraft icing issues through regulation and research.

2.2   Unmanned Aircraft

An unmanned aircraft, also know as an unmanned aerial vehicle, a drone, as an unmanned aircraft system (UAS), remotely piloted aircraft systems (RPAS), or by several other names, is an aircraft without a human pilot on board. In this monograph unmanned aircraft or UAV will be the preferred designations and will refer to fixed-wing aircraft. Unmanned aircraft may be operated to various degrees of autonomy; remote control by human operator, intermittent, or fully autonomously, through the control of on board computers.

Over the last decade unmanned aircraft have played an increasingly prominent role in military programs and strategies all around the world. Technological advances have enabled the development of both large UAVs (e.g. Global Hawk, Predator, Eitan, and Triton) and smaller, increasingly capable UAVs (e.g. Wasp, Dragon Eye, Puma, and Nighthawk). Military applications for unmanned aircraft include reconnaissance, surveillance, battle damage assessment, and communication relays [26].

Civil and commercial applications are as of yet not as well developed, although potential applications have a very broad scope, including environmental monitoring (e.g. pollution, weather, and scientific applications), forest fire monitoring, traffic monitoring, precision agriculture, disaster relief, ad hoc communications networks, rural search and rescue, inspection, and for Arctic shipping routes, ice flow monitoring and tracking. One of the more recent potential applications is package delivery, as Amazons *Prime Air*, Google X' *Project Wing*, and DHLs *Parcel Copter*. For many of these applications to develop into a mature level, the reliability of unmanned aircraft needs to improve, advances in their capabilities is required, ease of use must be improved, and associated cost needs to be minimised. In addition to these technical and economic challenges, the regulatory issues of integrating unmanned aircraft into national and international air space needs to be overcome.

The scope of this monograph is focused on addressing some of the challenges posed in the previous paragraph by advancing the capabilities for reliable UAV operations conducted in atmospheric conditions conducive to icing.

2.3   Aircraft Icing Protection Systems

Aircraft IPS typically include means of detecting icing and an active de-ice or anti-ice element. Generally de-icing entails a removal of accreted ice, while anti-icing signifies an altogether prevention of icing. For larger conventional commercial aircraft such systems have been a part of design solutions for decades. However, for the relatively young developing industry of unmanned aircraft no commercially available solution exists.

Note that 'conventional' in this monograph represents all fixed-wing manned aircraft.

For the interested reader, the introduction of icing protection systems found in the following, is based on the work presented in [27–36]

2.3.1 Icing Protection Systems - Conventional Aircraft

For conventional aircraft a wide variety of IPS are commercially available. These can be classified into three different categories depending on their common usage. The categories are 1) thermal-based methods, 2) mechanical based methods, and 3) chemical-based methods.

In the thermal-based category the most common systems are hot air and electro-thermal. The hot air systems typically rely on the high temperature bleed-air from the engine compressor gas or hot exhaust gas, which is transferred to relevant icing exposed surfaces by piccolo tubes. Electro-thermal systems include thermal sources, usually electric heating blankets embedded in the wing structure, under the skin-surface on - and around - the leading edges of the wings and stabilisers. Recently developed conductive polymer nano-composites could eventually render the use of heating blankets moot, however, these composites will not change the fundamental concept behind thermal-based icing protection systems.

The category of mechanical-based icing protection systems could be denominated surface deformation systems. This category of systems can be divided into three sub-categories labelled, 1) pneumatic boots, 2) electromagnetic impulse de-icing, and 3) electromagnetic expulsive boots. The systems labelled pneumatic boots are the most commonly applied systems, employing surface deformation, on conventional aircraft. Pneumatic boots are essentially a thick inflatable rubber membrane bonded to surfaces that require icing protection. When ice has accreted on the rubber membrane it is inflated, imposing bending and shear stresses on the ice layer, which in turn breaks the ice into small pieces that are carried downstream by aerodynamic forces. The two remaining sub-category systems are based on the same principle as the pneumatic boots, although they employ electromagnetic impulses to shed icing. Using these impulses rapidly decreases inflation time (compared to the relatively slow inflatable pneumatic boots), resulting in not only breaking the accreted ice, but launching it off the protected surface area into the incoming airflow.

Chemical-based icing protection can be divided into two sub-categories, 1) ground and 2) in-flight. The prior indicate the icing solution, where certain chemicals (typically ethylene glycol) are applied to exposed aircraft surfaces, thereby lowering the freezing temperature of liquid water. The latter sub-category is generally denoted the weeping wing solution, as chemicals are exuded in-flight through nozzles in the leading edge of the wings and stabilisers.

Note that icing detection is not included in conventional aircraft icing protection systems. The reason for this absence is that icing detection is accomplished by the pilots visual confirmation, or through sensors (typically optical) that alert the pilot. Once icing has been established the pilot manually activates any icing protection deemed necessary.

A recurring subject in icing protection solutions is icephobic external surface materials that in essence should repel the ice and minimise ice adhesion. With the advent of nanotechnology, the spectra of potential materials that may fulfil the desired characteristics related to low ice adhesion have expanded considerably. So far, solutions of this type have challenges to overcome before they could be considered a viable alternative to conventional systems. To mention a few; the material has to withstand erosion, stress, and other weathering conditions in terms of its structural integrity. The material needs to preserve its initial characteristics related to icephobicity regardless of erosion and corrosion [37]. Finally, the material should be inexpensive to manufacture, easy to apply, and environmentally friendly.

2.3.2 Icing Protection Systems - Unmanned Aircraft

Icing protection systems (or solutions) for small unmanned aircraft is new field of research, as such no UAV specific literature on this subject presently exists. Icing detection for UAVs, however, is a topic that has been addressed. Therefore, icing detection will be the sole topic of the following section.

Note that icing protection solutions for conventional aircraft are not suitable for smaller UAVs as they are either structurally invasive, expensive, heavy, or hazardous to the environment.

Icing Detection

Structural changes due to icing are common causes for UAV incidents in regions and at altitudes, where temperatures drop below freezing. For fixed wing UAVs various aircraft surfaces are exposed to these changes, causing a significant reduction in aerodynamic ability; i.e. decreasing lift and manoeuvrability, increasing drag and weight, and consequently an increase in power consumption. Timely detection of such changes could potentially prevent icing related UAV incidents.

As technology has advanced, improved methods of ice detection have been developed. Presently various icing detector sensors are commercially available. These, however, are typically highly expensive in a small UAV context.

Another icing detection approach is through algorithms using avionics and indirect sensor measurements. The review of icing detection approaches presented in [38] includes a comparison between existing methods; observer-based algorithms, batch least-squares algorithms, neural networks based algorithms, H_∞ based algorithms, and a combination of neural networks and *Kalman* filtering techniques. The study reveals that among the mentioned approaches, it is the H_∞ and the neural networks combined with Kalman filtering techniques that provide timely and more accurate icing indication. In [39] and [40] icing is diagnosed through an observer-based fault diagnosis technique that detects and estimates the percentage of ice present on the aircraft wing, relying on a linearised lateral model of the aircraft. In [41] the icing detection problem is cast in a multiple-model framework and based on a linearised longitudinal model of the aircraft. A bank of possible system models, whose structure is based on Krener min-max observers, is defined, each one corresponding to a different claimed value of the icing severity factor. Overall state and icing factor estimates are obtained as weighted combinations of the

states of the models and the claimed icing values, respectively. A similar method is presented in [42]. In [43] - which is based on the work presented in [44] - icing detection is addressed using an linear parameter varying (LPV) unknown input observer based approach. A decision algorithm identifies unexpected system dynamics caused by icing through the analysis of temporal and low-frequency residuals. The proposed approach is validated through a case study. Further, this work has been extended in [45], where an LPV proportional integral unknown input observer is used to diagnose actuator faults and icing for UAVs. This approach is more robust towards noise and also includes a wind to noise ratio allowing for optimal tuning of relevant design parameters. The approach is validated through simulations. The work described in [46] applies an approach similar to the one presented in [43], but for over-actuated UAVs. In [47] in-flight parameter estimation of dynamic aircraft parameters is completed, using a *Hinf* parameter identification algorithm. Subsequently, icing detection and location is provided by the application of a probabilistic neural network (supplied with a database corresponding to various icing locations and severities for training purposes), receiving the parameter estimates as inputs. A simulation study of the approach reveals promising results. The work presented in [48] has a different approach altogether. Here aligned Carbon nanotubes (CNTs) are applied as a separate surface layer. This layer is then heated through electrical heating. A change in heat capacity will then signify an additional material, such as water or ice. This approach assume that certain parameters have a constant behaviour and that the additional material has significant mass.

As presented in the preceding paragraph one approach to icing detection is to cast the problem in a fault diagnosis framework. This will be the approach for two novel solutions presented in this monograph. Such an approach is feasible as icing on exposed aircraft surfaces induces certain penalties to the nominal behaviour of the aircraft system. Fault diagnosis has been applied extensively to detect various aircraft faults. The fault diagnosis approach presented in [49] is based on a two-stage adaptive Kalman filter for simultaneous state and fault parameter estimation and a statistical change detection solution, to detect and isolate aircraft control actuator faults. In [50], fault diagnosis serves as the base for a study on a reconfigurable control allocation solution, for an over-actuated aircraft system experiencing control actuator faults. Numerous investigations into similar faults conducted for UAVs have been completed. In [51], control surface faults are diagnosed, applying a signals processing approach. The work presented in [52] uses a statistical change detection approach to detect faults in air system sensors (pitot-tube) and on control surfaces. Interestingly, the latter approach has also been used to detect faults, caused by ice clogging the pitot-tube, as presented in [53].

2.3.3 Icing Protection Solution Objectives

The objectives of the developed icing protection solution presented here are as follows:

- Enable safe and robust aircraft operations in spite of harsh weather conditions, conducive to icing.

- Have little negative impact on aircraft aerodynamics, weight, and overall performance.

- In-flight icing detection, mitigation, or altogether prevention should be executed completely autonomously, while optimising energy consumption.

- IPS integration procedures should accommodate UAV platforms generically, while abiding by flight readiness and airworthiness requirements.

How the solution achieves these objectives are described throughout this monograph.

2.4   Unmanned Aircraft Test beds

This section provides a brief introduction to four UAV platforms displayed in Figures 2.5–2.8. The platforms serve as the primary test beds for the development of an IPS, introduced in [54], for small UAVs. The cruise airspeed for the four aircraft is 15 m/s to 20 m/s, all of which are powered by an electrical motor.

- The X8 Skywalker, developed by Skywalker Technology Co, Ltd. and integrated by the Norwegian University of Science and Technology (NTNU). The X8 Skywalker UAV platform has an operational of approximately 40 km at a cruise airspeed of 18 m/s, depending on flight conditions. Maximum payload weight is 1 kg and maximum take-off weight is 4.5 kg. The aircraft has a wingspan 2120 mm.

- The Dragon Eye, developed by the Naval Research Laboratory (NRL). The Dragon Eye UAV platform operates at a cruise airspeed of approximately 18 m/s, with an endurance of 60 minutes and a range of 5 km. The maximum take-off weight is 2.7 kg and maximum payload weight is approximately 1 kg. The wingspan of the Dragon Eye is 1143 mm.

- The Puma, developed by AeroVironment. This platform performs at airspeeds ranging from 10 m/s to 23 m/s, with an endurance of approximately 3 hours and maximum range of 15 km. The maximum take-off weight is approximately 6.3 kg. The wingspan of the PUMA UAV platform is 2800 mm.

- The Aeromapper, developed by Aeromao and operated by the The University of Alaska, Fairbanks (UAF). The approximate maximum airspeed for the Aeromapper is 25 m/s and cruise airspeed is approximately 15 m/s, with an endurance of 90-100 minutes, and a ground telemetry range of approximately 20 km. The payload bay module used for the work presented here allows for approximately 0.65 kg of payload with a maximum take-off weight for the combined aircraft of 5.35 kg. The wingspan of the Aeromapper is 2000 mm.

The composition of the X8 Skywalker UAV platform consists of expanded polyolefine (EPO) alone, making it a highly durable and light weight platform. The structural composition of the Dragon Eye and Puma are identical. The core of these platforms consists of expanded polystyrene (EPS) foam covered by a thin Kevlar surface coating. Finally, the composition of the Aeromapper platform is made up of a thin skin layer of carbon fibre, covering a core of balsa and air.

Figure 2.5: The X8 Skywalker UAV platform.
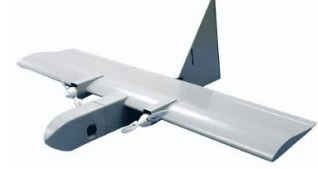
Figure 2.6: The Dragon Eye UAV platform.

Figure 2.7: The Puma UAV platform.

Figure 2.8: The Aeromapper UAV platform.

2.4.1 Aerofoils

Subsequent analyses require aerofoil details for all four platforms. Unfortunately, such information is not publicly available. Consequently, aerofoils that display similar characteristics, with public accessible details, have been identified. The X8 Skywalker aerofoil has been reconstructed manually.

- X8 Skywalker aerofoil - reconstructed.

- Dragon Eye aerofoil - Liebeck LA2573A aerofoil.

- Puma aerofoil - Selig/Donovan SD7032 aerofoil.

- Aeromapper aerofoil - Selig/Donovan SD8020 aerofoil.

The aerofoil profiles are illustrated in Figures 2.9–2.12
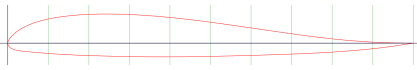
Figure 2.9: X8 Skywalker reconstructed aerofoil.
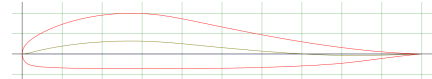
Figure 2.10: Dragon Eye equivalent aerofoil - LA2573A.
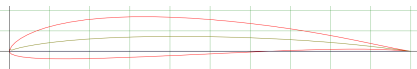
Figure 2.11: Puma equivalent aerofoil - SD7032.
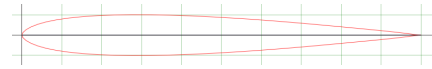
Figure 2.12: Aeromapper aerofoil - SD8020.

17

2.5 Heat Transfer

The IPS presented in this monograph is based on electro-thermal sources. Thermo-dynamic phenomena - like the fundamental heat transfer processes - are essential in understanding the concepts and inner workings of the proposed solution.

Heat transfer, i.e. the flow of energy in the form of heat, occurs through the three fundamental processes, thermal conduction, thermal convection, and thermal radiation. Heat transfer is a process that describes changes in the internal energy of thermodynamic systems. The following introduction to thermodynamics fundamental processes is based on [55–62].

2.5.1 Thermal Conduction

Thermal conduction is the transfer of internal energy by microscopic diffusion and collision of particles or quasi-particles, thereby transferring kinetic and potential energy (collectively denoted internal energy). Thermal conduction occurs within a single object or material, or between multiple objects in contact with each other.

Joseph Fourier was the first to formulate a complete exposition on the theory of heat conduction, where he stated the empirical law, now known as Fourier's law: *the heat flux, $\dot{Q} = \dot{q}/A$ [W/m^2], resulting from thermal conduction is proportional to the magnitude of the temperature gradient and opposite to it in sign* [56]. Utilising k [W/(m·K)] as the constant of proportionality, denoted the thermal conductivity, Fourier's law can be written as

$$\vec{Q} = -k \cdot \nabla T, \tag{2.1}$$

where T is the temperature in Kelvin. Note that the heat flux $\dot{Q}$ is the rate of heat energy transfer $\dot{q}$ through a given surface area A, per unit time. In general the coefficient of proportionality k - the thermal conductivity - also depends on position and temperature, i.e. $k = k(\vec{r}, T(\vec{r}, t))$, where $\vec{r}$ is the position vector. In this monograph, however, relevant materials are considered homogeneous, as such $k = k(T)$. The temperature gradient ∇T describes both magnitude and direction of the maximum temperature change at each point and is defined as

$$\nabla T \equiv \vec{i}\frac{\partial T}{\partial x} + \vec{j}\frac{\partial T}{\partial y} + \vec{k}\frac{\partial T}{\partial z}. \tag{2.2}$$

Utilising Fourier's law, the first law of thermodynamics (the law of energy conservation), and Gauss' theorem the following expression is obtained[1],

$$\nabla \cdot k\nabla T + \dot{Q} = \rho c_p \frac{\partial T}{\partial t}, \tag{2.3}$$

Where ρ is the density of a given medium (gas, fluid, or solid) and c_p is the specific heat capacity of the same medium. (2.3) is known as the *heat diffusion equation* in three dimensional space, which is valid under the constraint of two assumptions:

- Incompressible medium

---

[1]The interested reader is referred to [56] for the complete derivation.

- No convection (The medium cannot undergo any relative motion)

If the variation of k with T is small, (2.3) can be rewritten into

$$\nabla^2 T + \frac{\dot{Q}}{k} = \frac{1}{\alpha_d} \frac{\partial T}{\partial t}, \tag{2.4}$$

where α_d [m^2/s] is the thermal diffusivity, which is given by

$$\alpha_d = \frac{k}{\rho c_p}. \tag{2.5}$$

The thermal diffusivity is a measure of the rate at which a medium distributes heat away from a thermal source. As materials in general are not heated instantaneously α includes both the thermal conductivity k and the volumetric heat capacity ρc_p.

From (2.4), the expression $\nabla^2 T = \nabla \cdot \nabla T$ is known as the Laplacian and in a Cartesian coordinate system is given by

$$\nabla^2 T = \frac{\partial^2 T}{\partial x^2} + \frac{\partial^2 T}{\partial y^2} + \frac{\partial^2 T}{\partial z^2} \tag{2.6}$$

(2.4) is recognised as a complete multidimensional transient heat conduction equation [56].

2.5.2 Thermal Convection

Thermal convection occurs as energy transfer due to diffusion and by bulk (or macroscopic) motion of a fluid. This motion is attributed to large number of molecules moving collectively or as aggregates. In the presence of a temperature gradient such motion contributes to the transfer of thermal energy. As molecules in aggregate maintain their random motion, the combined thermal transfer is due to the superposition of energy transferral by random motion of the molecules and the bulk motion of the fluid [57].

An alternative description of the physical process of thermal convection from [56, 58] follows. Consider a cold fluid flowing past a warm body. The fluid immediately adjacent to the body forms a layer of thickness δ, which flows at a reduced velocity. This layer is know as the *boundary layer*. Heat is conducted into the boundary layer, which transports it farther downstream, where it is mixed with the cooler free stream flowing fluid. This process, where heat is transported by a moving fluid is called convection. The mathematical representation of convection attributed to Sir Isaac Newton is given by

$$\dot{Q} = \bar{h} \Delta T, \tag{2.7}$$

where $\Delta T \equiv (T_s - T_\infty)$. (2.7) is the steady-state form of what is known as Newton's law of cooling [59, 60], where T_s is the solid' surface temperature and T_∞ is the temperature of the oncoming flow. The coefficient $\bar{h}$ [W/(m·K)] is termed the *convective heat transfer coefficient*, where the bar signifies that it is the average of coefficients over the surface of a body. Without the bar, h is simply a local value at a specific point on the body surface. The convective heat transfer coefficient is

a highly intricate quantity to predict and it is tightly linked to the motion of the fluid flowing around the body that is heated or cooled.

The boundary layer can be in either a turbulent or laminar flow regime, where the latter is characterised by the fluid flowing in parallel layers, i.e. there is no transferral of fluid particles between the parallel layers, nor any swirls or eddies [63]. Properties concerning the laminar flow regime is a high momentum of diffusion and a lower momentum of convection [56, 58, 64]. The work presented in this monograph is based on the assumption that the flow around relevant areas of a given aerofoil is laminar.

It is evident that thermal convection is highly interconnected with fluid dynamics, therefore significant parameters necessitate an introduction. One such parameter is a dimensionless quantity that aides the characterisation and quantification of different flow regimes and is known as the Reynolds number, Re, which is defined as the ratio of momentum forces to viscous forces. Laminar flow generally occurs at low Reynolds numbers (Re) (though still at Re$> 10^4$ for aerofoils [65]), where viscous forces are more dominant, or where the flow velocity is less dominant. For flow around aerofoils Re is defined as

$$\mathrm{Re} = \frac{V_\infty x_c}{\nu},\tag{2.8}$$

where V_∞ is the free stream flow velocity, x_c is a characteristic linear dimension (for aerofoils this corresponds to the chord line), and ν is the kinematic viscosity of the fluid in which the aerofoil operates.

When a temperature difference exists between a solid and the free stream of a fluid flowing past, a thermal boundary layer is present, with thickness δ_t, different from the thickness of the boundary layer δ. Heat transfer at the surface is by conduction and, as such

$$-k_f \left. \frac{\partial (T - T_s)}{\partial y} \right|_{y=0} = h (T_s - T_\infty),\tag{2.9}$$

where k_f is the conductivity of the fluid, T is the temperature at a given point in the the thermal boundary layer, and y is a perpendicular distance from the surface of the solid. The term on the left of the equality corresponds to Fourier's law (of thermal conduction) in one-dimensional space. Rearranging (2.9) and multiplying by the inverse of a characteristic linear dimension results in

$$\frac{hx_c}{k} = \frac{\left. \frac{\partial (T_s - T)}{\partial y} \right|_{y=0}}{\frac{(T_s - T_\infty)}{x_c}} \equiv \mathrm{Nu}_{x_c},\tag{2.10}$$

which is known as the *Nusselt number* (Nu) and can be summarised as the ratio of conductive thermal resistance to the convective thermal resistance of the fluid [58]. The temperature profile for a fluid flowing past a heated solid surface is illustrated in Figure 2.13.

A Nusselt number close to 1 signifies laminar flow, where larger values for Nu correspond to a turbulent flow.
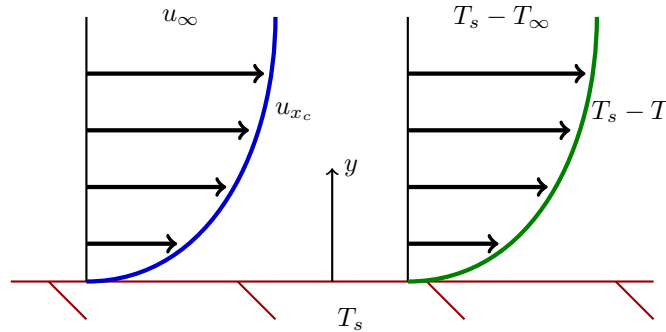
Figure 2.13: Temperature and velocity profiles for a fluid flowing past a heated plate.

The final significant parameter introduced here is the *Prandtl number* (Pr), which can be summarised as the ratio of molecular kinematic viscosity to the molecular thermal diffusivity [58], and is defined as

$$\text{Pr} \equiv \frac{\nu}{\alpha}. \tag{2.11}$$

The values of the Prandtl number indicate the interrelation between the thickness of the boundary layer and the thickness of the thermal boundary layer. If $\text{Pr} = 1$ it indicates $\delta = \delta_t$, further when $\text{Pr} > 1 \Rightarrow \delta > \delta_t$, and conversely when $\text{Pr} < 1 \Rightarrow \delta < \delta_t$. Intuitively this is sensible as high viscosity leads to a thick boundary layer, and a high thermal diffusivity should imply a thick thermal boundary layer.

Thermal convection is generally divided into two main classifications. These are related to the driving force causing the flow. For the work presented in this paper focus will be limited to *forced convection*, as opposed to *free* or *natural convection*. Forced convection is the classification applied for describing convection, where fluid circulation is produced by an external agent, such as wind, a fan, or the forced movement of a body through a fluid.

2.5.3 Thermal Radiation

Thermal radiation is electromagnetic radiation generated by particle collision that cause the kinetic energy of atoms and molecules to change. It is this change that results in a charge-acceleration and/or dipole oscillation, which in turn produce the electromagnetic radiation [61].

Thermal radiation differs from conduction and convection in several ways, but most prominently in that no medium is required for its propagation. In fact maximum thermal radiation is achieved when the transferral of energy is in perfect vacuum. The perfect thermal radiator is termed a *black body* and has the properties that it absorbs all incident energy that reaches it and reflects nothing [58]. Black bodies do, however, emit energy as electromagnetic waves at wavelengths $0.1 - 100\mu m$. The energy emission, i.e. the radiative equivalent of thermal flux for

conduction and convection, (E [W/m^2]), from a black body is given by

$$E_b(T) = \sigma T^4, \tag{2.12}$$

where T is the absolute temperature and the proportionality constant σ is the Stefan Boltzmann constant, which equals 5.676×10^{-8} [W/(m$^2 \cdot K$)]. Equation (2.12) is most often referred to as the *Stefan Boltzmann law* of thermal radiation. For bodies that do not display the same energy characteristics as a black body, the expression found in (2.12) will not suffice, another parameter is required. The total energy emission, $E(T)$, of a given body surface is defined as the total rate of thermal energy emitted by radiation from that surface in all directions and at all wavelengths per unit surface area [58]. Closely related to the total energy emission is the emissivity ϵ, which is defined as

$$\epsilon \equiv \frac{E(T)}{E_b(T)}, \quad 0 < \epsilon \leq 1, \tag{2.13}$$

consequently the total energy emitted per unit surface area can be written as

$$E(T) = \epsilon E_b(T) = A\epsilon\sigma T^4, \tag{2.14}$$

where A is the radiating surface area.

It is evident that $\epsilon = 1$ for a black body.

It should be noted that (2.14) is an approximation based on the assumption here denoted the *grey body assumption*. In a radiative context no real grey body exist, however, many exhibit grey behaviour, e.g. the sun approximately appears to the earth as a grey body with $\epsilon = 0.6$ [56]. The emittance of most common materials and coatings varies with wavelength in the thermal range. The total emittance accounts for this behaviour at a particular temperature. By applying this, the emmissive power can be written as if the body was grey without integrating over wavelength, as is seen in the expression of (2.14).

For the remainder of the work presented in this monograph, radiation has been discarded in any contributory thermal manner, as it will be relatively insignificant. The exclusion of radiation is reasonable, as $A << 1$ m^2, $\epsilon \leq 1$, the infinitesimal numerical value of σ, and $T \in [-20, 20] \Rightarrow T^4 \leq 160,000$, hence $E(T) << 1$.

Discarding the contribution from radiation is also corroborated by the work presented in [66, 67], although it should be mentioned that the work presented in [66, 67] was conducted on larger aircraft operating at flight envelopes that differ from small unmanned aircraft.

2.6   Icing Aero-Thermodynamics

The following is an introduction to fundamental thermodynamic theory when applied to the field of aerofoils in icing conditions. The introduction here is based on the work of [25, 68–71] and the seminal work found in [62, 66, 67, 72, 73].

Consider the first law of thermodynamics - the law of energy conservation - as a collection of thermal energy components. These components were identified and collected into a single model, denoted the *Messinger model* [67] in 1953. Each

component contributes to the thermal equilibrium of the thermodynamic system, here comprised of the aircraft wing structure, the electro-thermal source, and the surrounding environment.

One of the primary contributors is the dissipation of energy through thermal convection (as presented in Section 2.5.2 - henceforth denoted $\dot{Q}_C$), which can be expressed as

$$\dot{Q}_C = \bar{h}\left(T_s - T_\infty\right), \tag{2.15}$$

where T_s is the surface temperature of any exposed aircraft surface and T_∞ is the temperature of the free airflow surrounding the aircraft body. In the work presented in this monograph the surface temperature will be equivalent to the temperature of the electro-thermal source, i.e. $T_s = T_{ETS}$. The legitimacy for this latter distinction is that the electro-thermal source is applied directly onto the exposed aircraft surfaces.

Thermal dissipation by incoming liquid water droplets $\dot{Q}_d$ is given by

$$\dot{Q}_d = \rho_\infty \beta_c V_\infty c_{p,w}\left(T_{ETS} - T_\infty\right), \tag{2.16}$$

where ρ_∞ and V_∞ are the free airflow density and velocity, respectively. $c_{p,w}$ [J/(kg·K)] is the specific heat coefficient of water. β_c is denoted the local collection efficiency.

A quick aside about the local collection efficiency parameter. This parameter can be regarded as a means to estimate the amount of water that impinges exposed aircraft surfaces, i.e. the surface areas subject to ice formation. The local collection efficiency is defined as

$$\beta_c \equiv \frac{\Delta y_0}{\Delta s}, \tag{2.17}$$
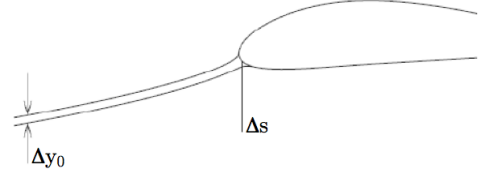
Figure 2.14: Definition of collection efficiency [2].

where Δy_0 is the distance between two liquid water droplets at the release plane and Δs is the distance between the two locations of impact of the same droplets on the aerofoil (see Figure 2.14).

Another thermal dissipation component is of an evaporative kind, which can be expressed by

$$\dot{Q}_e = \mathcal{X}_e\left[e(T_{ETS}) - e(T_\infty)\right], \tag{2.18}$$

where $\mathcal{X}_e$ is denoted the evaporation coefficient. In [74] the evaporation function $e(T)$ is approximated by a sixth-order polynomial for $T_\infty \in [233, 320]$K. However, according to [69] this approximation can be simplified for the subset of temperatures $T_\infty \in [257, 273.15]$K to a linear approximation, given by

$$e(T) \approx -6.803 \times 10^3 + e_0 T, \tag{2.19}$$

where e_0 is known as the saturation vapour pressure constant.

Sublimation is the chemical process where a solid changes phase to a gaseous state without an intermediate liquid stage, e.g. when ice experiences a phase change

to water vapour without changing phase to the intermediate liquid water stage. Thermal dissipation by sublimation can be expressed as

$$Q_s = \mathcal{X}_s e_0 \left(T_{ETS} - T_\infty \right),$$ (2.20)

where $\mathcal{X}_s$ is denoted the sublimation coefficient, which is related to the evaporation coefficient as

$$\mathcal{X}_s = \mathcal{X}_e \frac{L_s}{L_e};$$ (2.21)

L_s [J/kg] and L_e [J/kg] are latent heat constants for sublimation and evaporation, respectively.

Where the preceding components have all been negative, or dissipative terms, the following are the positive components to the equilibrium of the thermodynamic system. The first of these positive contributors is the thermal energy gained by aerodynamic (viscous or frictional) heating, which occurs as the kinetic energy of the aircraft, as it passes through air, is converted into heat by skin friction on the surface of the aircraft at a rate that depends on the viscosity and speed of the air (i.e. the speed of the aircraft). This aerodynamic heating is given by

$$Q_a = \frac{r_a \bar{h} V_\infty}{2 c_p},$$ (2.22)

where r_a is the adiabatic recovery factor (for a laminar airflow $r_a = \mathrm{Pr}^{1/2}$ and for turbulent flow $r_a = \mathrm{Pr}^{1/3}$ [70]).

Thermal energy gained equivalent to the kinetic energy of the liquid water particles as they impinge the exposed aircraft surface. This kinetic energy contribution can be expressed as

$$Q_k = \beta_c V_\infty G \frac{V_\infty^2}{2},$$ (2.23)

with G [kg/m^3] denoting the liquid water content (also abbreviated LWC) in the free airflow.

The final positive thermal energy component in the presentation here is the latent heat of solidification, which is the shift in enthalpy as energy is provided to change the state of a substance from solid to liquid. The expression for latent heat of solidification is given by

$$Q_l = \rho_i L_F \frac{\partial B}{\partial t},$$ (2.24)

where ρ_i is the density of ice. Note that this quantity can assume different values depending on the type of ice that is forming. L_f [J/kg] is the latent heat of fusion constant and B [m] is the ice layer thickness.

The expression for energy conservation can now be formulated as

$$Q_C + Q_d + Q_e + Q_s = Q_a + Q_k + Q_l.$$ (2.25)

Note here that based on the work presented in [66, 67] radiation is not included as a contributory component to the energy balance equation featured in (2.25).

In [71] the *Messinger Model* was extended to account for compressible flow and in [69] conduction through ice and water layers was included in the model.

It should be noted that the model applied here will be the standard *Messinger Model* with an added dissipative term. This final dissipative contribution comes from conduction and occurs as heat is transferred from the electro-thermal source into the aircraft wing structure. A one-dimensional approximation of *Fourier's Law* is given by

$$Q_c = -k \left(T_{ETS} - T_\infty \right).$$ (2.26)

This approximation has been deemed sufficient and appropriate as the specific testbed platforms (presented previously) are comprised of thermally insulating materials. As such the overall contribution from thermal conduction of this type will be small, consequently any multidimensional contribution is assumed to be negligible.

2.7 Contributions and Monograph Structure

The core structure and **contributions** of the monograph are presented in Chapters 3–10 - as described in the following subsections - and is concluded by Chapter 11.

2.7.1 Chapter 3

The first core chapter of this monograph provides a description of the modular architecture of the proposed IPS. This also serves as **contribution 1** of the monograph.

The system and its architecture is the first of its kind for UAVs and it distinguishes itself - comparing it to solutions for conventional aircraft - as icing is mitigated or altogether prevented autonomously. The proposed architecture enables the IPS to execute on-line and in-flight icing detection, mitigation, or prevention, ensuring safe and robust UAV operations regardless of potential atmospheric icing conditions.

The architecture proposed here has not been published, but is a main contributor to the patent (application is under development).

2.7.2 Chapter 4

In this monograph two different icing detection algorithms are presented. The first of these is the *model-based icing detection algorithm*, which is **contribution 2** in this monograph.

This algorithm addresses the issue of detecting icing when it forms on the leading edge of small UAV wings by means of a surface change detection and identification approach using a nonlinear longitudinal model of the aircraft. Under the assumption that model uncertainties, such as unknown aerodynamic coefficients, are a priori estimated, the scheme is based on a structural analysis performed on the system, with residual generation as an outcome. A generalised likelihood ratio test (GLRT) is then used to detect any changes in the generated residuals, where any constant change would constitute an occurrence of a fault, i.e. icing forming on the leading edge of the aircraft wings.

The proposed algorithm has been presented in [75] and was published in the fall of 2015.

2.7.3   Chapter 5

The second icing detection algorithm presented in this monograph is the *electro-thermal-based icing detection algorithm*, which constitutes **contribution 3**.

As for its collaborative partner (the model-based icing detection algorithm) the electro-thermal-based icing detection algorithm applies developed residuals to detect occurrences of icing. The proposed algorithm is based on the thermodynamic system surrounding an electro-thermal source (applied to the leading edge of the aircraft wings), the aircraft wings, and ambient conditions. To detect icing the electro-thermal source - already applied to exposed aircraft surfaces - is actively used to induce temperature responses that will deviate once icing is present.

The algorithm proposed here has not been published, but is on of the main contributions in the patent submitted as [76].

2.7.4   Chapter 6

The control unit presented in this chapter serves as **contribution 4** in this monograph.

The control unit is comprised of the hardware and software of the proposed IPS, i.e. it is the heart and mind of the entire solution. The hardware consists of microcomputers, active components, sensors, and prototype printed circuit boards (PCB). The software developed for the control unit include the two icing detection algorithms, various data collection and processing algorithms, and control algorithms.

The control unit is based on the work found in [54] and is on of the contributions in the patent submitted as [76].

2.7.5   Chapter 7

This chapter is a presentation of 2-dimensional thermodynamic analyses of the IPS integrated onto the the four testbed UAV platform aerofoils. The work presented here constitutes **contribution 5**.

The thermodynamic system analysed is comprised of an aircraft wing, an electro-thermal source, and the surrounding airflow. It is based on numerical simulations applying a transient finite element approach to account for multidimensional boundary conditions that vary along the chord of any aerofoil.

When aircraft operations occur in non-icing conditions the thermodynamic system is in thermal equilibrium. However, when ambient conditions change and the aircraft - operating in non-icing conditions - suddenly operates in potential icing conditions the IPS will drive the thermodynamic system out of equilibrium by increasing the temperature of the electro-thermal source, hence thermal energy begins to flow. The analyses presented are conducted to investigate the thermal distribution once the electro-thermal source is activated in a virtual flight environment. The chapter will also provide an investigation into the power consumption of the present electro-thermal source layout and compare it to an alternative layout.

The thermodynamic analyses are an extension to the published work found in [77].

2.7.6   Chapter 8

Appropriate integration procedures are a necessity to accommodate specific UAV platforms, while abiding by flight readiness and airworthiness requirements. Chapter 8 provides a presentation of this very topic, which also serve as **contribution 6** of this monograph.

The process of integrating (or retro-fitting) the IPS is specific to each platform UAV. This chapter begins with a presentation of the integration procedures that have been required to accommodate the structural design of each specific platform, while ensuring that the IPS performs as needed. This is followed by an introduction to various test sites used for preliminary test flights and a presentation of some of the obtained results.

The procedures and results obtained and presented in this chapter are previously unpublished.

2.7.7   Chapter 9

This chapter presents findings from wind icing tunnel experiments of the developed IPS, integrated onto several test bed UAV platforms. The work presented is listed as **contribution 7**.

The test site facilitating the wind icing tunnel is the LeClerc Icing Research Laboratory (LIRL), developed and operated by Cox & Company inc., located at 1664 Old Country Road, Plainview, NY 11803. All experiments were obtained during a two day period in mid February 2016. The chapter includes an introduction to the test facility, a presentation of the preceding work required, and reveal results that a discussed and concluded upon.

The work presented in this chapter is previously unpublished.

2.7.8   Chapter 10

The final core chapter of the doctoral thesis revolves around test flights of the proposed IPS integrated onto the X8 Skywalker and Dragon Eye UAV platforms. The work presented here constitutes **contribution 8**, the final contribution of this monograph.

The final step in demonstrating the feasibility of the proposed IPS is to conduct flight tests. The main contribution of Chapter 10 is the presentation of findings obtained from flight tests conducted in Ny-Ålesund, Svalbard, Norway. However, the chapter also includes a brief introduction to some preliminary test flights conducted in Anchorage, Alaska, in Ny-Ålesund, Svalbard, Norway, and at Udduvoll, Norway. It should be noted that some of these preliminary test flights were the first flights in the world for any IPS integrated onto any small unmanned aircraft. Finally all test locations are introduced, and results are presented, discussed, and concluded upon.

The results from this chapter have not previously been published.

2.7.9 Publications

The work revolving this doctorate has resulted in the following publications and a patent.

[54] Sørensen KL, Helland AS, Johansen TA. Carbon nanomaterial-based wing temperature control system for in-flight anti-icing and de-icing of unmanned aerial vehicles. In: IEEE Aerospace Conference; 2015.

[75] Sørensen KL, Blanke M, Johansen TA. Diagnosis of Wing Icing Through Lift and Drag Coefficient Change Detection for Small Unmanned Aircraft. In: IFAC Workshop Series; 2015. p. 541–546

[76] Sørensen KL, Johansen TA, Borup KT, inventors; Icing Control System. ; 2016. GB Patent 1614339.8 (*Submitted*)

[77] Sørensen KL, Johansen TA. Thermodynamics of a Carbon Nano-Materials Based Icing Protection System for Unmanned Aerial Vehicle. In: IEEE Aerospace Conference; 2016.

[78] Johansen TA, Cristofaro A, Sørensen KL, Hansen JM, Fossen TI. On estimation of wind velocity, angle-of-attack and sideslip angle of small uavs using standard sensors. In: International Conference on Unmanned Aircraft Systems (ICUAS); 2015. p. 510–519

[79] Sørensen KL, Johansen TA. Electro-Thermal Icing Detection for Small Unmanned Aircraft. IEEE Transactions on Aerospace and Electronic Systems. 2016; (*Submitted*)

[80] Sørensen KL, Johansen TA. Thermodynamic Analyses of Electro-Thermal Anti-Icing System for Small Unmanned Aircraft. AIAA Journal of Aircraft. 2016; (*Submitted*)

Chapter 3

Icing Protection Solution Architecture and Overview

This chapter provides an introduction to the modular architecture of the icing protection solution. To start the chapter, an overview of the architecture is presented and described. This initial part of the chapter will also include a brief description of the three primary elements comprising the IPS. Subsequently the *control unit* and sub-components are introduced and briefly described. The chapter is concluded with a summary of the most important presented aspects.

3.1 Component Overview

The IPS presented here is based on three primary elements, 1) an electro-thermal source, 2) an intelligent control unit, and 3) a power source, which could supply power from the aircraft engine, or as is the design presently, from batteries (i.e. system is standalone, chosen based on ease of testing). The control unit is primed by an on-board atmospheric sensor package, measuring ambient environmental conditions. Once the risk of icing is established, two ice detection algorithms - working in parallel - are activated. This approach ensures robustness and accuracy. If icing is detected, control algorithms controls the power supplied to the electro-thermal source, thereby achieving temperature control of the thermal source, while minimizing power consumption. The overall functionality of the proposed IPS, running in a de-icing mode, is illustrated by the high level state diagram found in Figure 3.1. The corresponding diagram for an anti-icing mode of operation, for the present IPS, would include only a state where potential icing would be determined by the atmospheric sensor and an icing preventing state.

The solution is comprised of several components as seen in Figure 3.2. The "external" components to the control unit will be described in a summary manner in the following, whereas the "internal" components to the control unit will be presented further sub-sequentially.

Note that the parallel icing detection approach is merely a preliminary default configuration. The system will work fine with just one. The notion of two, or more,
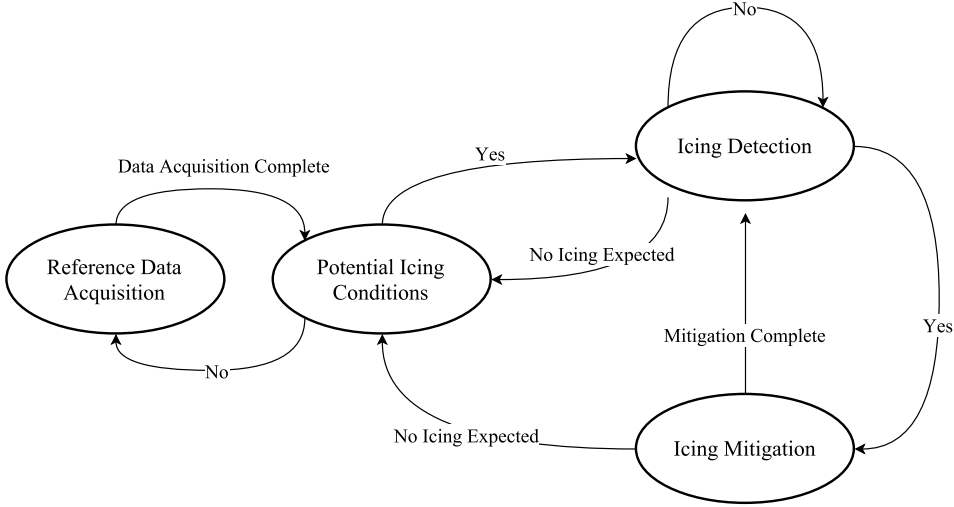
Figure 3.1: Icing Protection Solution (de-icing mode) - High level state diagram.

detection algorithms is merely to strengthen reliability and robustness, which in turn will result in a higher safety level and an improved performance.

Regarding Figure 3.2 and the overall architecture of the solution, it should be noted that there is *one* atmospheric sensor package; *one* set of air data measurements; *one* set of pressure sensor measurements; *one* power source; and *one* air data estimation, for the aircraft in its entirety, but that all the other components (internal and external to the control unit) have duplicates (signified by a capital T - for twin - at the bottom right of each relevant component in Figure 3.2), as each wing has its own electro-thermal source and therefore require individual feedback and algorithms for optimal control.

As seen in Figure 3.2 several sensor measurement blocks provide measurements to the control unit. A brief explanation follows and a clarifying diagram of the IPS, integrated onto an X8 Skywalker UAV platform, is found in Figure 3.3.

- The *external sensor measurements* includes; an IMU[1] supplying measurements of the specific force and angular rate of the aircraft; a pitot-static tube providing measurements of the relative velocity in the longitudinal axis of the aircraft; an engine speed sensor; GNSS-based[2] ground velocity measurements; and control surface input measurements

- The *air data measurements* signify a number of strategically located sensors providing pressure measurements and secondary temperature measurements

- The *atmospheric sensor measurements* provides both ambient temperature- and relative humidity measurements

---

[1]An inertial measurement unit (IMU) is an electronic device that measures and reports a body's specific force, angular rate, and magnetic field surrounding that body. These measurements are obtained using a combination of accelerometers, gyroscopes, and magnetometers.

[2]GNSS is an acronym for the Global Navigation Satellite System, which is a satellite system that is used to pinpoint the geographic location of a user's receiver anywhere in the world
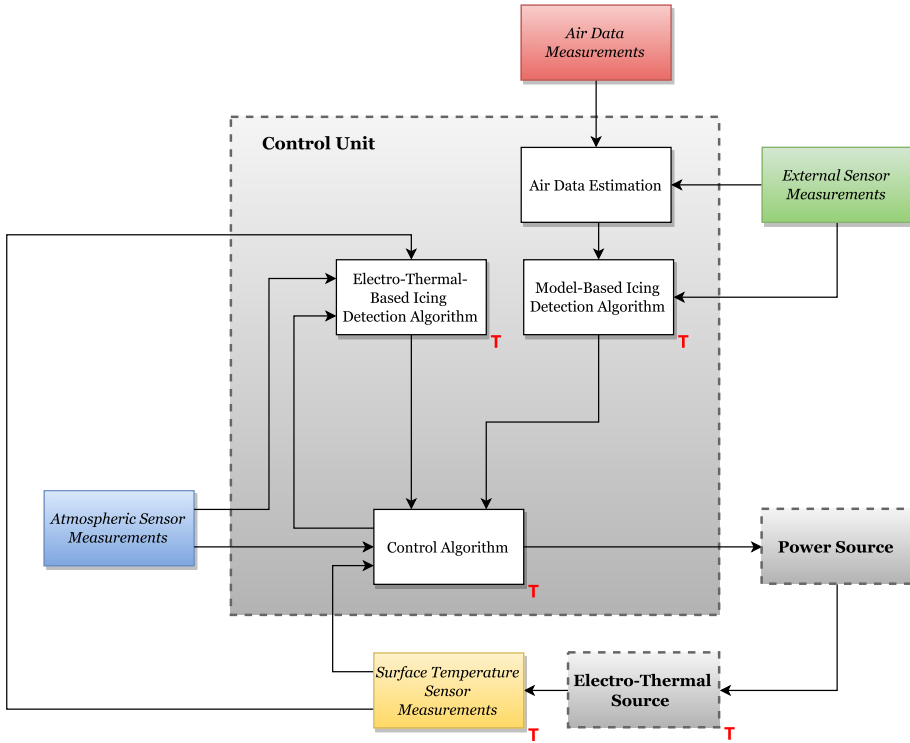
Figure 3.2: Icing Protection Solution - component overview.

- The *surface temperature sensor measurements* is comprised of a sensor array embedded in each wing. These sensor arrays supply the control unit with temperature measurements of the electro-thermal sources (one is applied to each wing)

Potential icing conditions are considered present when the atmospheric sensor measurements indicate a relative humidity RH $\leq 50\%$ and ambient temperatures $T_\infty \leq 0°$C, parameter values that according to [81–84] ensures non-icing conditions despite sub-zero ambient temperatures.

Two of the three primary elements of the solution presented in this document are the electro-thermal source and the power source, both found in Figure 3.2.

- The composition of the electro thermal source is based on Carbon Nano materials and is applied through a liquid carrier (a coating). The internal resistivity of the electro-thermal source is based on the thickness of any applied layer and area-size of said layer.

- The power source can be either a battery pack, typically lithium polymer batteries, or power can be supplied by the aircraft engine through a generator.
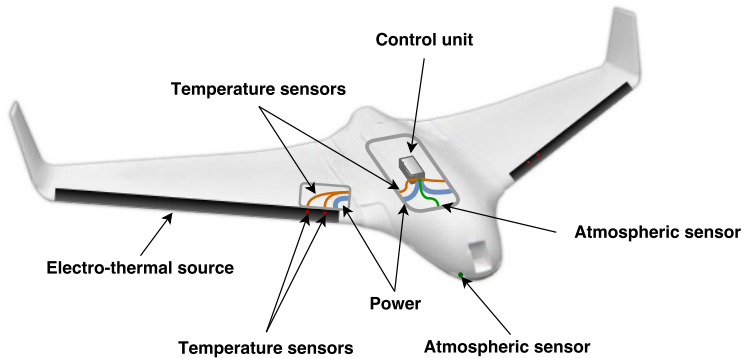
Figure 3.3: Integrated IPS onto X8 Skywalker UAV platform.

Power is supplied to the electro-thermal source through a copper bus-bar located on the wings of the aircraft, as seen in Figure 3.4. Here it should be noted that the thickness, location, and layout of the electro-thermal source is directly linked to power consumption. Optimizing these three aspects is key to achieving the highest level of performance.
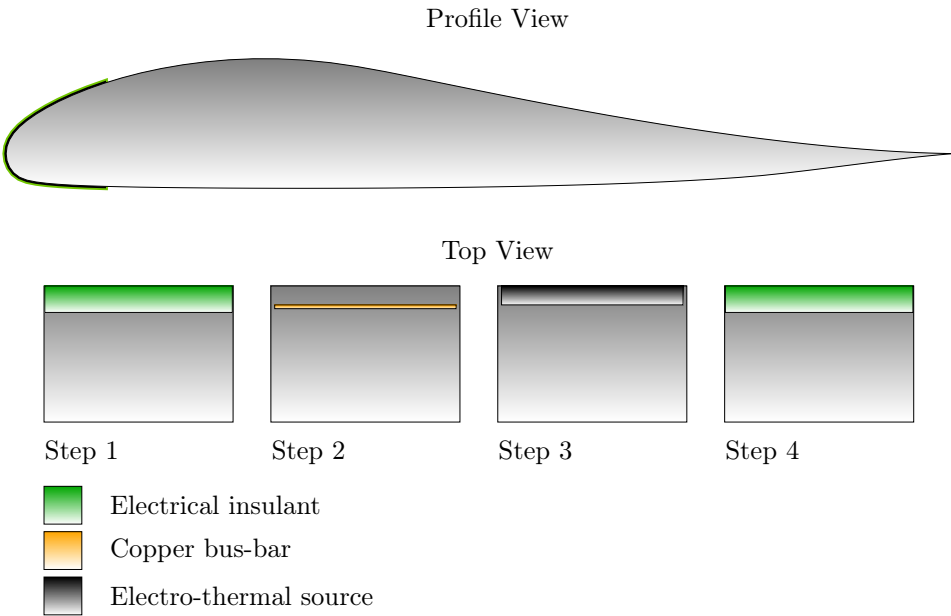
Figure 3.4: Application procedure of electro-thermal source to leading edge of aircraft wing

The last of the primary elements that constitute the solution presented here is the control unit, whose components will be presented, in detail, in the following sections.

3.2 Control Unit

The control unit depends on external inputs processed by internal components. As seen in Figure 3.2 these components combined with the external inputs form an intricate system of interconnections ultimately enabling the control algorithm to perform as required. For presentation purposes the following will take this intricate system apart, describe each component in detail, and explain how each contributes to the performance and reliability of the combined solution.

3.2.1 Air Data Estimation

The air data estimation component obtains measurements from strategically placed sensors (supplied by the air data measurements component) to provide estimates of the angle-of-attack (AOA), side-slip (SS) angle and airspeed. Such sensors could include pitot-static-tubes, pressure sensor arrays, air velocity sensors, etc.

These parameters (AOA and SS) are directly related to the performance of the aircraft, e.g. for a high angle-of-attack

Figure 3.5: Air data estimation component and interactions.

the wing is under stall conditions and the aircraft suffers from decreased lift force. Figure 3.5 display the air data estimation component and interconnections in an overall systems perspective.

Numerous algorithms have been proposed that can be applied in this setting, e.g. [78, 85–87].

3.2.2 Model-Based Icing Detection Algorithm

The **model-based** icing detection algorithm confront the issue of detecting ice when it forms on the leading edge of small UAV wings during flight operations. The algorithm addresses the issue in a fault diagnosis framework by using a mathematical model of the aircraft to detect wing surface (aerodynamic) faults, which would be the indication required to assume icing has formed on the leading edge of the aircraft wings.

Figure 3.6: Model-based icing detection algorithm component and interactions.

The proposed algorithm relies on estimates of aerodynamic parameters - obtained under nominal flight conditions - and the mathematical model of the aircraft. Should these parameters change unexpectedly a surface fault is said to have oc-

curred - icing is said to be forming on the wings of the aircraft - and the algorithm generates a signal that alerts the control algorithm of the risk.

A schematic of the model-based icing detection algorithm component and interconnected components is found in Figure 3.6. The foundation of the model-based icing detection algorithm is the mathematical model of the aircraft and several inputs from two other components, 1) are external sensor measurements in the form of angular velocities, specific force, and engine speed measurements; and 2) are the estimates provided by the air data estimation component.

A comprehensive description of the model-based icing detection algorithm is provided in Chapter 4.

3.2.3 Electro-Thermal-Based Icing Detection Algorithm

The collaborative partner to the model-based icing detection algorithm is the **electro-thermal-based** icing detection algorithm. Like its partner, the electro-thermal-based detection algorithm addresses the issue of icing detection in a fault diagnosis framework, but where the prior uses the mathematical model of the aircraft rigid-body dynamics to do this, the latter applies a model of the thermodynamic system surrounding the aircraft wings and the electro-thermal source. The model of said system includes, the composite structure of the wing and the electro-thermal source, the airflow around the wing, water layers, and an ice layer.

Figure 3.7: Electro-thermal-based icing detection algorithm component and interactions.

The electro-thermal-based icing detection algorithm introduced here operates in a form of symbiotic relationship with the control algorithm, as the prior requires the control algorithm to operate a certain control pattern, conversely the control algorithm requires knowledge about any icing instances on the wings. The control pattern mentioned allows for rapid and short temperature increases of the electro-thermal source, enabling the detection algorithm presented in this section, to obtain estimates of wing surface temperature gradients (one for each wing). For reference these gradients are estimated under nominal flight conditions (see *reference data acquisition* in Figure 3.1). If the temperature gradients change unexpectedly, from the ones obtained as a reference, a fault is said to have occurred and the algorithm produces a signal that alerts the subsequent control algorithm component to the risk of icing.

A schematic of the electro-thermal-based icing detection algorithm component and interconnected components is found in Figure 3.7. Input from the control algorithm is required to determine active electro-thermal source periods. Input from the atmospheric sensor is needed to distinguish between reference data acquisition and data acquired for the purpose of icing detection. Further inputs are supplied

Figure 3.8: Control algorithm component and interactions.

by the surface temperature sensors embedded in each wing (and electro-thermal source).

An extensive presentation of the electro-thermal-based icing detection algorithm is provided in Chapter 5.

3.2.4 Control Algorithm

The final internal component of the control unit is the control algorithm. The primary objective of this algorithm is to optimize power consumption, while mitigating or preventing ice occurrences on the leading edge of the aircraft wings. This objective is achieved through feedback control, of the electro-thermal source, using the surface temperature sensor measurements; continuously supplying redundant measurements of the electro-thermal source temperature (i.e. surface temperature of the leading edge of each wing of the aircraft). When temperature control is required, the control algorithm generates a signal to the power source component signifying how much current is allowed to flow through the electro-thermal source in a certain time period. As such the range of temperature control is tightly linked with the power source available, as well as the internal composition and structural layout of the electro-thermal source.

A schematic of the control algorithm component and interconnected components is found in Figure 3.8.

The control algorithm is primed by the inputs from the atmospheric sensor measurements component that indicate possible icing conditions through ambient temperature and relative humidity measurements. 'Primed', in this instance does not necessarily signify 'activate', as will be explained subsequently.

The control algorithm has three primary procedures, 1) icing detection, 2) anti-icing, and 3) de-icing.

- The objective of the icing detection program routine is to generate the specific temperature profiles required by the electro-thermal-based icing detection algorithm.

- The objective of the anti-icing procedure is to prevent icing from ever forming on the leading edge of the aircraft wings by ensuring that the temperature of

the electro-thermal source is maintained at a specified level above freezing. This procedure does not require rapid heating, nor high temperatures to achieve its objectives.

- The de-icing procedure mitigate, rather than prevent ice occurrences, i.e. ice accretion to a certain extent is allowed, however, once icing is detected, this procedures requires rapid heating of the electro-thermal source, and a desired temperature in the range of $T_{ETS} \in [+10, +30]°$C [31]. Hence, the de-icing procedure requires less energy, compared to the anti-icing procedure, but more power.

The three procedures listed, are presented in further detail in Chapter 6.

3.3   Summary

The presented IPS and its architecture is the first of its kind for UAVs and it distinguishes itself - comparing it to solutions for conventional aircraft - as icing is mitigated or altogether prevented autonomously. The proposed architecture enables the IPS to execute on-line and in-flight icing detection, mitigation, or prevention, ensuring safe and robust UAV operations regardless of potential atmospheric icing conditions.

The IPS is comprised of three primary elements, 1) a power source, 2) electro-thermal sources, and 3) the control unit. The proposed modular architecture of the latter is comprised of four components, where the air data estimation and the two icing detection algorithms (the model-based and electro-thermal-based icing detection algorithms) supply the control algorithm with relevant and necessary input enabling for optimal and informed control algorithms.

Chapter 4

Model-Based Icing Detection Algorithm

The following contains a detailed description of a novel icing detection algorithm, denoted the model-based icing detection algorithm. The algorithm has been developed using a structural analysis to generate relevant residuals and a statistically change detection approach has been applied to detect any unexpected wing surface changes, i.e. icing on exposed aircraft surfaces.

The model-based icing detection algorithm is based on the published work found in [75].

4.1 Model-Based Icing Detection Algorithm - Introduction

This section is divided into four subsections and should be considered introductory reading only. The first provides a brief description of the consequences icing entail for the flight envelope[1] of an aircraft. The second subsection gives an overview of the sensor suite applied in this chapter. The final two subsections presents the aircraft model, i.e. kinematics, forces and aerodynamics.

4.1.1 Icing Consequences - Aerodynamics

Aircraft operating in their respective flight envelopes maintain their aerodynamic capabilities throughout an operation. But when significant quantities of icing occurs on the leading edge of aircraft wings the flight envelope changes dramatically. As icing forms, the maximum lift provided by the wing is considerably reduced, drag is markedly increased, and the AOA is substantially limited as stall is introduces at much smaller angles.

4.1.2 Sensors

Application of the following sensor suite is assumed.

---

[1]The flight envelope signify the range of combinations of speed, altitude, angle-of-attack (AOA), etc., within which an aircraft is aerodynamically stable.

- An IMU procures measurements of angular velocities, specific force, and altitude of the aircraft.

- A pitot-static tube providing measurements of the relative velocity in the longitudinal axis of the aircraft.

- An engine speed sensor.

4.1.3 Aircraft Model - Kinematics

Let $\vec{v}_g^b = (u,\ v,\ w)$ denote the decomposition of the ground velocity vector $\vec{v}_g$, defined in the Earth-fixed local North-East-Down (NED) frame, into the BODY frame, and let $p,\ q,\ r$ be the angular rates. This allows for the aircraft kinematics to be written as

$$\dot{u} - rv + qw = a_x, \tag{4.1}$$

$$\dot{v} - pw + ru = a_y, \tag{4.2}$$

$$\dot{w} - qu + pv = a_z, \tag{4.3}$$

with acceleration components $(a_x,\ a_y,\ a_z)$ decomposed in the BODY frame. Let the wind velocity vector relative to Earth be denoted $\vec{v}_w = (u_w,\ v_w,\ w_w)$. The aircraft velocity relative to the wind velocity is then $\vec{v}_r = \vec{v}_g - \vec{v}_w$. Consequently the relative velocity in the BODY frame, denoted $\vec{v}_r^b = u_r,\ v_r,\ w_r$, can be written as

$$\begin{pmatrix} u_r \\ v_r \\ w_r \end{pmatrix} = \begin{pmatrix} u \\ v \\ w \end{pmatrix} - R_n^b \begin{pmatrix} u_w \\ v_w \\ w_w \end{pmatrix}, \tag{4.4}$$

where R_n^b is the rotation matrix from NED to BODY frame defined by the Euler angles roll, pitch, and yaw ($\phi,\ \theta,\ \psi$ respectively).

The relative velocity components u_r, v_r, and w_r are related to the airspeed V_a through

$$u_r = V_a \cos(\alpha) \cos(\beta), \tag{4.5}$$

$$v_r = V_a \sin(\beta), \tag{4.6}$$

$$w_r = V_a \sin(\alpha) \cos(\beta), \tag{4.7}$$

$$V_a = \sqrt{u_r^2 + v_r^2 + w_r^2}, \tag{4.8}$$

with α and β denoting the AOA and sideslip angle (SS). For small UAVs the AOA and SS are generally not measured, nor is the wind speed, instead they require estimation. In [88] a sensor fusion approach is applied for just this purpose, where the estimation is based on estimates of velocities and wind speeds, and on the general relations (see [26], [88], and [89])

$$\alpha = \tan^{-1}\left(\frac{w_r}{u_r}\right), \qquad \beta = \sin^{-1}\left(\frac{v_r}{V_a}\right).$$

A similar objective, but different approach, is utilised in [78], where wind velocities, AOA, and SS are estimated through kinematic relationships and a Kalman

filter, thereby avoiding the need to know aerodynamic models or other aircraft parameters. Based on either of the aforementioned estimation methods α, β, $\vec{v}_w$, and consequently V_a (denoted $\hat{V}_a$) is assumed known.

4.1.4 Aircraft Model - Forces & Aerodynamics

Let the specific force vector, decomposed in the BODY frame, be (f_x, f_y, f_z), defined as

$$f_x = a_x + g \sin(\theta), \tag{4.9}$$
$$f_y = a_y - g \sin(\phi) \cos(\theta), \tag{4.10}$$
$$f_z = a_z - g \cos(\phi) \cos(\theta), \tag{4.11}$$

where g is the gravitational constant. (f_x, f_y, f_z) is related to the aerodynamic forces and thrust force of the aircraft by

$$f_x = \frac{1}{m}(F_{a_x} + F_t), \tag{4.12}$$

$$f_y = \frac{1}{m}F_{a_y}, \tag{4.13}$$

$$f_z = \frac{1}{m}F_{a_z}, \tag{4.14}$$

where m is the aircraft mass and F_t denotes the thrust force, which is assumed to be aligned with the longitudinal axis of the aircraft. $(F_{a_x}, F_{a_y}, F_{a_z})$ are aerodynamic forces represented as a vector decomposed in the BODY frame.

The thrust developed by the engine, as presented in [26], is described by

$$F_t = \frac{1}{2}\rho S_p C_p \left(k_p^2 \omega_p^2 - V_a^2\right), \tag{4.15}$$

where ρ is the air density, S_p, C_p, k_p are propeller coefficients, where the latter specifies motor efficiency, and ω_p denotes the angular velocity of the propeller.

The focus of the fault diagnosis approach presented in this paper is confined to longitudinal and vertical change detection. For that purpose the relevant aerodynamic forces can be described by

$$F_{a_x} = \frac{1}{2}\rho V_a^2 S C_X(\alpha), \tag{4.16}$$

$$F_{a_z} = \frac{1}{2}\rho V_a^2 S C_Z(\alpha), \tag{4.17}$$

where S is the wing surface area and $\frac{1}{2}\rho V_a^2$ represents the dynamic pressure. C_x and C_z are composed of lift C_L and drag C_D coefficients and depend on α, as described in [26] and [89], i.e.

$$C_X = C_L(\alpha)\sin(\alpha) - C_D(\alpha)\cos(\alpha), \tag{4.18}$$
$$C_Z = -C_L(\alpha)\cos(\alpha) - C_D(\alpha)\sin(\alpha). \tag{4.19}$$

The aerodynamic coefficients, C_X and C_Z, are unknown quantities that require estimation. One approach to achieve this is using a standard adaptive observer updating approach as described in [53]. For the work presented in this monograph the nominal values of these, i.e. no icing, are assumed a priori known, and their non-nominal estimates (denoted $\hat{C}_X$ and $\hat{C}_Z$, respectively) are found from (4.18) and (4.19), where it is assumed that C_D, C_L, and α are estimated and available.

4.2 Fault Diagnosis

The objective of the fault diagnosis approach, presented in this section, is to detect and isolate the surface faults that occur when ice forms on the leading edge of aircraft wings. The diagnosis is complicated by model uncertainties, which can be attributed to the non measurable coefficients C_X and C_Z found in the expressions for the longitudinal and lateral aerodynamic forces. The objective is achieved through residual generation and a statistical change detection solution. The former is obtained as presented in [90] and the latter follows an approach detailed in [91].

4.2.1 Structural Analysis

Given the nonlinear model of the aircraft, described in the previous section, the following constraints for the structural analysis can be formulated

$$c_1: \quad f_x = \frac{1}{\mathrm{m}}\left(F_{a_x}(\hat{V}_a, \hat{C}_X) + F_T(\hat{V}_a, \omega_p) \right),$$

$$c_2: \quad f_z = \frac{1}{\mathrm{m}} F_{a_z}(\hat{V}_a, \hat{C}_Z),$$

$$\begin{array}{llll}
m_1: & y_1 = f_x, & m_2: \quad y_2 = f_z, & m_3: \quad y_3 = \omega_p, \\
e_1: & y_4 = \hat{V}_a, & e_2: \quad y_5 = \hat{C}_X, & e_3: \quad y_6 = \hat{C}_Z,
\end{array}$$

Note that the constraints denoted e_1, e_2, and e_3 are estimated parameters, but for the analysis to come these are considered measured parameters.

Residuals are identified using the methods described in [90] and confirmed using the Matlab tool SATool presented in [92]. Measured parameters are introduced to obtain the following expressions for $\{c_1, c_2\}$.

$$r_1 = \frac{\rho}{2\mathrm{m}}\left(y_4^2 S y_5 + S_p C_p \left(k_p^2 y_3^2 - y_4^2 \right) \right) - y_1, \tag{4.20}$$

$$r_2 = \frac{\rho}{2\mathrm{m}} y_4^2 S y_6 - y_2, \tag{4.21}$$

Note that $r_1 = 0$ and $r_2 = 0$ signify that no wing surface changes (faults) have occurred.

4.3 Simulation Study

To asses the performance of the proposed icing detection solution, this section provides the foundation for the numerical analysis that has been completed. The

numerical analysis have been conducted using Matlab and Simulink, with a sample time of 0.01s. The simulations have been based on the complete, 6-degree of freedom *Zagi* model, of the small unmanned aircraft system presented in [26], including the autopilot module, operating at cruise conditions. Measurement noise is modelled as zero-mean white Gaussian noise, $\mathcal{N}(0, \sigma_{m,*})$, with standard deviations similar to the ones found in [93], i.e. $\sigma_{m,u_r} = 0.1$ [m/s] and $\sigma_{m,f_x}, \sigma_{m,f_z} = 0.1$ [m/s^2]. Wind is modelled as a constant wind field with added turbulence, which is generated as white noise filtered through a *Dryden gust model*, an approach presented by [93] and applied in [26, 89], where the simulation environment developed in [26] serves as a basis for the simulations presented in this Chapter. The Dryden gust model was chosen for simulations as an approximation to the *Von Karman gust model*, whose spectrum does not result in rational transfer functions. The Dryden transfer functions for the wind turbulence are defined by

$$H_u(s) = \sigma_{D,u}\sqrt{\frac{2V_a}{L_u}} \cdot \frac{1}{s + V_a/L_u}, \tag{4.22}$$

$$H_v(s) = \sigma_{D,v}\sqrt{\frac{3V_a}{L_v}} \cdot \frac{s + V_a/(\sqrt{3}L_v)}{(s + V_a/L_v)^2}, \tag{4.23}$$

$$H_w(s) = \sigma_{D_w}\sqrt{\frac{3V_a}{L_w}} \cdot \frac{s + V_a/(\sqrt{3}L_w)}{(s + V_a/L_w)^2}, \tag{4.24}$$

where σ_{D*} and L_* are the turbulence intensities and spatial wavelength, respectively, along the aircraft frame axes. The gust model used is for low altitude, moderate turbulence, with numerical values for the turbulence parameters presented in Table 4.1

Table 4.1: Measurement noise levels and Dryden gust parameters

altitude,	50	[m]
L_u, L_v,	200	[m]
L_w,	50	[m]
$\sigma_{D,u}$, $\sigma_{D,v}$,	2.12	[m/s]
$\sigma_{D,w}$,	1.4	[m/s]

The surface fault, icing on the leading edge of the wing entails, has been imposed upon the aircraft as a 10% increase in the drag coefficient and a 10% decrease in the lift coefficient, which are well within the penalties described in [14, 20, 25, 30]. For clarifying purposes Figures 4.1 and 4.2 display the responses of the aircraft system to icing. The former show responses in altitude, airspeed, and pitch angle. The latter display autopilot responses, i.e. thrust and elevator displacements. The fault is imposed at $t = 500$ s with ice forming over a period lasting 120 seconds.

4.3.1 Change Detection

Fault detection is achieved by detecting changes in the residual signals (4.20) and (4.21). The proposed detection solution relies on $\hat{C}_X$ and $\hat{C}_Z$ under nominal flight
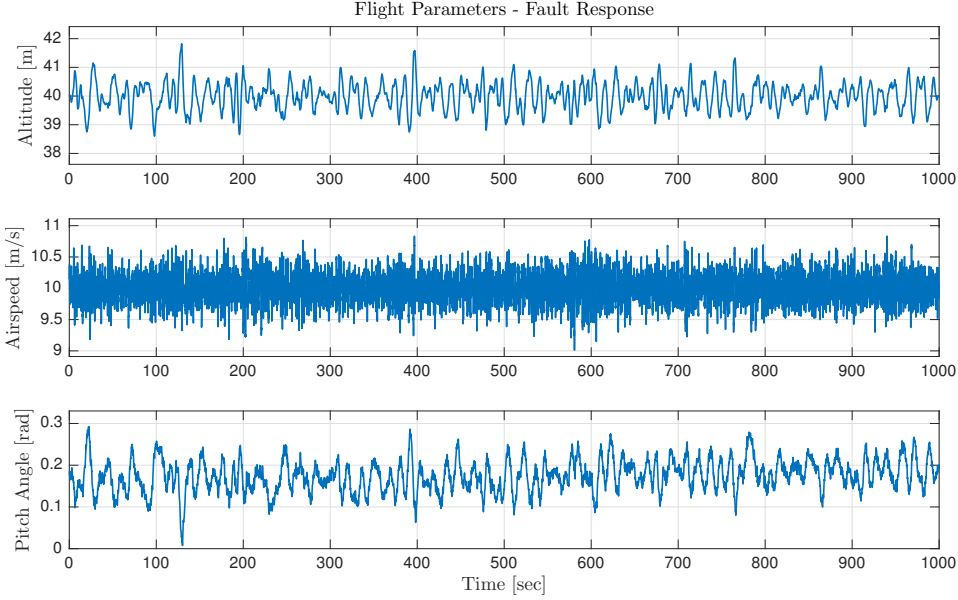
Figure 4.1: Response to surface fault- 1. altitude, 2. airspeed, 3. pitch angle.

conditions. When $\hat{C}_X$ and $\hat{C}_Z$ display unexpected changes, a bias is introduced into the residuals and a surface fault (icing on the leading edge of the aircraft wings) is said to have occurred. Note that r_1 and r_2 can be presented as

$$r_1 = \frac{\rho}{2\mathrm{m}} V_a^2 S \left(\hat{C}_X - C_X \right), \tag{4.25}$$

$$r_2 = \frac{\rho}{2\mathrm{m}} V_a^2 S \left(\hat{C}_Z - C_Z \right), \tag{4.26}$$

where $\hat{C}_* - C_* \neq 0$ whenever icing is forming on the leading edge of the aircraft wing.

The response of the two residuals and the distributions for faultless and faulty evolutions are displayed in Figures 4.3 and 4.4.

A generalised likelihood ratio test (GLRT) is used to distinguish between two hypotheses stated about the residual signal. The problem is mathematically expressed as the following detection problem.

$$\begin{aligned} \mathcal{H}_0 : x[n] &= w[n] & n = 0, 1, \ldots N - 1, \tag{4.27} \\ \mathcal{H}_1 : x[n] &= A + w[n] & n = 0, 1, \ldots N - 1, \tag{4.28} \end{aligned}$$

where x is a specific residual signal, A is unknown, $w[n]$ is white Gaussian noise with unknown variance σ^2, and N is the window size.

The $\mathcal{H}_0$ hypothesis describes the case where the signal contain the expected noise only, whereas the alternative hypothesis $\mathcal{H}_1$, other than containing the expected noise, also contain an offset A from zero. If an offset is identified it implies a significant difference between the model and the measurement, hence a fault is
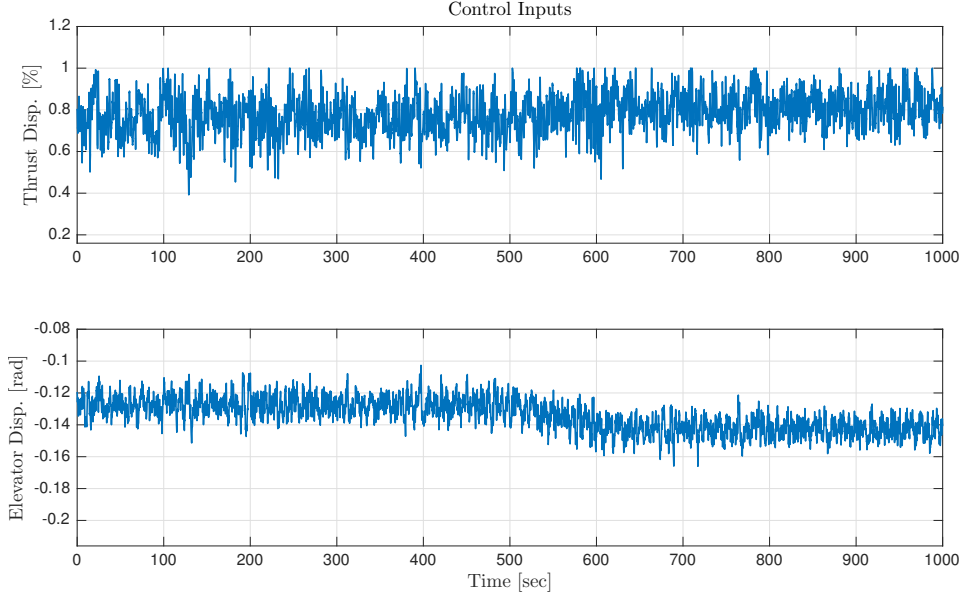
Figure 4.2: Autopilot response to surface l fault- 1. thrust displacement, 2. elevator displacement.

concluded to be present. In Figures 4.5 and 4.6 the probability plot and autocorrelation of the two relevant residuals are displayed. As seen in the figures the residuals contain uncorrelated samples.

The probability plots show that the residuals follows a Gaussian distribution with a general form

$$p(x; \mu, \sigma) = \frac{1}{\sigma\sqrt{2\pi}} e^{-\frac{(x-\mu)^2}{2\sigma^2}}. \tag{4.29}$$

The GLRT is based on the likelihood ratio between the probability of the two hypotheses given a window of data. The GLRT decides $\mathcal{H}_1$ if

$$L_G(\mathbf{x}) = \frac{p(\mathbf{x}; \hat{A}, \hat{\sigma}_1^2, \mathcal{H}_1)}{p(\mathbf{x}; \hat{\sigma}_0^2, \mathcal{H}_0)} > \gamma, \tag{4.30}$$

where $[\hat{A}\ \hat{\sigma}_1^2]^T$ is the maximum likelihood estimate (MLE) of the vector $[A\ \sigma_1^2]$ under $\mathcal{H}_1$ and $\hat{\sigma}_0^2$ is the MLE of σ_0^2 under $\mathcal{H}_0$. The decision function (or threshold) is denoted γ. $\hat{A}$, $\hat{\sigma}_1^2$, and $\hat{\sigma}_0^2$ are determined by maximising (4.29) with $\mu = A$ and $\mu = A = 0$, respectively. For the MLEs under $\mathcal{H}_1$ this results in

$$\hat{\sigma}_1^2 = \frac{1}{N} \sum_{n=0}^{N-1} (x[n] - \bar{x})^2, \tag{4.31}$$

with $\bar{x}$ being the sample mean of $x[n]$ and where $\bar{x} = \hat{A}$. For the MLE under $\mathcal{H}_0$

43
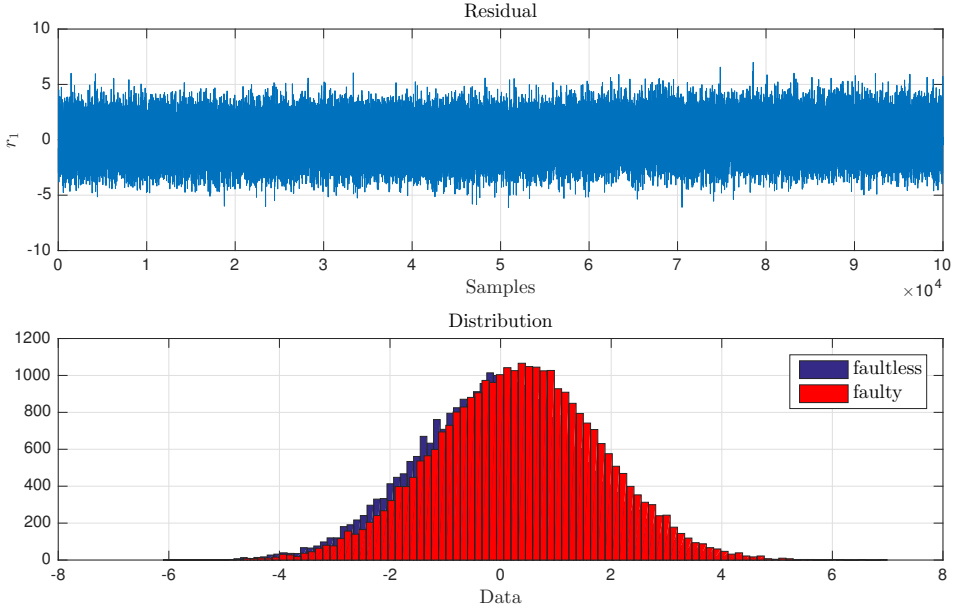
Figure 4.3: Residuals r_1 with distributions for the faultless and faulty operations.

maximising (4.29), assuming $\mu = A = 0$, leads to

$$\hat{\sigma}_0^2 = \frac{1}{N} \sum_{n=0}^{N-1} x[n]^2. \tag{4.32}$$

With this the following test statistic can be derived (see [91])

$$T(\mathbf{x}) = N \ln \left(\frac{\hat{\sigma}_0^2}{\hat{\sigma}_1^2} \right). \tag{4.33}$$

A theoretical threshold γ is determined according to the Neyman Pearson theorem found in [91]. Given a signal $f(t)$ that behaves according to the probability density function $p(f(t); \mathcal{H}_0)$ under $\mathcal{H}_0$, the threshold that maximises the probability of detection P_D is found from

$$P_{FA} = \int_{\{f : L_G(f) > \gamma\}} p(f; \mathcal{H}_0) \mathrm{d}f, \tag{4.34}$$

where P_{FA} is the desired probaility of false alarm.

Note that for the modified GLRT, here denoted $T(\mathbf{x})$, an asymptotic result exists for large data records ($N \to \infty$) [91, 94].

The probability of detecting a fault under $\mathcal{H}_1$, with probability P_D for a given threshold γ is given by

$$P_D = 1 - P(\gamma; \mathcal{H}_1, \nu, \lambda), \tag{4.35}$$

where $P(\cdot)$ is the cumulative distribution function of a given test statistics distribution.
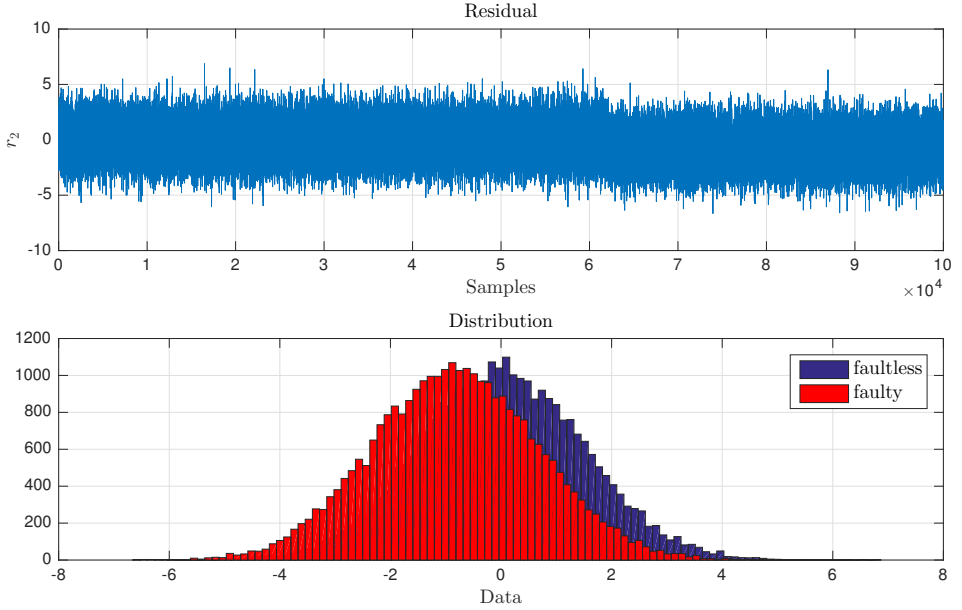
Figure 4.4: Residual r_2 with distributions for the faultless and faulty operations.

4.4 Model-Based Icing Detection Algorithm - Performance Assessment

The GLRT performance is dependant on the trade-off between the desire for a high P_D, a low P_{FA}, GLRT window size N , and the time it takes to detect the occurrence of a fault.

The test statistics, from r_1 denoted $T_{r_1}(\mathbf{x})$, approximately follow a chi-squared ($\mathcal{X}_\nu^2$) distribution under $\mathcal{H}_0$ and a non-central $\mathcal{X}_\nu'^2(\lambda)$ under $\mathcal{H}_1$, with ν and λ serving as degree-of-freedom and non-centrality parameters, respectively. For window sizes $N = \{500, 1000\}$, corresponding to 5 and 10 seconds, a visual representation can be found in Figure 4.7, which also includes thresholds for $P_{FA} = 10^{-6}$. Here it should be mentioned that parameters of the $\mathcal{X}_\nu^2$, used to fit the data, were estimated utilising MLE.

For r_2, the test statistics, denoted $T_{r_2}(\mathbf{x})$, display the same distribution characteristics as $T_{r_1}(\mathbf{x})$, i.e. $T_{r_2}(\mathbf{x})$ approximately follow a $\mathcal{X}_\nu^2$ distribution under $\mathcal{H}_0$ and a $\mathcal{X}_\nu'^2(\lambda)$ under $\mathcal{H}_1$. Choosing window sizes $N = \{100, 200\}$, corresponding to 1 and 2 seconds, the probability characteristics of $T_{r_2}(\mathbf{x})$ are displayed in Figure 4.8. The thresholds seen in the figure are for $P_{FA} = 10^{-6}$. The performance of the GLRT, for both residuals, are found in Table 4.2.

Note that wind turbulence levels significantly influence the evolution of the residuals, i.e. increased turbulence will result in a decrease in P_D, but this is easily accommodated by increasing the window size N. It is, however, the accelerometer measurement noise that is the primary contaminant. Consequently a white noise model could have limitations, as accelerometer noise might include issues such as

45
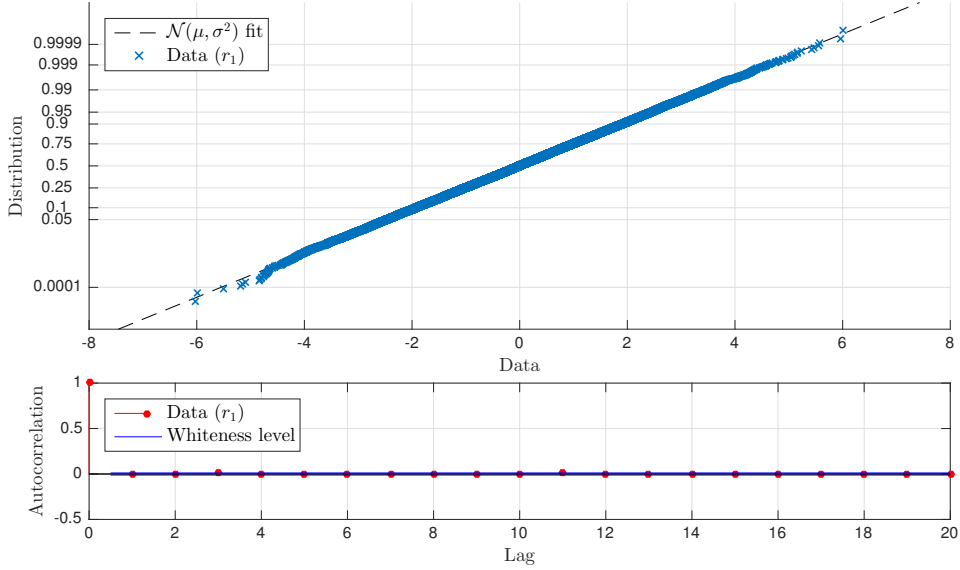
Figure 4.5: Residual r_1 data distribution fit and autocorrelation.

	$T_{r_1}(\mathbf{x})$		$T_{r_2}(\mathbf{x})$	
N	500	1000	100	200
P_{FA}	10^{-6}	10^{-6}	10^{-6}	10^{-6}
P_D	44.74%	97.84%	64.67%	99.63%

Table 4.2: GLRT performance

bias, drift, vibrations, etc. that are correlated. Correlated noise can be addressed by pre-whitening. The issue of correlated noise and any solutions to said noise is a subject deemed outside the scope of the work presented here.

4.5 Summary

Overall, the chapter presents a novel icing detection algorithm, which is validated through a numerical analysis. The main components of the algorithm are two residuals whose signals indicate any unexpected wing surface changes, i.e. the indication that ice is forming on exposed aircraft surfaces. The decision, whether any unexpected changes have occurred, is dictated through the use of a statistical change detection approach, based on hypothesis testing applying a Generalised Likelihood Ratio Test.

A simulation environment - based on the work found in [26] - has been developed to validate the proposed algorithm. Aerodynamic penalties for flying in icing conditions have been imposed upon the simulated aircraft as a 10% decrease in lift and a 10% increase in drag. These are well within the penalties specified in [14, 25]
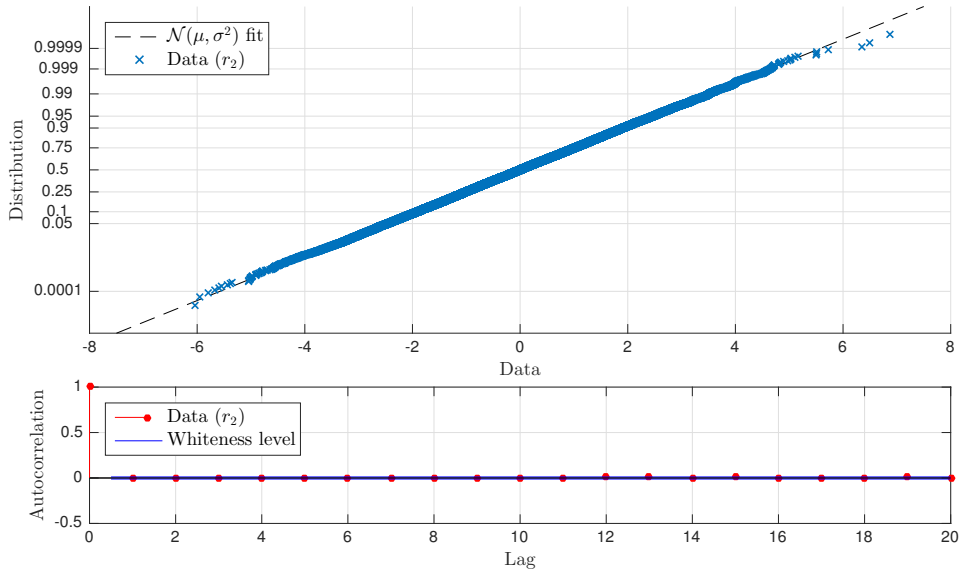
Figure 4.6: Residual r_2 data distribution fit and autocorrelation.

and [20]. With these conditions the algorithm performs as expected and is able to detect icing with up to 99% certainty and a negligible probability of raising a false alarm.
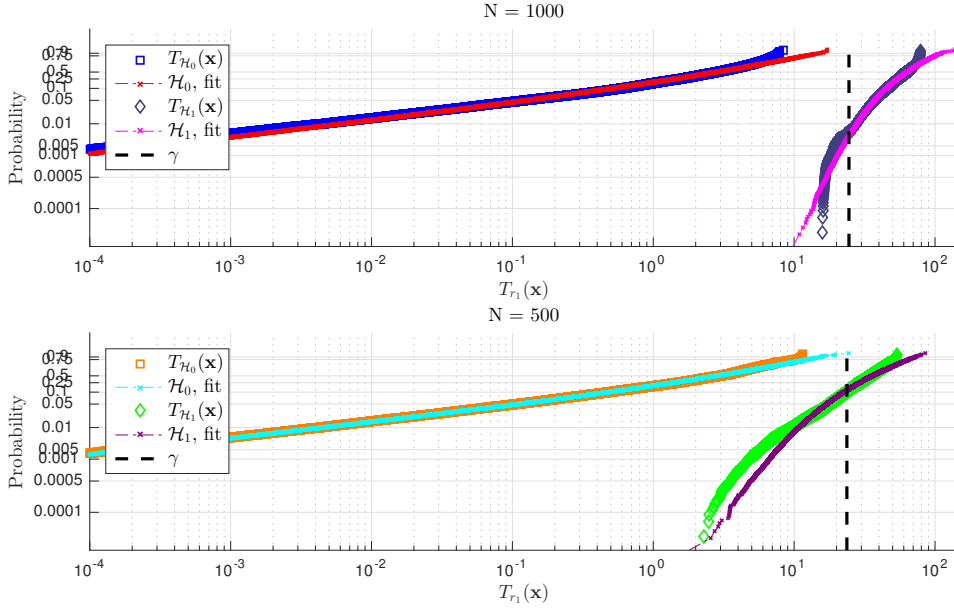
Figure 4.7: Probability plot of $T(\mathbf{x})$, for r_1, under $\mathcal{H}_0$ and $\mathcal{H}_1$ for window length $N = 500$ and $N = 1000$.
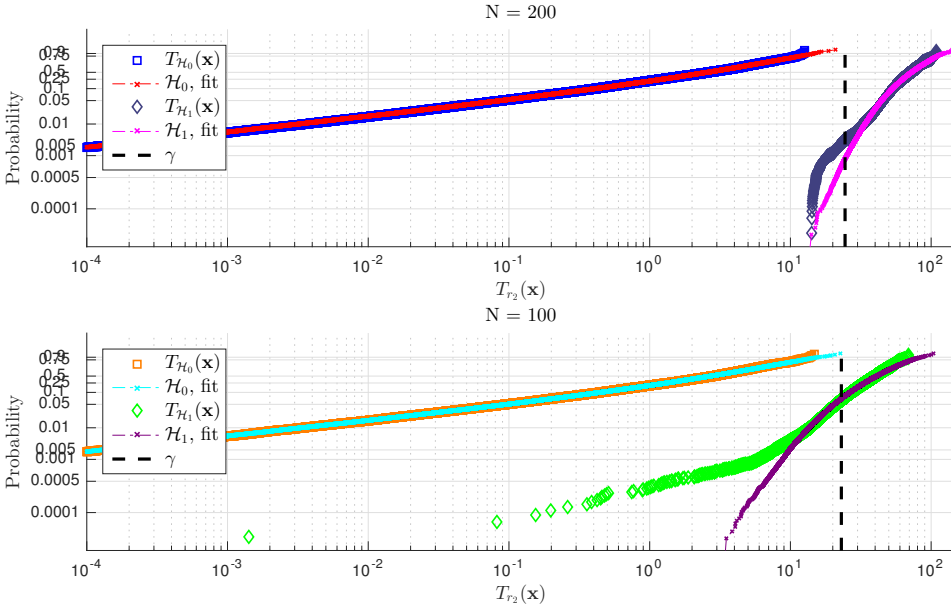
Figure 4.8: Probability plot of $T(\mathbf{x})$, for r_2, under $\mathcal{H}_0$ and $\mathcal{H}_1$ for window length $N = 100$ and $N = 200$.

Chapter 5

Electro-Thermal-Based Icing Detection Algorithm

This chapter provides a presentation of a second icing detection solution, denoted the electro-thermal-based icing detection algorithm. As for its collaborative partner, the model-based icing detection algorithm, the electro-thermal-based icing detection algorithm applies developed residuals to detect icing. The proposed solution presented in this chapter is based on the thermodynamic system surrounding the electro-thermal source, the aircraft wings and ambient conditions, rather than the nonlinear aerodynamic model of the aircraft as was the case in the previous chapter. As such the method presented in this chapter is novel in that it actively uses the solution already integrated onto the aircraft.

5.1 Electro-Thermal-Based Icing Detection Algorithm - Introduction

This section is comprised of several subsections that each introduce important elements that serve as a basis for the electro-thermal-based icing detection algorithm. The first subsection describes the thermodynamic consequences of icing conditions. The second is a brief introduction to the sensor and active elements used in the proposed solution. Finally an introduction to the underlying thermodynamics applied for this algorithm concludes the section.

5.1.1 Icing Consequences - Thermodynamics

For an aircraft operating in non-icing conditions, consider the thermodynamic system comprised of the aircraft wings, the electro-thermal source, a water layer (depending on atmospheric conditions), and the airflow surrounding the aircraft. Once icing occurs another element is introduced into this same system that greatly changes the flow of thermal energy in it. It is this change that the algorithm - presented in this chapter - evaluates in order to detect ice accretion.

5.1.2   Sensors and Active Elements

Application of the following sensors and active elements is assumed:

- An array of temperature sensors, e.g. K-type Thermocouples, embedded in the electro-thermal source providing temperature measurements of the surface of the aircraft wings.

- The electro-thermal source is activated in a specific on/off pattern enabling temperature gradient estimation.

5.1.3   Thermodynamic Theory - Wing Icing

The fundamental thermodynamic theory applied to the field of aerofoil icing was presented in Section 2.6 and will not be repeated here. As presented previously the expression for energy conservation can be formulated as

$$\dot{Q}_C + \dot{Q}_d + \dot{Q}_e + \dot{Q}_s + \dot{Q}_c = \dot{Q}_a + \dot{Q}_k + \dot{Q}_l. \tag{5.1}$$

This expression includes dissipative phenomena such as thermal conduction and convection, and additive elements as aerodynamic heating and latent heat of solidification. As a demonstration of feasibility is the objective of at this specific developmental stage, several simplifying assumptions about the thermodynamics of the system are established. As such only thermal convection will be included in the subsequent proposition. A listing of the assumptions and considerations as to their validity is supplied in the following.

- Thermal conduction ($\dot{Q}_c$) in this context implies heat flowing from the electro-thermal source to the wing structure. In the framework applied here thermal convection and conduction are initially proportional to the same temperature difference ΔT, with different proportionality coefficients k and $\bar{h}$, for conduction and convection respectively. The reason for discarding conduction of this type in the subsequent proposition relates to the ratio $\bar{h}/k$, where the core wing structure materials of the four testbed platforms, have a conductivity coefficient $k << 1$, while $\bar{h} \geq 100$ [69, 95–97]. Consequently the contribution from thermal conduction will be negligible compared to the contribution from thermal convection. Note here that the convective heat transfer coefficient is a highly intricate quantity to discern, dependant on atmospheric parameters and aerofoil design parameters alike, and that there presently are no studies quantifying a set of values in a small UAV framework.

- Sublimation, evaporation, and latent heat of solidification ($\dot{Q}_s$, $\dot{Q}_e$, and $\dot{Q}_l$, respectively) are discarded as no phase change is expected to occur during electro-thermal source temperature increases used to obtain the required data for the analyses.

- Thermal dissipation by incoming liquid water droplets ($\dot{Q}_d$) and the heat released through kinetic energy ($\dot{Q}_k$) are not included in the subsequent considerations. The dissipative term considered here is given by

$$\dot{Q}_d = \text{LWC}\beta V_\infty c_{P,w}\left(T_{ETS} - T_\infty\right), \qquad T_{ETS} \geq T_\infty, \tag{5.2}$$

and the expression for the kinetic gain can be formulated as

$$\dot{Q}_k = \text{LWC}\beta V_\infty \frac{V_\infty^2}{2}, \tag{5.3}$$

where LWC is the liquid water content in the surrounding airflow, β is the liquid water droplet collection efficiency (see [69, 70]), V_∞ is the airflow velocity (or airspeed), $c_{P,w}$ is the specific heat capacity of water, T_{ETS} is the temperature of the electro-thermal source, and finally T_∞ is the temperature of the surrounding airflow. The relatively low cruise airspeeds of the testbed platforms ($V_\infty \in [15, 20]$ m/s) lead to $\dot{Q}_d > \dot{Q}_k$ as long as the electro-thermal source is activated. Therefore, the inclusion of these two terms ($\dot{Q}_d$ and $\dot{Q}_k$) will overall contribute to the dissipating side of the thermodynamic system, with a contributory magnitude highly dependant upon T_∞. It is believed that the exclusion of these two terms is reasonable for less severe icing conditions, i.e. low values of LWC and MVD (median volume droplet diameter).

- Thermal gain by aerodynamic heating ($\dot{Q}_a$) is discarded as the surface of the aircraft are relatively smooth and cruise airspeed is low (15-20 m/s).

It should be noted that although thermal conduction into the wing core structure and into an ice layer are not considered in the icing detection model, they are part of the virtual environment applied for simulation and data generation, such that the simplified model is validated.

5.2 Proposition

Assume that, for non-icing conditions, the average temperature of the electro-thermal source ($\bar{T}_{ETS}$) depends on convective cooling and electrical heating alone, i.e.

$$\dot{q}_{sys} = -\dot{q}_C + \dot{q}_{ETS}, \tag{5.4}$$

which is based on thermal energy balance for a given thermodynamic system. Note that $\dot{q}_*$ is the heat rate measured in unit W.

In (5.4) energy out of the system is assumed to be a result of thermal convection alone and the generated energy comes from the electro-thermal source through electrical heating. For such a system, not in thermal equilibrium, with no active electro-thermal source (i.e. $\dot{q}_{ETS} = 0$), the rate of thermal dissipation ($\dot{q}_{sys}$) can be equated with the decrease in temperature of the body volume (the volume of the electro-thermal source) over time, as presented here

$$\dot{q_{sys}} = -\bar{h}A\left(\bar{T}_{ETS} - T_\infty\right) = \rho c_p V \frac{d\bar{T}_{ETS}}{dt}, \tag{5.5}$$

where ρ, c_p, V, and A are the density, specific heat capacity, the volume, and area of the electro-thermal source, respectively.

The linear time invariant system of (5.5) can be cast in in the form of

$$\frac{d\bar{T}_{ETS}}{dt} + \frac{1}{\tau}\bar{T}_{ETS} = \frac{1}{\tau}T_\infty, \tag{5.6}$$

where the thermal time constant (τ) is given by

$$\tau = \frac{\rho c_p V}{\bar{h} A},$$ (5.7)

which is a feature of the lumped capacity analysis method (or lumped system analysis) for a thermodynamic system. This method is based on the assumption that the conductive (internal) resistance to heat transfer is significantly greater than that of the convective (external) heat transfer. This assumption is inevitably related to the *Biot modulus* given by

$$\text{Bi} = \frac{\bar{h} V}{k A},$$ (5.8)

where k is the thermal conductivity of the electro-thermal source. A commonly applied 'rule of thumb' is that the error inherent in a lumped system analysis will be less than 5% for a value of Bi less than or equal to 0.1 [58].

Equation (5.6) suggests that the difference between the electro-thermal source and the surroundings, as a function of time, is given by

$$\Delta T(t) = \Delta T_0 e^{-t/\tau},$$ (5.9)

where ΔT_0 is the temperature difference $\Delta T_0 = \bar{T}_{ETS} - T_\infty$ at simulation time $t = 0$. Equation (5.9) is the mathematical interpretation of the intuitive notion that the electro-thermal source - once de-activated - assumes the temperature of the surrounding airflow at an exponentially decaying rate governed by the thermal time constant τ.

For detection purposes the expression on the right hand side of equation (5.9), including the theoretical thermal time constant of equation (5.7) serves as a reference. The left hand side of equation (5.9) is the measurable quantity. Consequently the resultant residual can be defined as

$$r \equiv \Delta T_0 e^{-t/\tau} - \Delta T(t),$$ (5.10)

where $r \approx 0$ when there is no ice and $r \neq 0$ when there is.

Note here that the term $\Delta T_0 e^{-t/\tau}$ in (5.10) is the theoretical response and that $\Delta T(t)$ is its measured equivalent. It should also be noted that the above residual is valid for steady flight with an approximately constant cruise airspeed and operational altitude.

5.3   Simulations

To demonstrate the feasibility of the proposed electro-thermal-based icing detection algorithm a simulation environment is developed and the required data generated.

5.3.1   Assumptions

The algorithm itself and the simulation environment are based on the following assumptions.

Assumption 5.1: All the physical elements of the model, i.e. thermal source, aerofoil surface, airfoil core, and surface ice are assumed to be in perfect thermal contact.

Assumption 5.2: Laminar flow near the aerofoil.

Assumption 5.3: Constant air pressure in the simulation environment.

Assumption 5.4: Constant ambient temperature (free stream flow temperature $T_\infty = $ constant).

Assumption 5.5: Uniform conditions along the span of the airfoil, which indicates that the 2D simulation environment is assumed to acquire all major aspects of the thermal response of the system. Intuitively this is a reasonable assumption as the impact of differential span-directional contributions will be negligible compared to chord-directional contributions.

The quantitative dimension of the model presented in the preceding section is based on parameter values listed here.

- The average convective heat transfer coefficient over the surface area of the electro-thermal source has been chosen to be $\bar{h} = 500$ W/m^2·K, corresponding to the value of the average convective heat transfer coefficient found in [69].
- The area size of the applied electro-thermal source is $A = 0.1155$ m^2, corresponding to an electro-thermal source layout measuring 750 mm (span length) by 154 mm (chord line length). Note that the latter quantity is a measure that include both 'under' and 'atop' of the aerofoil, as the electro-thermal source is applied around the leading edge of the aerofoil.
- The electro-thermal source volume is $V = 2.3100 \cdot 10^{-5}$ m^3, with electro-thermal source thickness chosen to be 0.2 mm.
- The density of the electro-thermal source is $\rho = 1300$ kg/m^3.
- The specific heat capacity of the electro-thermal source is $c_p = 1100$ J/kg·K.
- The conductivity of the electro-thermal source is $k = 1.00$ W/m·K.
- The power supplied to the electro-thermal source has been chosen to be $\dot{q}_{ETS} = 500$ W $\Rightarrow \dot{Q}_{ETS} = 4.32$ kW/m^2, which is well within the maximum power levels used in [33].

Note that all electro-thermal source specific parameter values have been declared by the material supplier. It should also be noted that the above parameter values lead to Bi $= 0.1$.

5.3.2 Simulation Environment

The simulation environment, used to obtain the required data for the electro-thermal-based icing detection algorithm, has been generated using the commercial COMSOL Multiphysics finite-element software package. COMSOL supports fully transient, multi-dimensional, nonlinear, thermal finite-element modelling, including temperature dependent material properties and complex boundary conditions [98].

The simulation environment developed mimics that of a wind tunnel without liquid water droplet control, i.e. the airflow in the virtual tunnel is considered

to be water vapour. The inlet airspeed (V_{in}) is $V_{in} = V_\infty = 20$ m/s and the surrounding temperature (or ambient temperature T_a) is $T_a = T_\infty = -20°$C. The simulation is initialised with an activation of the electro-thermal source, by supplying $P = 500$ W for 10 seconds. This forces the thermodynamic system out of a state of equilibrium and into a transient stage. The remainder of the simulation period (the total simulation time is 60 seconds) the electro-thermal source is dormant, as such the thermodynamic system returns to equilibrium after a certain amount of time. It is the evolution of the temperature profile during this return that the electro-thermal-based icing detection algorithm exploits. One dataset has been obtained with an icing layer applied to the leading edge of the aerofoil and one dataset without. The icing layer is approximately 5 mm thick. Figures 5.1(a) and 5.1(b) display the simulation environment and the X8 Skywalker aerofoil, with the ice layer applied to the leading edge.

(a) Airflow (in unit m/s) in the virtual environment used to obtain data for the electro-thermal-based icing detection algorithm.

(b) Airflow (in unit m/s) in the virtual wind tunnel environment - close up of applied ice layer.
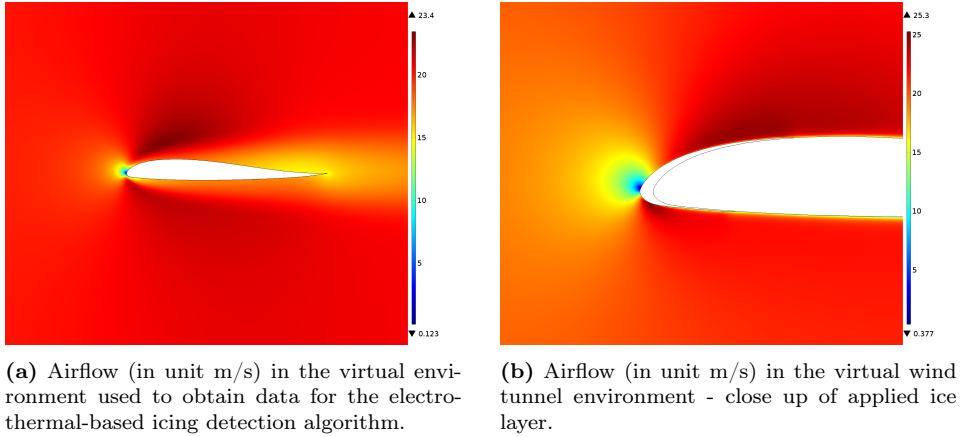
Figure 5.1: X8 Skywalker aerofoil mounted in virtual wind icing tunnel.

To obtain the necessary average temperature over the electro-thermal source area, several probes (virtual sensors) are embedded in the aerofoil, covering the range of the electro-thermal source. Their location is specified in the following table (Table 5.1). The location is expressed by an a for 'atop' or u for 'under' and by the chord line length from the leading edge of the aerofoil. Figure 5.2 illustrates the location of the virtual sensors.

Probe #	Chord Line Length [mm]	Location [a/u]
[1, 9]	[90.00, 10.00]	a
10	0.00	-
[11, 14]	[40.00, 10.00]	u

Table 5.1: Location of virtual sensors on the X8 Skywalker aerofoil.

Figure 5.2: Location of virtual sensors on the aerofoil of an X8 Skywalker platform.

5.4 Results

The results of the COMSOL simulations - the simulations required to generate the datasets for the electro-thermal-based icing detection algorithm - are displayed in Figure 5.3.
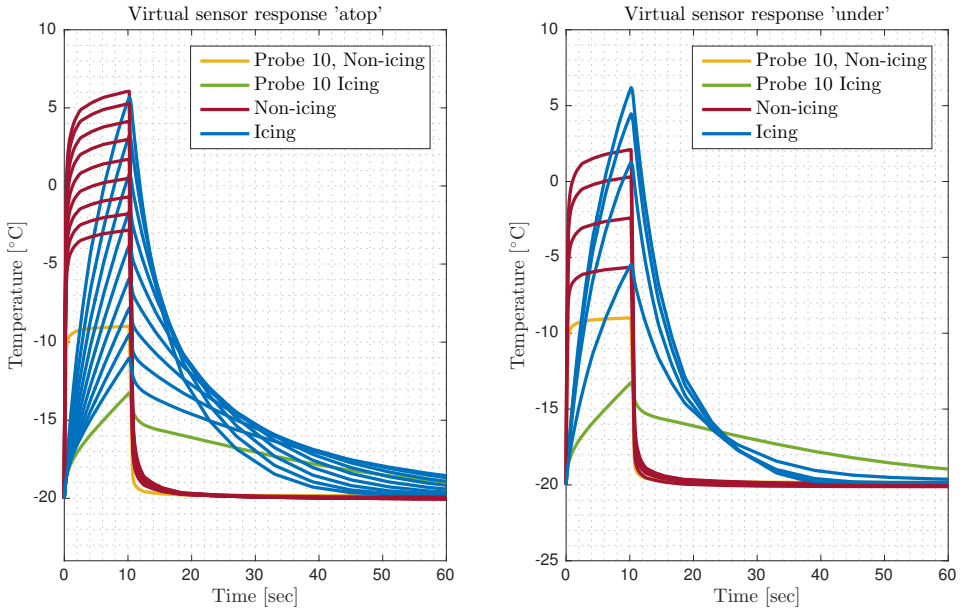
Figure 5.3: Thermal response of virtual sensors embedded in the electro-thermal source.

Reviewing the responses displayed in Figure 5.3 interesting thermal patterns are revealed from the simulations. The most relevant pattern is the profile of each response, when comparing the simulations conducted in icing with the ones conducted in non-icing conditions. These temperature profiles clearly display the intuitively expected impact of the ice layer on the thermal time constant. It is also interesting to note the temperature deviation from the virtual sensor located at the very leading edge (probe 10), to the rest of the sensors.

To visually present the proposition, Figure 5.4 includes responses of the electro-thermal source temperature (an average over all probes) for datasets obtained in

non-icing (–) and icing (–) conditions. The figure also displays the residual signal for the datasets obtained in the aforementioned simulations.
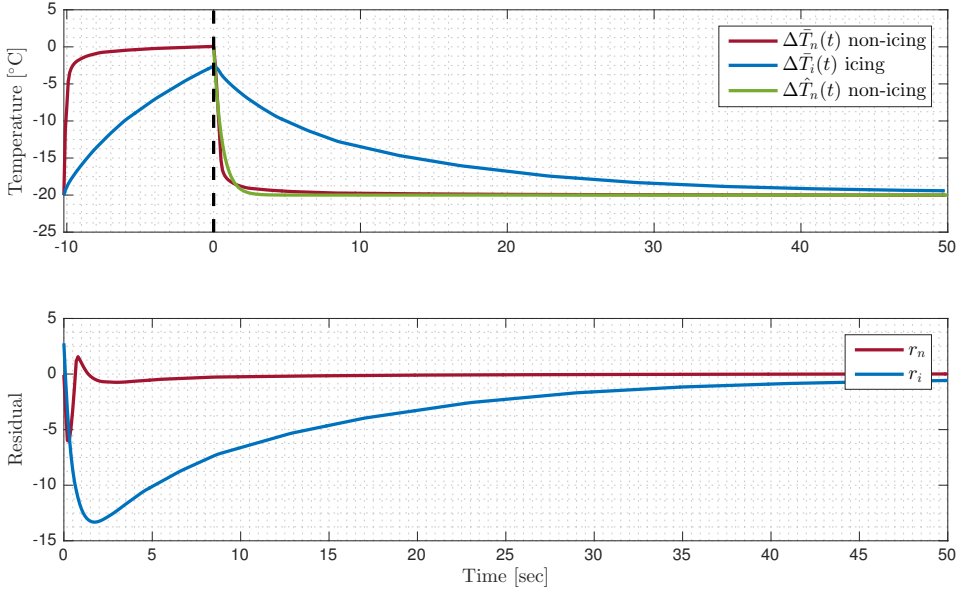
Figure 5.4: Average temperature responses, reference response, and residual responses in simulated icing and non-icing conditions.

The response denoted $\Delta \bar{T}_n(t)$ (see Figure 5.4) is the average electro-thermal source temperature for simulations conducted for non-icing conditions, while the response identified by $\Delta \bar{T}_i(t)$ display the average temperature of the electro-thermal source for simulations conducted for icing conditions. $\Delta \hat{T}_n(t)$ signifies the response of the expression found in (5.9) with the thermal constant determined by (5.7). This latter response serves as a reference (or an estimate of the temperature profile) for non-icing conditions. The two signals r_n and r_i denote the residual signal for non-icing and icing conditions, respectively.

From the residual signal responses (r_n and r_i) it is evident that - after an initial period of approximately 1-2 seconds - the settling time of the two versions of the signal clearly indicate when icing is present on the leading edge of the aerofoil.

To clarify, the residual signal is just that, one signal. The generated residual signal responses found in Figure 5.4 are merely for illustrative purposes and show the same signal responding to two atmospheric condition scenarios.

To evaluate the residual response and determine if icing is present a number of threshold methods could be applied, such as statistical change detection or adaptive threshold methods. Another approach that could be used is parameter estimation, where the thermal time constant would be estimated.

5.5 Algorithm

Reference data is obtained while the atmospheric sensor measurements indicate a relative humidity RH $\leq 50\%$ and ambient temperatures $T_\infty \leq 0°$C, parameter values that according to [81–84] ensures non-icing conditions despite sub-zero ambient temperatures. The data obtained in these conditions is used to determine the thermal time constant from (5.7) by rewriting (5.9) and integrating over the period from deactivating (t_1) to activating (t_2) the electro-thermal source.

$$\tau = \frac{1}{t_2 - t_1} \int_{t_1}^{t_2} \frac{-\theta}{\ln(\Delta T(\theta)) - \ln(\Delta T_0)} d\theta, \qquad (5.11)$$

used in the reference term of the residual (see (5.10))

Figure 5.5 displays a high level flow-chart of the electro-thermal-based icing detection algorithm.

Once icing conditions have been established and the icing detection algorithms are activated, the internal functionality of the electro-thermal-based icing detection algorithm begins. An initial heating period is required to ensure temperature variations in the electro-thermal source. Once this heating period is completed, data acquisition is conducted, where temperature measurements collected over a period (of a certain duration) is processed, thus enabling for residual evaluation. If the residual signal indicate unexpected changes, an icing alert signal is generated. Otherwise, the algorithm is idle for the remainder of a cool-off period (also of a certain duration).

Figure 5.5: High level electro-thermal-based icing detection algorithm flow-chart.
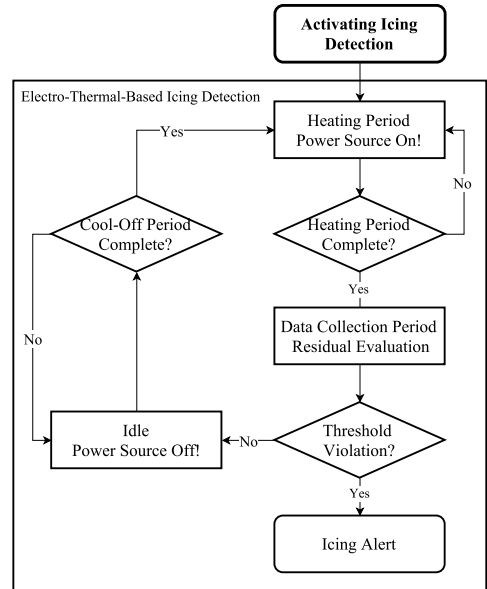
5.6 Discussion

The icing detection algorithm presented in this chapter is fundamentally different than the typical icing detection algorithms found in the literature, with the exception of [48], which will be addressed subsequently in this paragraph. The proposed electro-thermal-based icing detection algorithm actively uses the electro-thermal source, and thermodynamics rather than aerodynamics, to obtain information about icing occurrences. The algorithm relies on the responses of the thermodynamic system that includes the airflow surrounding the aircraft, the electro-thermal source applied to the leading edge of the aerofoil, and the core

structure of aircraft wing itself. This approach is somewhat similar to the one found in [48], which bases detection on changes in effective heat capacity while a thermal source is activated (i.e. heated). The approach presented in [48] is independent of the convective heat transfer coefficient ($\bar{h}$) and is based on observing changes in the initial temperature gradient. The solution presented in this chapter differs primarily in the application of the convective heat transfer coefficient. It is believed that including this enables for icing detection, where the unexpected residual change, caused by the presence of icing, is greatly enhanced. This belief is corroborated by the fact that - for the solution proposed here - it is the change from thermal convection in free airflow to conduction into ice that causes the aforementioned change, i.e. a change between coefficients ($\bar{h}$ and k) separated in value by a factor of approximately 230 [69]. This stronger indication when icing is present enhances robustness of the proposed algorithm.

Several simplifying thermodynamic assumptions have been established for the purpose of achieving the objective of demonstrating the feasibility of the proposed algorithm. These assumptions are appropriate at the present developmental stage of the algorithm, and as illustrated by the responses of the simulations conducted (see Figures 5.3 and 5.4), these simplifying assumptions do not seem to have any significant negative influence on the resultant residual signal. Here it should be noted that the simulation is conducted based on one set of assumptions that are not identical to the ones of the proposition, i.e. there are thermal flow elements included in the simulations that are not introduced into the proposed thermodynamic model.

To complete the algorithm a residual signal evaluation element is required. The choice of evaluation method is tightly connected to the further development of the thermodynamic model as other thermal phenomena are introduced. The expansion of the model could be limited as further complicating the model will not necessarily result in better icing detection performance.

5.7 Summary

This chapter has provided a novel approach to icing detection, which is validated through a simulation study. The proposed algorithm adopts a thermodynamic, rather than the typical aerodynamic, approach where a temperature gradient based residual - including a thermal time constant - is generated. The thermodynamic system consists of the electro-thermal source (applied to the leading edge of the aircraft), the core structure of the aircraft wing, and the surrounding airflow. Any unexpected changes in the residual signal will indicate that the temperature profile of the electro-thermal source (once activated) evolves in a different manor than nominal, i.e. as it would in non-icing conditions.

A simulation environment has been developed, using the COMSOL Multiphysics finite-element software package, to validate the proposed algorithm. Two datasets were generated where one served as a non-icing condition reference, the other was obtained with a small ice layer applied to the leading edge of an aerofoil. Exposed to the two datasets the residual signal clearly display a considerable change once icing is present on the leading edge og the wing, providing a solid base for icing detection.

Chapter 6

Control Unit

The IPS is built upon three primary elements, 1) the electro-thermal source, 2) an energy supply, and 3) the central control unit. This chapter provides a presentation of the control unit, briefly introduced in Chapter 3. The control unit encompasses both the hardware and the software of the IPS, so in a way it is the heart and mind of the solution. The hardware consists of microcomputers, active components, sensors, and printed circuit boards (PCB) (see Figure 6.1 for an overview). The software developed for the control unit includes the icing detection algorithms presented in preceding chapters and various data collection and processing algorithms, all of which either have been presented, or will not be presented in this monograph. Focus, for the part of the software presentation, will instead be on the description of the control algorithms and their objectives.

6.1 Objectives

The control unit has three primary objectives that are in line with the IPS objectives:

- Mitigate, or altogether prevent any occurrences of icing on exposed aircraft surfaces. The solution should enable aircraft operations in icing conditions without any incidents, or events, that would decrease operational outcome or jeopardise the aircraft.
- Minimise and optimise power consumption, i.e. efficient operations are essential.
- Modular architecture should be employed to minimise invasive system integration procedures and support scalability.

6.2 Control Unit - An Overview

The control unit is an intricate component with a web of interconnections between sensors, active components, a microcomputer, and various elements required for data logging. Figure 6.1 provides a graphical overview of the control unit and its interconnections to other external components. In this overview external sensors introduced in Chapter 3 reappear. All sensory data connections have been highlighted

with blue, where two of these connections are especially notable. These include sensor data obtained from all external (external sensors, air data sensors, atmospheric sensor, and the surface temperature sensors) and internal sensors (the power sensors). This data is collected through the PCB and redirected to the data collection component for storage and to the microcomputer for processing. Power control is based on two active devices, here represented by two metal-oxide-semiconductor field-effect transistors (MOSFET). These enable for precise power control through pulse-width-modulation (PWM) transmitted by the microcomputer to the gate of the MOSFETs.
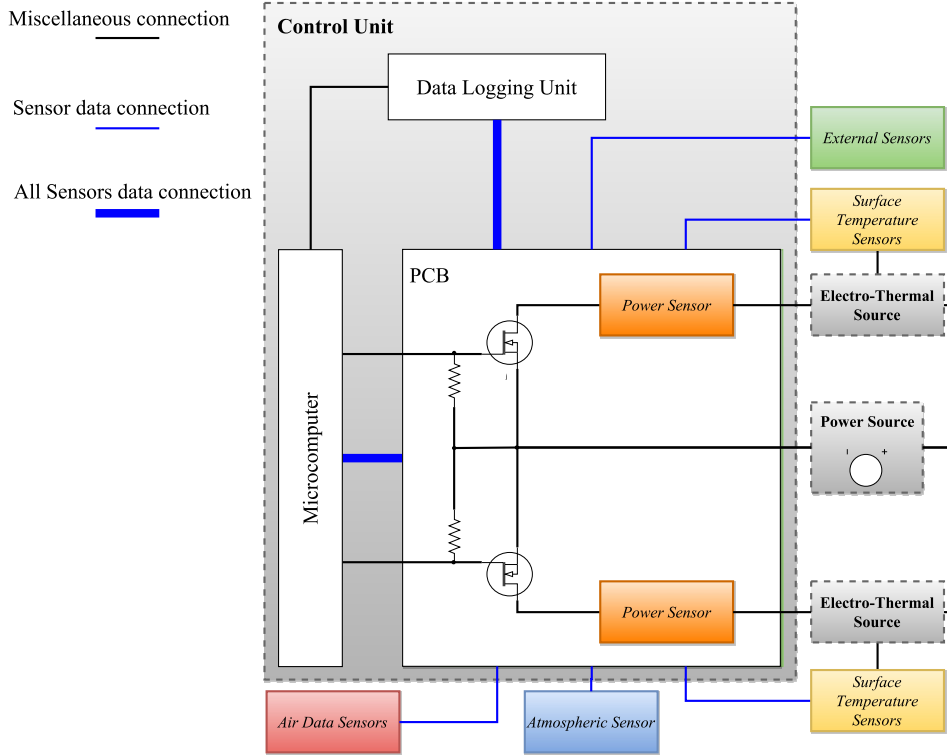
Figure 6.1: Diagram of the control unit with internal and external connections.

6.3 Sensors

Various sensor types are utilised for the IPS. These provide measurements of temperatures, humidity, and current.

The temperature sensors embedded in the wings and electro-thermal sources are analogue sensors providing a small voltage difference as a signal. This signal is amplified and digitalised before it is sent to the central control unit for processing. The atmospheric sensor package provides measurements of ambient relative humidity and temperature in a digital form. The power sensors are used to moni-

tor power consumption during active operations. They are fully digital and do not require external calibration.

6.4   PCB Design

Several prototype PCBs have been developed through the course of the work presented in this monograph. The objectives for these designs have evolved as the IPS itself has evolved, however the primary one has endured. This design objective is to enable central control data collection from all relevant sensors. Throughout the evolution of the PCB design emphasis has been on a stackable solution, i.e. the PCB could be stacked on top of the used microcomputer. Figure 6.2 displays the layout of the present prototype (version 3.0), which includes power cable connections, stack connections, current sensors, sensor connections, and active components.
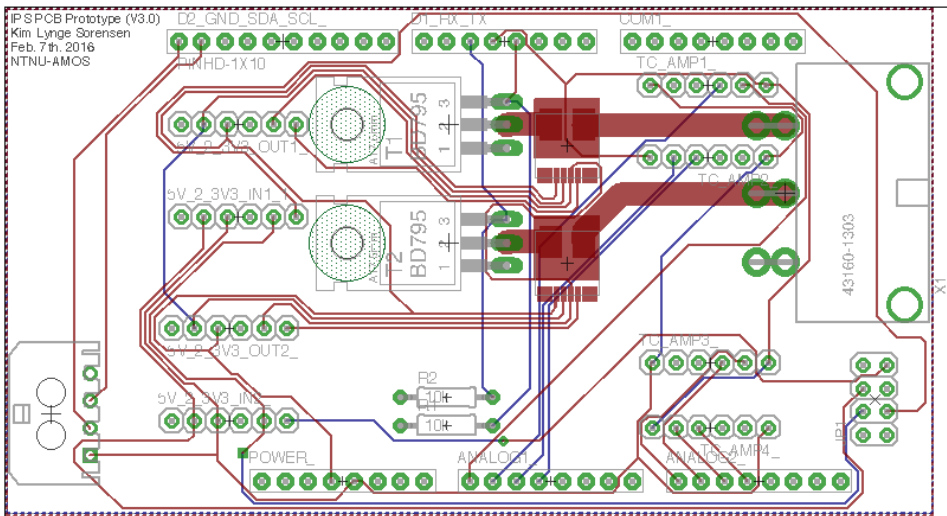
Figure 6.2: Diagram of IPS PCB design.

6.5   Control Algorithms

The objectives listed in the previous section are, in part, achieved through feedback temperature control, of the electro-thermal source, by the use of temperature sensors embedded in the wing and electro-thermal source. When temperature control is required the particular control algorithm generates a PWM signal to the MOS-FETS signifying how much current is allowed to flow through the electro-thermal sources in a given time period.

The basis for the control algorithms required for de-icing and anti-icing program routines is the proportional-integral-derivative (PID) controller, which can

be expressed in the form

$$u(t) = K_p e(t) + K_i \int_0^t e(\tau)d\tau + K_d \frac{de(t)}{dt}, \tag{6.1}$$

where K_p, K_i, and K_d, are all non-negative coefficients (or gains) for the proportional, integral, and derivative term, respectively. $u(t)$ is the control output (PWM signal) and $e(t)$ signify the error between the desired set-point for the controller and the input to the controller (electro-thermal source temperature).

Two PID controllers have been implemented in C++ using a standard microcomputer specific library that includes anti-wind-up and output saturation. One controller is used for *anti-icing* purposes and the other for *de-icing* purposes. The controller gains of each controller have been tuned to suit the requirements of the individual controller, i.e. the de-icing controller requires a more aggressive proportional term, as a rapid temperature increase is paramount, as opposed to the anti-icing controller, which is less bound by a need for a rapid temperature increase and more by energy efficiency.

The current IPS design does not include any dedicated autonomous decision algorithm, to decide which of the two control strategies to employ. This decision is presently user specified (pre-flight) and should be based on; weather forecasts; operational area, altitude, and objectives. E.g. for operations that are to be conducted above a certain cloud cover (assuming the cloud cover indicates potential icing conditions), an anti-icing strategy could be a viable option as any icing occurrences should be prevented during ascend and descend periods only. For operations that are conducted in altitudes and conditions where cloud covers (again sustaining potential icing conditions) would be frequently encountered, a de-icing approach would ensure that icing was mitigated when present only, thereby minimising power consumption.

Apart from the two control algorithms another program routine (or procedure) was developed for icing detection data collection. Thus the control algorithm has three primary procedures, 1) icing detection, 2) anti-icing, and 3) de-icing. Figures 6.3(a) and 6.3(b) display flowcharts of the higher level IPS operation for the anti-icing and de-icing program routine, respectfully. The icing detection activities are identical to the anti-icing ones, with the exception that it performs its task in all conditions, not just icing conditions.

6.5.1   Icing Detection

The icing detection procedure described here is the second part in the symbiotic relationship presented previously between the electro-thermal-based icing detection algorithm and the control algorithm. As the prior requires a certain temperature pattern to obtain estimates of surface temperature gradients, the latter provides by generating PWM signals to the MOSFETs that allow for rapid energy bursts (consequently temperature variations) through the electro-thermal source. This procedure is always active as the electro-thermal-based icing detection component requires reference estimates under nominal flight conditions. The control routine applied for this procedure enables for rapid and short bursts of energy supply to the

(a) Flow-chart for the anti-icing program routine.

(b) Flow-chart for the de-icing program routine.
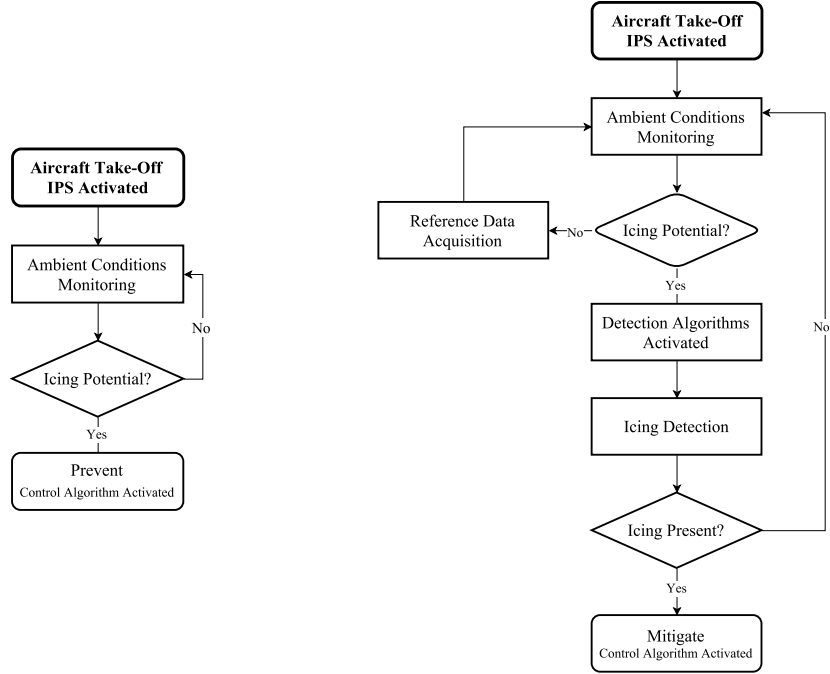
Figure 6.3: High level IPS operational flow-chart for two of the three control algorithm procedures.

electro-thermal source, resulting in rapid and short bursts of temperature increase and decreases. Energy is supplied for 10 seconds, followed by a 50 second period of temperature decrease.

Note that the icing detection procedure operates without any desired set-point temperature.

6.5.2 Anti-Icing

As described previously, the objective of the anti-icing procedure is to prevent icing occurrences on the leading edge of the aircraft wings by ensuring that the temperature of the electro-thermal source is maintained at a specified level (a desired set-point) above freezing. This objective is achieved through a feedback control approach, where the control algorithm uses the input received from temperature sensors embedded in the wings and electro-thermal sources, and a pre-defined temperature set-point (desired electro-thermal source temperature). This procedure is only active when primed by the atmospheric sensor measurements. The desired set-point temperature for the anti-icing procedure is chosen off-line prior to aircraft operations. For the purpose of minimising power consumption the desired set-point temperature should be maintained marginally above freezing, where this

margin is relatively independent of changes in freezing temperatures or other atmospheric phenomena. Consequently the primary influence of this margin is related to uncertainties in electro-thermal source temperature measurements.

6.5.3   De-Icing

All De-icing systems are designed to mitigate rather than prevent ice occurrences. This is also the true for the de-icing procedure developed for the IPS presented in this monograph. Mitigation indicates that ice should be allowed to form on exposed aircraft surfaces and indeed this is what the de-icing procedure requires to perform as expected. Once icing has been detected, the de-icing procedure is activated, consequently the control algorithm generates a PWM signal to the active components allowing for a succession of shorter energy bursts to the electro-thermal sources, each burst followed by a longer period where no energy is supplied. This process should result in momentary ice occurrences on the exposed aircraft surfaces followed by a rapid temperature increase enabling aerodynamic ice shedding. This procedure is only active when icing has been detected on the exposed aircraft surfaces.

Convectional electro-thermal de-icing systems are full-power cyclic systems, i.e. they have an active electro-thermal source for a fixed time period, regardless of when any icing occurrences are removed. Naturally this is sub-optimal from a power consumption perspective. One solution to address this issue could be to apply a similar approach as presented in Chapter 5, accordingly use the thermal time constant as an indicator for ice removal and not just ice accretion.

The de-icing procedure operates with a desired set-point temperature based on the findings presented in [31], well above 0°C temperatures.

It is worth noting that the anti-icing procedure has a lower peak-power requirement than that of the de-icing procedure. However, due to the nature of the two different procedures, anti-icing will also require a larger conversion of energy (average power) than de-icing.

6.6   Summary

The central control unit of the IPS, presented in this chapter, consists of both hardware and software. Microcomputers, active components, sensors, and PCBs comprise the hardware, and icing detection algorithms, various data collection and processing algorithms, and temperature control algorithms, make up the software.

The listed design objectives have been achieved through the development of a PCB that serves as a connectivity and data gathering hub for various sensors, a data collection component, a microcomputer, electro-thermal sources, and the power source.

Three different control procedures form the base of the control units purpose. The three procedures rely on the control algorithm generating appropriate PWM signals to two transistors that enable power control and consequently temperature of the electro-thermal source.

Chapter 7

Thermodynamic Analyses

This chapter represents a proof of concept study including analyses of a thermodynamic system, here comprised of an aircraft wing profile element (aerofoil), an electro-thermal source, and the surrounding airflow. The analyses are based on simulations applying a transient finite element approach to account for the multidimensional boundary conditions that vary along the chord of the aerofoil. The analyses are conducted on all four testbeds (see description in Section 2.4 found in the Introduction) and extends the published work found in [77].

7.1 Proof-of-Concept Study

When aircraft operations occur in non-icing conditions the aforementioned thermodynamic system is in thermal equilibrium, i.e. there is no exchange of thermal energy between the individual elements of the system. However, if the ambient conditions change and the aircraft operates in potential icing conditions the IPS will drive the thermodynamic system out of equilibrium and energy will begin to flow. The analyses presented here are conducted to investigate the thermal flow and especially dissipation when the electro-thermal source is activated in a virtual flight environment.

7.1.1 Objectives

One of the primary objectives of the study is to investigate the thermal distribution generated by activating an electro-thermal source applied to the leading edge of an aerofoil. Another is to investigate the relationship between thermal dissipation to the electro-thermal source area size. Based on this the layout of the electro-thermal source - currently applied for the IPS presented in this monograph - is evaluated.

7.1.2 Conceptual Considerations

When the electro-thermal source is activated, energy begins to flow in the form of heat. Heat always flow from hot to cold, consequently heat begins to flow from the electro-thermal source to the surrounding environment and into the airfoil struc-

ture. The relevant heat flow for these thermodynamic analyses occurs as thermal conduction and thermal convection.

Note that the analyses presented here do not include any thermal dissipative contributions, as impinging liquid water droplets, evaporation, sublimation; nor does it include any thermal gain contributions of the sort: aerodynamic, kinetic, or latent heat of solidification. Some of these are not included as they have been deemed insignificant (see Section 2.5.3), others will enter the analyses at a later stage. The thermal contributions from latent heat of solidification, sublimation, and evaporation are omitted as phase change and any related atmospheric phenomena are not introduced into the simulation environment.

The following is provided to explain the foundation for considerations regarding the electro-thermal source layout.

Consider the thermodynamic system influenced only by thermal convection and the energy supplied by an electro-thermal source,

$$\rho c_p V \frac{d\bar{T}_{ETS}}{dt} = -\bar{h} A \left(\bar{T}_{ETS} - T_\infty \right) + \dot{Q}_{ETS}, \tag{7.1}$$

where it should be noted that $\dot{Q}_{ETS}$ is the electro-thermal source heat rate in unit W. With

$$\tau = \frac{\rho c_p V}{\bar{h} A}, \tag{7.2}$$

and rearranging (7.1) the following can be obtained.

$$\frac{d\bar{T}_{ETS}}{dt} = -\frac{1}{\tau}\bar{T}_{ETS} + \frac{1}{\tau}T_\infty + \frac{1}{\rho c_p V}\dot{Q}_{ETS}. \tag{7.3}$$

Assuming thermal equilibrium at a constant $\dot{Q}_{ETS}$, (7.3) can be rewritten into

$$\bar{T}_{ETS} = T_\infty + \frac{1}{\bar{h} A}\dot{Q}_{ETS}. \tag{7.4}$$

Note that the considerations presented here are based on an assumption of steady flight, where the airspeed and operational altitude are approximately constant. Although airspeed would be the most significant influent, any sudden changes in one or both of these could influence the thermal flow in the thermodynamic system presented.

Equation (7.4) is interesting as it shows - aside from a minor offset - an inverse proportionality between the electro-thermal source temperature and area size, respectively, constrained by the assumption that a constant power is supplied. Thus, decreasing the electro-thermal source area size by 50% entails an increase in attainable temperature by 100%. Or for the scenario where a steady $\bar{T}_{ETS}$ is required, then a similar decrease in electro-thermal source area size would require only half the power supplied. It should also be noted that $\bar{T}_{ETS}$ is dependant upon the inverse of the convective heat transfer coefficient ($\bar{h}$), which itself is implicitly a function of the airspeed. Generally an increase in airspeed entails an increase in $\bar{h}$. For $\bar{T}_{ETS}$ in (7.4) an increase in airspeed would mean a decrease in steady state temperature and conversely for a lower airspeed.

7.1.3 Assumptions

The analyses are based on the following assumptions.

Assumption 7.1: All the physical elements of the model, i.e. thermal source, aerofoil surface, and airfoil core are assumed to be in perfect thermal contact

Assumption 7.2: Laminar flow near the aerofoil.

Assumption 7.3: Constant air pressure in the simulation environment.

Assumption 7.4: Constant ambient temperature (free stream flow temperature T_∞ = constant).

Assumption 7.5: Uniform conditions along the span of the airfoil; This indicates that the 2D simulation environment is assumed to acquire all major aspects of the thermal response of the system. This is reasonable as the impact of differential span-directional contributions will be negligible compared to chord-directional contributions.

Assumption 7.6: Due to the intricate nature of the core design of the Aeromapper platform, simulations concerning this test bed UAV have been conducted with a core composed of balsa wood entirely.

7.2 Feasibility

Transient thermodynamic analyses are conducted to investigate the thermal distribution surrounding the electro-thermal source and to the characteristics of the current employed electro-thermal source layout. They are based on models of each test bed platform aerofoils and will include all relevant properties regarding aerofoil surfaces and core structures. The electro-thermal source of the IPS is modelled as a resistive heating element, applied to the leading edge of the aerofoils. The analyses encompasses two of the three fundamental heat transfer processes; thermal conduction, as thermal energy flows from the electro-thermal source to the surface and core structure of the aerofoil; thermal convection, caused by the temperature difference between ambient and the electro-thermal source. The final fundamental heat transfer process is thermal radiation, whose contribution has been deemed relatively insignificant as described in 2.5.3 and corroborated in [66, 67].

The simulation environment is based on the parameter values presented in Section 5.3.1, except those regarding electro-thermal source layout, i.e. area and consequently volume, which will be specified individually where relevant (electro-thermal source layer thickness is the same as specified in the aforementioned section).

The structural composition of the specific aircraft platform has significance in the study presented here. The structural composition of the Dragon Eye and the Puma UAV platforms is identical, with a core of expanded polystyrene foam covered by a thin Kevlar surface coating. The X8 Skywalker UAV platform is made up of polyolefine alone. The Aeromapper UAV platform has a three component structure consisting of a core of air and Balsa covered by a surface layer of carbon fibre.

7.2.1   Simulations and Results

Using the COMSOL Multiphysics software package, a simulation environment has been developed, corresponding to that of the controlled environment in a wind icing tunnel. The virtual wind icing tunnel (VWIT) developed here, measures 1.00 m in width and 0.50 m in height. Inlet airspeed is $V_\infty = 20.00$ m/s, ambient VWIT temperature is $T_\infty = -20.00$ °C, liquid water content is 1.10g/m^3 [33], and simulation time is $t = 60$ seconds. The electro-thermal source is activated, with a power supply of $P_{ETS} = 500$ W (power level chosen based on experiments and flight tests), after 20 seconds of simulation time and is maintained for the remaining duration of the simulation.

The aerofoil has been fitted with several virtual sensors (or probes) that supply temperature measurements of the aerofoil surface, as illustrated in Figure 7.1 and explained by Table 7.1, where the location is expressed by a t for 'top' or u for 'under' and by the chord line length from the leading edge of the aerofoil. Figure 7.3(a) displays the thermal distribution (at simulation time $t = 60$ seconds) of an X8 Skywalker UAV platform aerofoil fitted with the electro-thermal source in the present layout, with area size $A_p = 0.1155$ m^2. Note here that the colour bar on the right hand side of Figure 7.3(a) is in unit degrees Celsius.

Figure 7.1: Location of virtual sensors on the aerofoil of an X8 Skywalker platform, for a thermodynamic analysis with present electro-thermal source layout.

To investigate the penalties and benefits of decreasing the area size of the electro-thermal source layout, simulations with an alternative layout are conducted. This proposed alternative layout has an area size of $A_a = 0.0566$ m^2, approximately half the size of A_p. The thermal distribution response (at simulation time $t = 60$ seconds) for a simulation conducted with the alternative electro-thermal source layout is displayed in Figure 7.3(b). Note here again that the colour bar on the right hand side of the figure is in unit degrees Celsius. The location of the virtual sensors - for the alternative electro-thermal source layout - is displayed in Figure 7.2 and is explained by Table 7.1.

Figures 7.3(a) and 7.3(b) clearly illustrate the different temperature distributions of the two electro-thermal source layouts (present and alternative). One important aspect to note is that the primary temperature increase for the present layout is located farther back on the aerofoil as opposed to the alternative. Further the lower temperature increase of the present layout is considerable, as is more clearly displayed in Figure 7.4, where the virtual sensor responses are shown. The temperature responses from the two different electro-thermal source layouts reveal that the temperature increases experienced by the alternative layout is ample, with
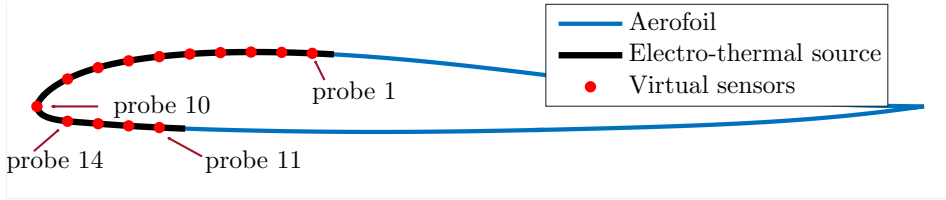
Figure 7.2: Location of virtual sensors on the aerofoil of an X8 Skywalker platform, for a thermodynamic analysis with alternative electro-thermal source layout.

Probe #	Chord Line Length [mm]	Location [t/u]	Layout [p/a]
[1, 9]	[90.00, 10.00]	t	p
10	0.00	-	p
[11, 14]	[40.00, 10.00]	u	p
[7, 9]	[30.00, 10.00]	t	a
10	0.00	-	a
[12, 14]	[30.00, 10.00]	u	a

Table 7.1: Location of virtual sensors on the X8 Skywalker aerofoil, for thermodynamic simulations of present and alternative electro-thermal source layouts.

a maximum measured temperature of the present layout reaching approximately 12°C, while the maximum obtained temperature for the alternative layout is just short of 29°C. It should also be noted that the measurements obtained by the probe located at the very leading edge of the aerofoil (probe 10), indicates that $P_{ETS} = 500$ W is not enough power for the present layout to achieve a temperature above freezing. The opposite is true for the alternative layout, where the temperature of probe 10 reaches approximately 2.5°C.

A comparison of the average temperatures of the two layouts and an average temperature of the present layout, but with the same sensor locations as the alternative layout, is displayed in Figure 7.5. The purpose of this latter average temperature (represented by LE - leading edge - in the figure) is to illustrate the difference in performance of the two layouts, at the location where it matters most, i.e. the leading edge of the aircraft. The responses indicate that for the present layout the thermal impact is greater further back on the aerofoil, illustrated by the temperature difference between the two 'Present' responses. Another interesting aspect illuminated by '$\bar{T}_{ETS}$ Pre. (LE)' is that the temperature increase of the alternative layout is approximately twice that of the present one, aligning the theoretical considerations presented in Section 7.1.2 with the findings from the simulations.

To further elaborate the correlation between the aforementioned theoretical considerations with findings from the simulations, the alternative electro-thermal source layout was tested with $P_{ETS} = 250$ W, i.e. half of the power supplied in the original simulations. The responses from these simulations, and the responses

(a) Thermal dissipation for present electro-thermal source layout.

(b) Thermal dissipation for an alternative electro-thermal source layout.
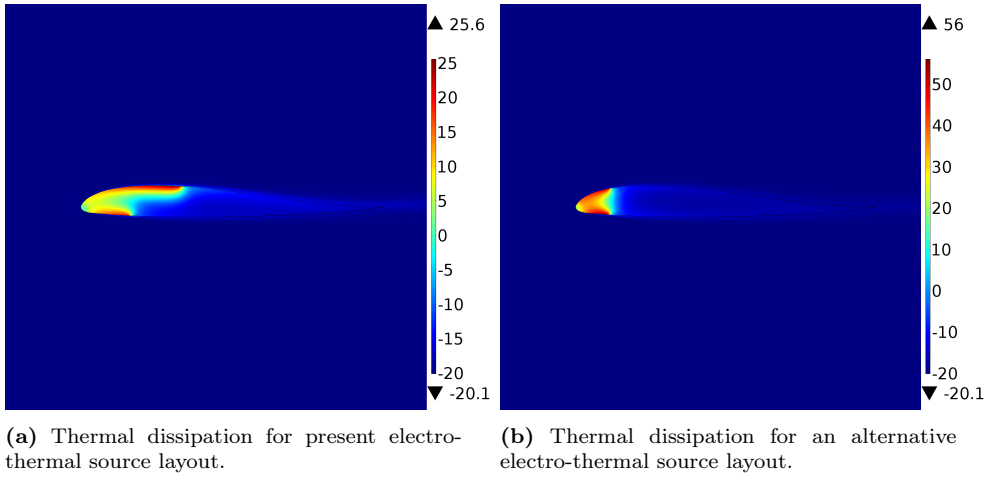
Figure 7.3: Thermal dissipation of the X8 platform, with the present and an alternative electro-thermal source layout. Power supplied is 500 W.
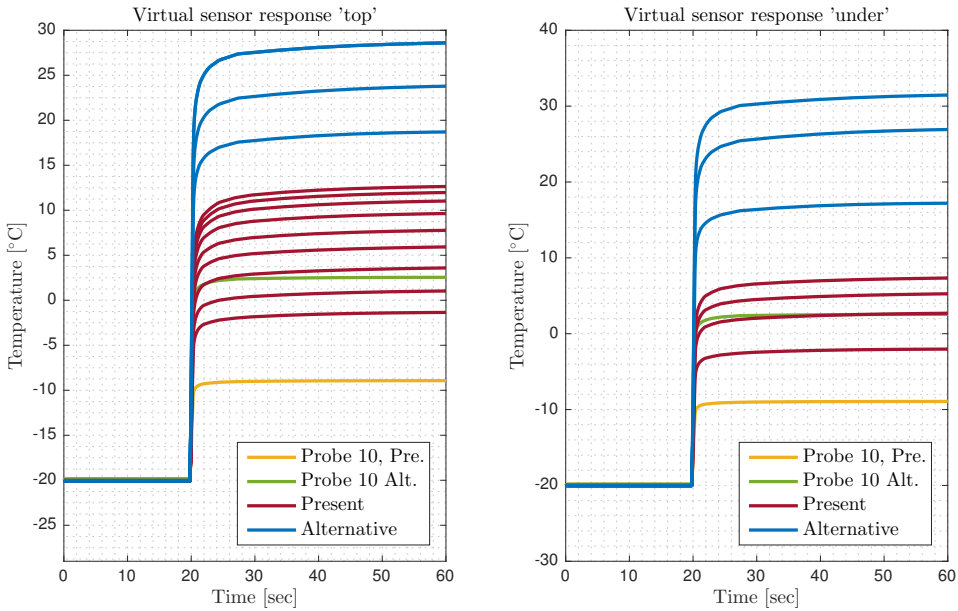
Figure 7.4: Temperature responses for present and alternative electro-thermal source layout, with power supplied $P_{ETS} = 500$ W.

from the original simulations with the present electro-thermal source layout, are displayed in Figures 7.6 and 7.7. As clearly illustrated in the figures the virtual sensors provide responses, from the two different scenarios, that are very similar. The minor discrepancy seen in the responses, when comparing the individual probes from each scenario, could be attributed to the assumption that the average
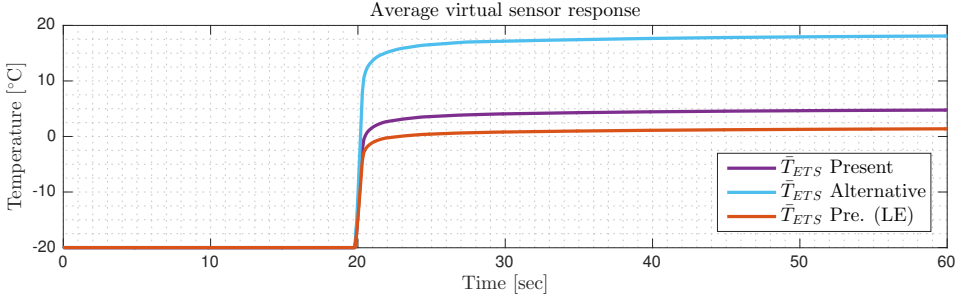
Figure 7.5: Average temperature responses for present and alternative electro-thermal source layout, with power supplied $P_{ETS} = 500$ W.
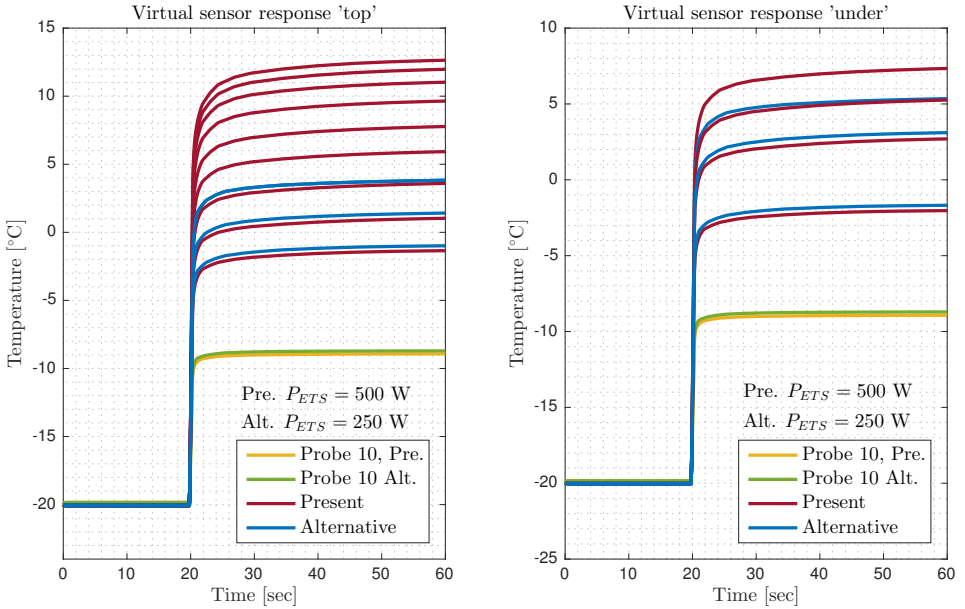
Figure 7.6: Temperature responses for present and alternative electro-thermal source layout, with power supplied $P_{ETS} = \{250, 500\}$ W.

convective heat transfer coefficient $\bar{h}$ is identical for each electro-thermal source layout.

A second set of simulations have been conducted to investigate thermal distribution differences that might occur from one UAV platform to another. The simulation environment is based on the parameter values presented in Section 5.3.1. The electro-thermal source layout and area size is similar to the alternative layout presented previously in this chapter, i.e. the area size is approximately 0.1155 m^2 for all four platforms. Power supplied to the electro-thermal source was $P_{ETS} = 500$ W and simulations were conducted over a period of 60 seconds. Figures 7.8(a) - 7.8(d) display the thermal distribution over all four UAV platform electro-thermal

71
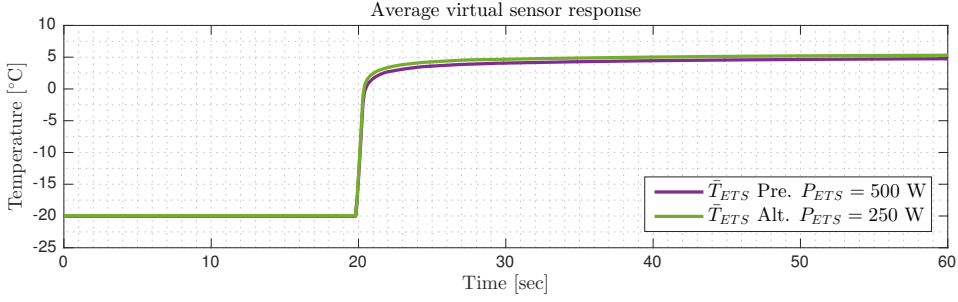
Figure 7.7: Average temperature responses for present and alternative electro-thermal source layout, with power supplied $P_{ETS} = \{250, 500\}$ W.

sources at simulation time $t = 60$ seconds, while figure 7.9 and 7.10 show the temperature responses from the virtual sensors located as presented in Table 7.1 and illustrated in Figure 7.2. Note that the colour bars to the right hand side of figures 7.8(a) - 7.8(d) are in unit degrees Celsius.

The thermal distributions displayed in figures 7.8(a) - 7.8(d) clearly show how heat is forced around the outer aerofoil surface and back by the incoming airflow. The figures also show that the core structure is significant with regards to thermal conduction, as the Balsa wood - i.e. the core structural component of the Aeromapper UAV platform - displays far superior thermal insulation characteristics than the Polyolefine and Polystyrene of the X8 Skywalker, Puma, and Dragon Eye UAV platforms. Here assumption 7.6 needs to be reiterated, which states that *due to the intricate nature of the core design of the Aeromapper platform, simulations concerning this test bed UAV have been conducted with a core composed of balsa wood entirely.* Another facet to note is attainable temperature of each platform, where the Puma seems to be able to achieve a higher temperature. This is most likely related to the thickness of the aerofoil and is not an indicator of the efficiency of the electro-thermal source itself, as it is measure of an accumulated temperature located in the core structure of the aerofoil, hence not an surface temperature.

The left side of Figure 7.9 displays the responses of probe 10 located at the leading edge of each aerofoil. The right side of the figure shows temperatures averaged over all the probes virtually embedded in the electro-thermal sources of each UAV platform. When inspecting the entirety of the figure, it could be hypothesised that generally aerofoils with a sharper leading edge (like the Aeromapper, Puma, and to an extent the X8 Skywalker) will tend to have a lower leading edge temperature and significantly higher temperatures further back on the aerofoil, i.e. the uniformity of the electro-thermal source is at a lower level. Conversely aerofoils with a more rounded leading edge (like the Dragon Eye) will have a higher leading edge temperature and only marginally higher temperatures further back on the aerofoil, thus a more uniform thermal distribution in the electro-thermal source. This hypothesis is corroborated by the temperature responses displayed in Figure 7.10, where the virtual sensors measurements for each aerofoil are included. Clearly the temperature responses obtained from the Dragon Eye display a more uniform temperature distribution over the electro-thermal source, while the other

(a) Thermal distribution around the Puma UAV platform.

(b) Thermal distribution around the Aeromapper UAV platform.

(c) Thermal distribution around the X8 Skywalker UAV platform.

(d) Thermal distribution around the Dragon Eye UAV platform.
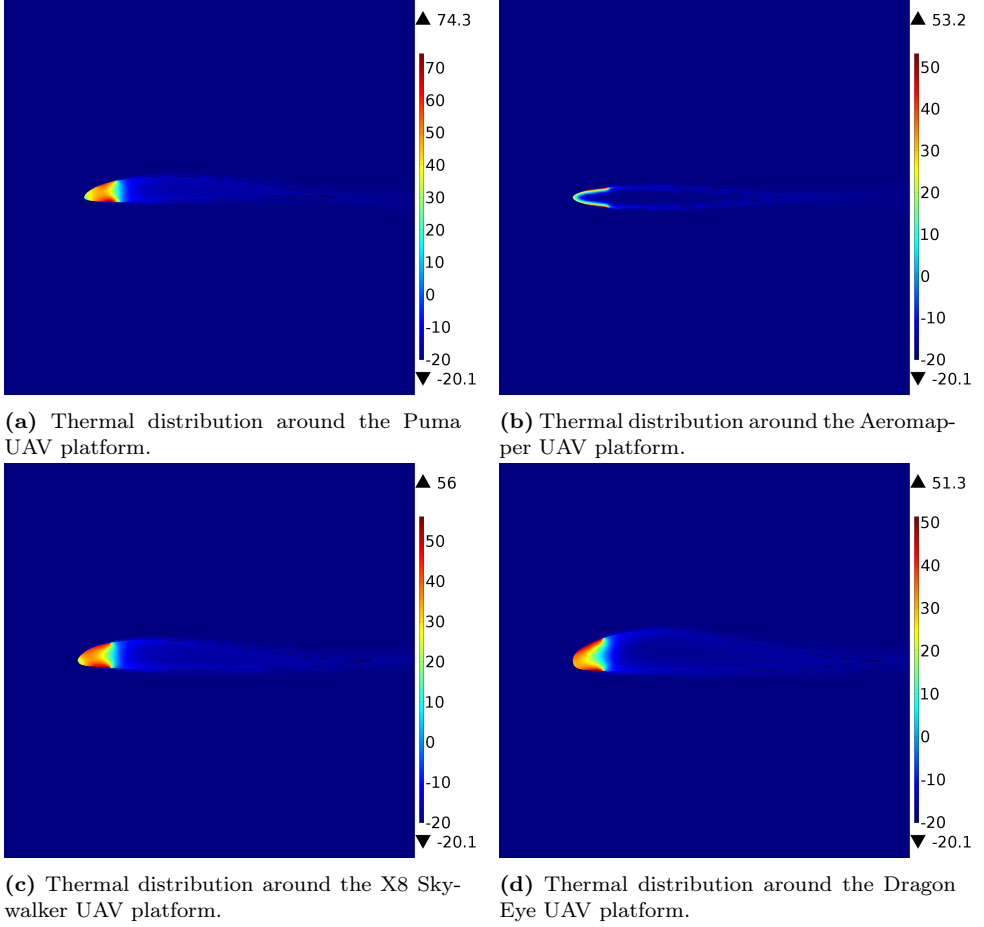
Figure 7.8: Thermal distribution around the each of the four UAV platforms. Power supplied to the electro-thermal source is $P_{ETS} = 500$ W.

UAV platform responses display an almost outlier behaviour of probe 10.

7.3   Discussion and Summary

This chapter has provided considerations and simulation results concerning the electro-thermal source layout and area size, which are aspects that are essential to optimise and eventually minimise IPS power consumption.

Electro-thermal source layout considerations relating to the IPS for small unmanned aircraft, and their theoretical foundation, have been presented and discussed. Considerations based on a simple thermodynamic system model indicate that there could be an inverse proportionality between the steady state average electro-thermal source temperature and the area size of said source. This leads to the hypothesis that IPS objectives achieved with the present layout, could be com-

73
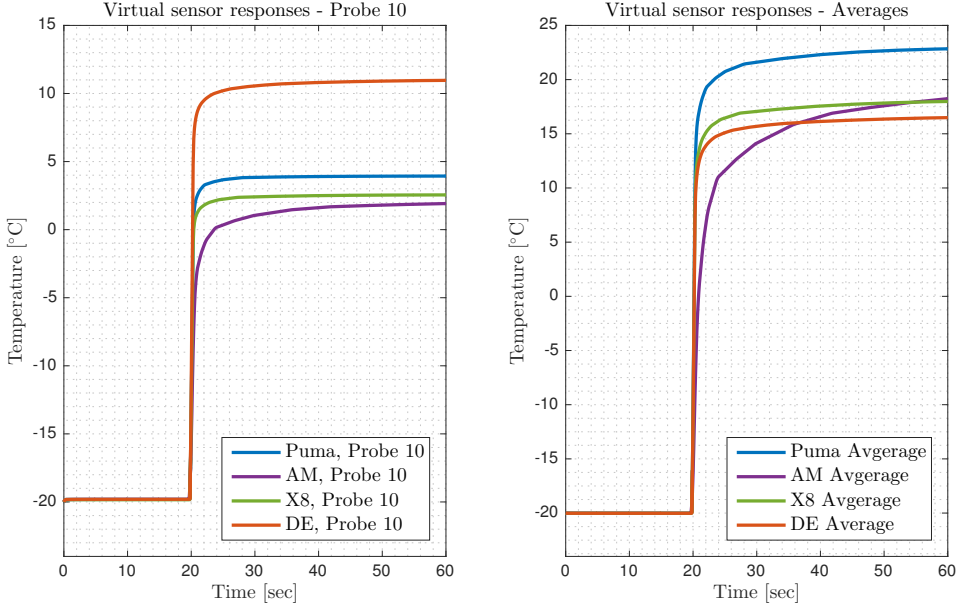
Figure 7.9: Virtual sensor responses (probe 10 and averages) from electro-thermal sources applied to each of the four testbed UAV platforms. Layout is identical and power supplied is $P_{ETS} = 500$ W.

pleted with an alternative layout half the size of the present one, while applying half the power.

Simulations have been conducted to investigate this hypothesis. The initial results indicate the importance of the layout as the average temperatures of the present layout (with an area size of $A_p = 0.1155$ m^2) barely reaches 2°C and the leading edge temperature response (obtained by probe 10) settles at approximately -10°C. This stands in sharp contrast to the alternative electro-thermal source layout (with an area size of $A_a = 0.0566$ m^2), where the average temperature settles at approximately 18°C and the leading edge temperature exceeds the important freezing temperature and and settles at approximately 2.5°C. The power supplied to the electro-thermal source, in both scenarios was $P_{ETS} = 500$ W.

To further highlight the significance of the electro-thermal source area size, a second set of simulations were conducted, where the alternative layout was supplied with $P_{ETS} = 250$ W, as opposed to the present layout' supply of $P_{ETS} = 500$ W. The temperature responses verify the theoretical founded considerations presented in Section 7.1.2, as the responses reveal an almost identical temperature distribution comparing the two layouts.

Other electro-thermal source design options that could have an impact on power consumption includes changing the electro-thermal source layer thickness and having multiple sources on one aerofoil.

A second set of numerical analyses have been conducted with the objective of investigating the thermal distribution over the electro-thermal source applied
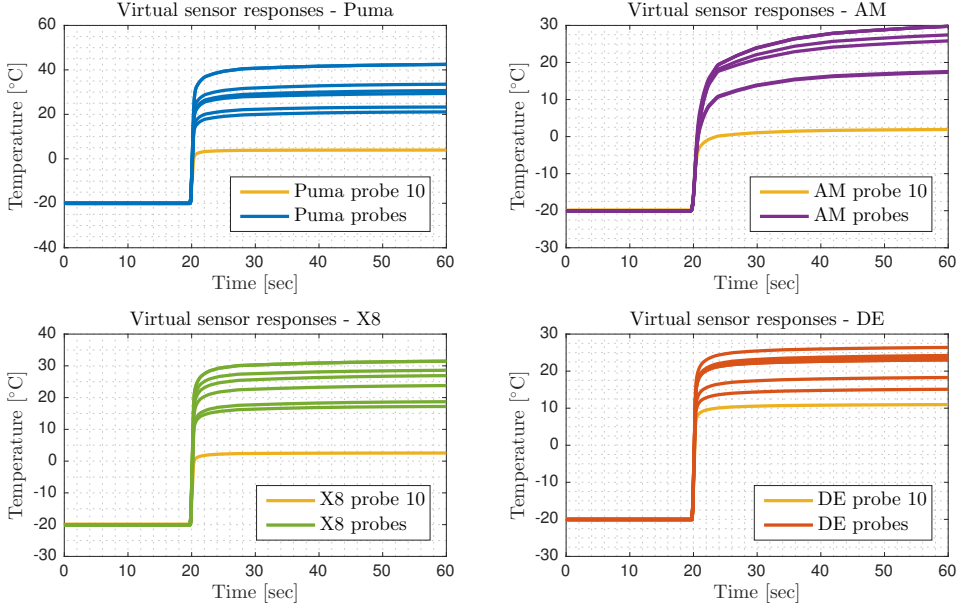
Figure 7.10: Virtual sensor responses from electro-thermal sources applied to each of the four testbed UAV platforms. Layout is identical for all and power supplied is $P_{ETS} = 500$ W.

to the leading edge of each of the four testbed UAV platforms. The area size of the electro-thermal source is approximately identical for each platform, and power supplied was $P_{ETS} = 500$ W. Simulations were conducted for 60 seconds. The thermal distributions displayed in figures 7.8(a) - 7.8(d) clearly show that the core structure is significant with regards to thermal conduction, as the Balsa wood - i.e. the core structural component of the Aeromapper UAV platform - display far superior thermal insulation characteristics than the Polyolefine and Polystyrene of the other testbed UAV platforms.

Figure 7.9 displays the responses of probe 10 located at the leading edge of each aerofoil, and temperatures averaged over all the probes virtually embedded in the electro-thermal sources of each UAV platform. Based on the figure a hypothesis could be stated; generally aerofoils with a sharper leading edge (like the Aeromapper, Puma, and to an extent the X8 Skywalker) will have a less uniform thermal distribution over the electro-thermal source, while aerofoils with a more rounded leading edge (like the Dragon Eye) will have a more uniform thermal distribution. This hypothesis is corroborated by the temperature responses displayed in Figure 7.10.

Chapter 8

Integration Procedures

The process of integrating (retro-fitting) the IPS is, at least to a degree, specific to each platform UAV. This chapter begins with a presentation of the integration procedures that are required to accommodate the structural design of each specific UAV platform, while ensuring that the IPS can perform as needed. This is followed by an introduction to various test sites used for preliminary test flights and the chapter is concluded with a summary.

Note that all integration procedures have been developed and performed by the author himself. It should also be noted that all integration procedures that have been performed up until now, have been for a standalone version of the IPS, i.e. there is no energy dependence from the IPS on the energy source of the aircraft engine(s).

The IPS includes several elements that require integration into the fuselage and wing structures. Previous to applying the electro-thermal source onto the surface of the leading edge of each wing, several temperature sensors (thermocouples) are embedded in the wings. The location of the control unit in the fuselage, necessitate the routing of temperature sensors wires and power cables to the electro-thermal source for each wing. The location of thermocouples and the layout of the electro-thermal source varies with each platform, as one objective of the integration procedure is minimising the intrusive nature of said procedure. Note that the electro-thermal source area typically covers an area above and below the leading edge of the wing. The following presents the individual procedures completed for each of the four UAV platform test beds. Figures 2.5 – 2.8 (presented in Section 2.4) display the four platforms.

The system integration procedure can be divided into several steps, as presented in the following.

- The first step in the integration procedure is embedding the thermocouples in the wings. The location of the thermocouples is chosen as a compromise between, a location at the very leading edge of the wing and minimising the structurally invasiveness of the procedure. The thermocouples generate small amplitude-varying, analogue signals that are amplified and digitalised, through the use of a specific designated chip, before being routed to the control unit.

- The second step is to apply the area chosen for the electro-thermal source with an electrically insulating layer, isolating the electro-thermal source from the surface of the wing.

- The third step is fitting two copper strips to the surface of the wing (one on each side of each wing), enabling for a bus-bar functionality. These are connected to power cables that, in turn, are connected to the control unit and a power source.

- The fourth step is applying the electro-thermal source. The internal resistance of the electro-thermal source is based on the area layout and the thickness of the applied layer. The typical internal resistance ($R_{i,ETS}$) of the electro-thermal source as applied to the platforms presented in this monograph are $R_{i,ETS} \in [0.50, 2.00]\ \Omega$. The electro-thermal source is applied through a liquid carrier (a paint) using a standard hand-held air-driven paint gun. It comprises black carbon and a bonding system in the form of Polyurethane.

- The fifth step is applying another electrically insulating layer, ensuring electrical isolation from the aircraft surroundings and completing the isolation of the electro-thermal source altogether.

The presented steps does not include mounting of the atmospheric sensor, as this procedure is less invasive and can be completed at any procedural stage.

Electrically insulating the embedded temperature sensors from the electro-thermal source is necessary, as the high levels of current running through an activated electro-thermal source will disrupt sensor measurements. Further, due to the size of the temperature sensor, the sensor bead is partly embedded in the electro-thermal source and the wing as illustrated in Figure 8.1.
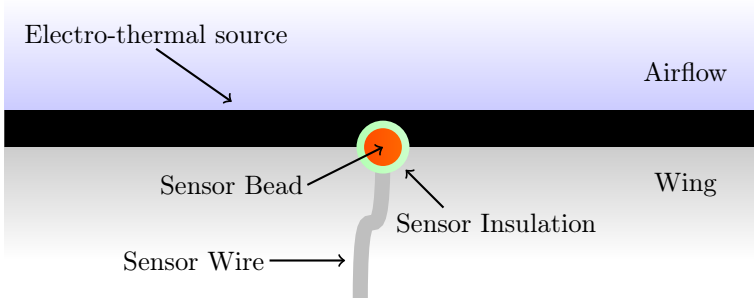
Figure 8.1: Temperature sensor embedded in wing and electro-thermal source.

8.1 Dragon Eye - Integration Procedure

In collaboration with NASA-Ames Research Center one of NASAs Dragon Eye UAV platforms was equipped with a copy of the first prototype of the IPS. The integration was completed in late March 2015.

The Dragon Eye UAV platform was developed for the United States Marines, for use as a hand launched reconnaissance tool. One objective of the design is that
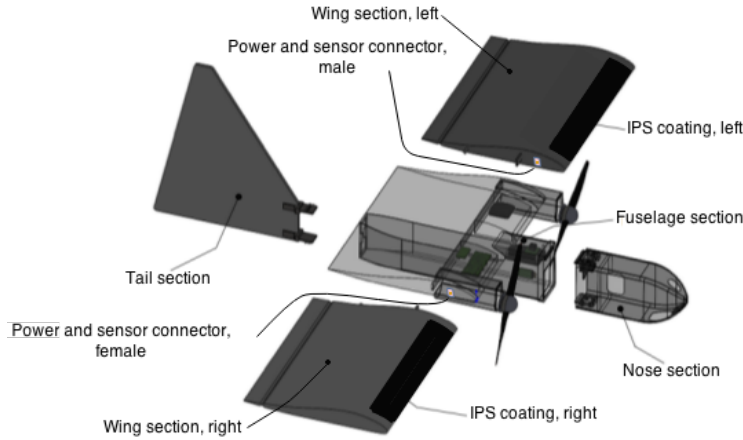
Figure 8.2: Diagram of Dragon Eye UAV platform, including detachable components and IPS integration.

the wings, nose - this is also the payload bay - and tail are detachable, enabling the entire platform to be carried in a backpack. For purposes of energy absorption the same components detach during landings. As the icing protection system - developed and presented in this monograph - relies on measurements from sensors embedded in the wing, and power to the active component (i.e. the electro-thermal source) requires cables, the design of the Dragon Eye UAV platform poses integration challenges. The Dragon Eye operates at a cruise airspeed of approximately 18 m/s and has an endurance of 60 minutes, with a range of up to 5 km. The Dragon Eye has a wing span of 1143 mm and has a maximum take-off weight of approximately 4 kg, including a maximum payload weight of 1 kg.

The core structure of the Dragon Eye is composed of Expanded Polystyrene (EPS) covered by a thin surface layer of Kevlar.

Figure 8.2 is a diagram displaying the detachable components, the electro-thermal source, and thermocouple wires and power cables on the Dragon Eye UAV platform. Figures 8.3(a) and 8.3(b) show how the thermocouple wires and power cables are connected to the fuselage. Finally Figure 8.4 is an image of the complete Dragon Eye UAV platform, with the integrated icing protection system. The small black patch seen on the wing in Figure 8.3(a) (and seen to an extent in Figure 8.3(b)) is a small electrical insulating paste, with high thermal conductivity characteristics.

As previously mentioned, the nose section of the Dragon Eye UAV platform (see Figure 8.2) also serve as the payload bay. However, the prevailing integration procedure for the first IPS prototype onto the Dragon Eye, includes a fixation of the nose section to the main fuselage, thereby denying any detachment of this component during landing.

The challenge of connecting thermocouple wires and electro-thermal source power cables from the fuselage of the Dragon Eye to its detachable wings is resolved by embedding specific connectors in the wings, attached to the Kevlar surface. This
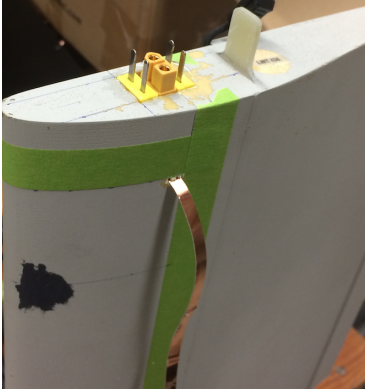
(a) Copper strips, thermocouples with connectors and electro-thermal source power connection to the fuselage.
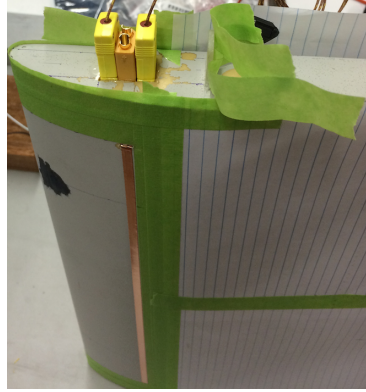
(b) Copper strips, thermocouples and electro-thermal source power connected to the fuselage.

Figure 8.3: Wing element of Dragon Eye UAV platform showing the IPS integration procedure.

Figure 8.4: Integrated IPS onto Dragon Eye UAV platform.

allows for any stress of detachment to be transferred to the wing structure instead of wire and cable connections (see Figures 8.3(a) and 8.3(b)).

The assembled Dragon Eye, with the retro-fitted IPS, displayed in Figure 8.4 includes a custom component mounted on top of the main fuselage. This component includes two GoPro cameras pointing towards each wing. The component is mounted at a location that does not alter the centre of gravity of the aircraft.

The total weight for the electro-thermal sources, with power cables; temperature
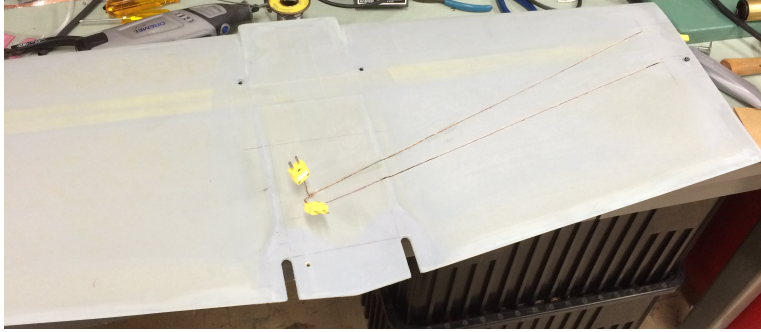
Figure 8.5: Centre wing of a Puma UAV platform, with thermocouple wires embedded.

sensors embedded in the wings, with wires; Atmospheric sensor, with wires; and control unit is approximately 320 g. The power source (a LIPO battery) weighs approximately 400 g, supplying up to 150 W to the electro-thermal source. The GoPro component, including the two cameras, weighs approximately 200 g.

8.2 Puma - Integration Procedure

In collaboration with the National Oceanic and Atmospheric Administration (NOAA) and AeroVironment a Puma UAV platform was equipped with a copy of the first prototype of the IPS. The integration was completed in late March 2015.

The Puma UAV is designed for land based and maritime operations, capable of landing in water or on land. The Puma is slightly larger than the Dragon Eye, but there are many similarities. The core structural composition and surface layer are identical to that of the Dragon Eye. The payload bay is in the main fuselage and only the wings are designed to detach. The design of the aircraft differs from that of the Dragon Eye in the manor with which the wings are attached the fuselage, as the Puma has two outer wings and one centre wing mounted on top of the fuselage. This one big wing composed of three elements is designed to detach from the fuselage during landings. This platform performs at airspeeds ranging from 10 m/s to 23 m/s, with an endurance of approximately 3 hours and maximum range of 15 km. The maximum take-off weight is approximately 6.3 kg. The wingspan of the PUMA UAV platform is 2800 mm.

To apply a similar integration procedure, as was used for the Dragon Eye UAV platform, the centre wing was treated as part of the main fuselage and the electro-thermal source was therefore only applied to the two outer wing elements.

Figure 8.5 display the centre wing of the Puma UAV platform, during integration procedures and Figure 8.6 shows the fully assembled Puma UAV platform, retro-fitted with the IPS.

To retro-fit the outer wing elements with both thermocouples and the electro-thermal source, trenches were needed in the centre wing for thermocouple wires and electro-thermal source power cables. To allow for centre wing detachment during

Figure 8.6: Assembled Puma, with IPS retro-fitted.

landings, intermediate connectors were used for the wires and cables, connected to the fuselage and the outer wings (see Figure 8.5).

The Puma UAV platform, fully assembled and retro-fitted with the IPS, is displayed in Figure 8.6, where it should be noted that only one of the outer wings have an applied electro-thermal source. After assembly the Puma was to be used for multiple scientific purposes on operations in the Arctic and Antarctic regions, and as such the available space for the control unit was limited, which impacted the retro-fit options. Consequently only one outer wing was fitted with the electro-thermal source. For a closer look at the image displayed in Figure 8.6 the control unit and atmospheric sensor are visible underneath the starboard side of the centre wing.

The total weight for the electro-thermal source, including power cables; temperature sensors embedded in the wing, with wires; Atmospheric sensor, with wires; and control unit is approximately 300 g. The power source (a LIPO battery) weighs approximately 400 g, supplying up to 200 W to the electro-thermal source.

8.3 X8 Skywalker - Integration Procedure

One of the central UAV platforms of the NTNU unmanned aircraft laboratory in Trondheim, Norway, is the X8 Skywalker. Throughout the developmental stages of the IPS, this platform has served as the primary testbed. The integration procedure of the first prototype IPS onto the X8 Skywalker UAV platform was completed in early March 2015.

The X8 Skywalker is composed out of Expanded Polyolefine alone making it extremely light, yet highly durable. The aircraft can be launched by hand, but the preferred choice of the NTNU-UAV lab. pilots is catapult launches. For transportation purposes the wings are detachable, but for flight and landing nothing detaches, setting this platform aside from the two other UAV platforms presented previously in this chapter. The X8 Skywalker has an operational range of approximately 40 km at a cruise airspeed of 18 m/s, depending on flight conditions. The UAV has a wingspan of 2120 mm, a maximum payload weight of 1 kg, and maximum take-off weight of 4.5 kg.

Figure 8.7 shows the wing of an X8 Skywalker fitted with the electro-thermal source and embedded thermocouples. Figure 8.8 display the X8 Skywalker fully assembled, with the IPS integrated, about to be launched from a catapult, out over Kongsfjorden at Ny-Ålesund, Svalbard, Norway.

The power source, supplying the electro-thermal source with power, is located in the payload bay alongside the control unit. The atmospheric sensor is located on the fuselage at the nose of the aircraft, close to the pitot-tube that supplies the on board flight computer with airspeed measurements.

Figure 8.7: X8 Skywalker wing, with thermocouples embedded and applied electro-thermal source. Thermocouple locations are highlighted by a red circle (◯) and the electro-thermal source is emphasized by a red square (▢).

The location of the electro-thermal source temperature sensors (there are two) - highlighted in Figure 8.7 by a red circle - was chosen based on the objective of minimising the structurally invasive process of embedding the sensors in the wing.

From the outside of the aircraft it is close to impossible to see the icing protection system once integrated. An attempt to display this is seen in Figure 8.8, which shows the fully assembled X8 Skywalker platform, retro-fitted with the IPS, about to be launched over Kongsfjorden, Ny-Ålesund, Svalbard, Norway.

The accumulated weight for the electro-thermal source, including power cables; thermocouples embedded in the wings, with wires; Atmospheric sensor, with wires; and control unit is approximately 380 g. The power source (two parallel LIPO batteries) weighing approximately 500 g, supplying up to 400 W to the electro-thermal source.

8.4 Aeromapper - Integration Procedure

The latest addition to the UAV platform test bed portfolio, is the Aeromapper, operated by the University of Alaska, Fairbanks (UAF). The Aeromapper was only introduced as a test bed for the IPS in late 2015, with the first retro-fitting completed in mid-March 2016 at the UAV laboratory facilities of UAF.

The Aeromapper platform has several structural and design distinctive features. The structural core of the wings are a mix of Balsa wood and air covered by a surface layer of carbon fibre. The Aeromapper is hand-launched platform with a single-rotor engine located in the front of the aircraft. Safe landing is completed by the deployment of a parachute. The Aeromapper has very thin wings, maximum thickness is approximately 15 mm, which complicates integration somewhat. The

Figure 8.8: Fully assembled X8 Skywalker, with integrated IPS, about to be launched on a preliminary flight test out over Kongsfjorden, Ny-Ålesund, Svalbard, Norway.

maximum airspeed for the Aeromapper is approximately 25 m/s and cruise airspeed is 15 m/s, with an endurance of 90-100 minutes, and a ground telemetry range of approximately 20 km. The payload bay module used for the work presented here allows for approximately 0.65 kg of payload with a maximum take-off weight for the combined aircraft of 5.35 kg. The wingspan of the Aeromapper is 2000 mm.

Figures 8.9(a) – 8.9(c) display an Aeromapper wing element subjected to the process of retro-fitting the IPS electro-thermal source and temperature sensors.

As described previously in this chapter the location of the electro-thermal source temperature sensors - embedded in the wing - is a result of the integration objective to minimise the intrusive process of retro-fitting the aircraft with the IPS. The current location (see Figure 8.9(a)) enables for thermocouple wire threading in one of the cavities of the wing, there for the purpose of control surface actuator wiring as illustrated in Figure 8.9(b). The profile characteristics of the Aeromapper wing entail surface mounted power cable connections, as opposed to the typical (typical for the Dragon Eye, Puma, and X8 Skywalker platforms) subsurface connections. The difference can be seen when comparing Figures 8.3(b) and 8.9(c), where the copper strips of the latter clearly never enter the wing structure, as opposed to what is seen in the prior.

The accumulated weight for the electro-thermal source, including power cables; thermocouples embedded in the wings, with wires; Atmospheric sensor, with wires; and control unit is approximately 320 g. The power source (a LIPO battery) weighing approximately 300 g, supplying up to 250 W to the electro-thermal source.

8.5   Summary

The integration procedures presented have all been conducted in concordance with the objectives of the IPS, i.e. minimizing structural invasiveness and infer little to no aerodynamic impact once integrated.

(a) Wing element fitted with copper strips and thermocouples, their location highlighted by the red circle (◯).
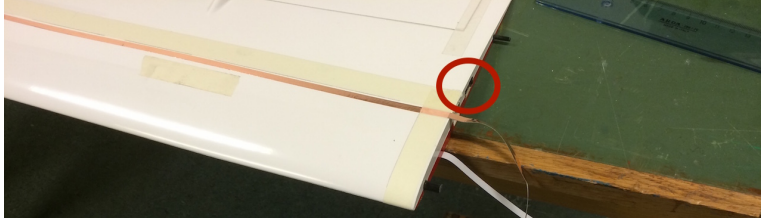
(b) Wing element with wing structure exploited for thermocouple wiring, emphasized by the red circle (◯).
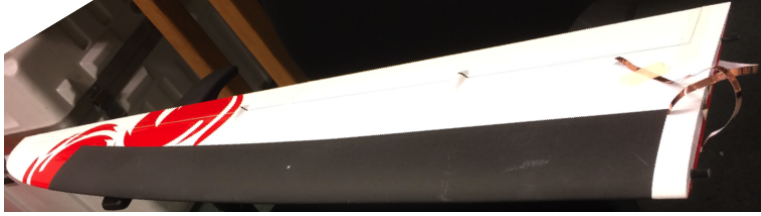
(c) Wing element with electro-thermal source applied to the leading edge.

Figure 8.9: Aeromapper wing element during various integration stages.

The process of integrating the IPS is specific to each platform UAV. This chapter has provided a presentation of the integration procedures that have been required to accommodate the structural design of each specific platform, while ensuring that the IPS performs as needed.

The IPS includes several elements that require integration into the fuselage and wing structures. Previous to applying the electro-thermal source onto the surface of the leading edge of each wing, several temperature sensors are embedded in the wings. The location of the control unit in the fuselage, necessitate temperature sensors wires and power cables being routed to the electro-thermal source for each wing. The location of thermocouples and the layout of the electro-thermal source varies with each platform.

Procedures have been developed and the IPS have been integrated onto the four primary testbeds, enabling icing protection while abiding by airworthiness restrictions and requirements, i.e. compliance with aircraft type design and ensuring that the aircraft is in a condition for safe operation.

Chapter 9

Wind Icing Tunnel Experiments

This chapter presents findings from wind icing tunnel (controlled environment) experiments conducted on the wing elements of some of the UAV platform testbeds retro-fitted with the developed IPS. The test site facilitating the controlled environment is the LeClerc Icing Research Laboratory (see [99]), developed and operated by Cox & Company inc., located at 1664 Old Country Road, Plainview, NY 11803. All experiments presented in this chapter were obtained during a two day period in mid February 2016.

The chapter begins with a description of the test facility used and an introduction to the work preceding the experiments. This is followed by a presentation of the results, before the chapter is concluded with a discussion and a summary.

9.1 LeClerc – Introduction

A variety of experiments were conducted. The majority of these were conducted using the IPS presented previously, excluding online icing detection algorithms. However, for a specific type of experiments only a subset of the control system features and capabilities were applied. All experiments presented here were conducted in Test Section 1 (TS1) at the LeClerc Icing Research Laboratory (see Figure 9.1 for an illustration of the facility). A cross section of TS1 is seen in Figure 9.2 and a floor diagram is found in Figure 9.3. Note that all measurements in Figures 9.1–9.3 are in unit inches (").

The platform wings used in the experiments presented here, all includes an applied electro-thermal source and temperature sensors supplying the control unit with measurements of the electro-thermal source temperature (T_{ETS}). The control unit was located outside the wind icing tunnel during every experiment. The aircraft platforms used in the wind icing tunnel experiments were the X8 Skywalker and the PUMA.

9.1.1 Adapter

Due to the cross sectional size of TS1 each of the platform wings was mounted vertically, attached to the floor. To reduce the time used mounting platform wings
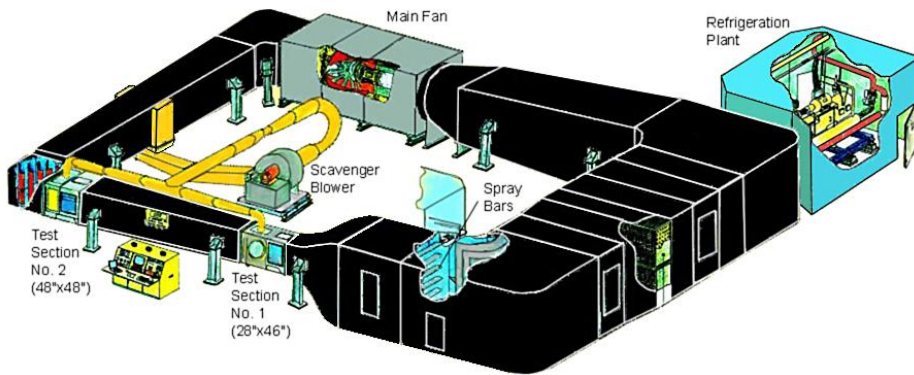
Figure 9.1: LeClerc Icing Research Laboratory - icing wind tunnel, courtesy of Cox & Company Inc.
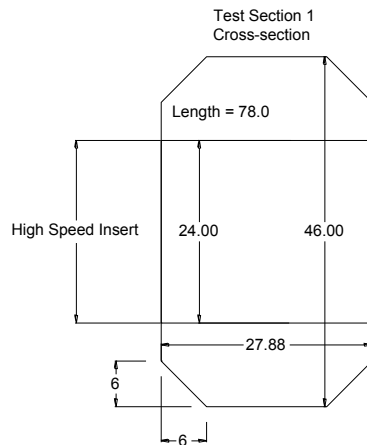
Figure 9.2: TS1, cross sectional view, courtesy of Cox & Company Inc.

in TS1 a wing-to-floor adapter was developed and applied (see Figures 9.4(a) and 9.4(b)). This adapter mimics the fuselage of each platform tested, while also being compatible with the mounting holes in the TS1 floor.

The adapter, illustrated in Figures 9.4(a) and 9.4(b), is a two-part construction made up entirely of aluminium. The adapter has a floor structure and a mounting structure. The floor structure is based on a floor plate measuring approximately $14 \times 12 \times 0.2$ (l,w,h) inches ("). Eleven holes have been drilled into the floor plate; ten mounting holes ($\varnothing 1/4$") and one hole ($\varnothing 2$") for wires and cables. These holes coincided with the holes found in the floor diagram of TS1. The floor structure also includes a "house", or casing, designed to have a small impact on airflow. The purpose of the casing is to secure and isolate wires running from the wings to the controller, but also to ensure a stable and strong structure that should withstand
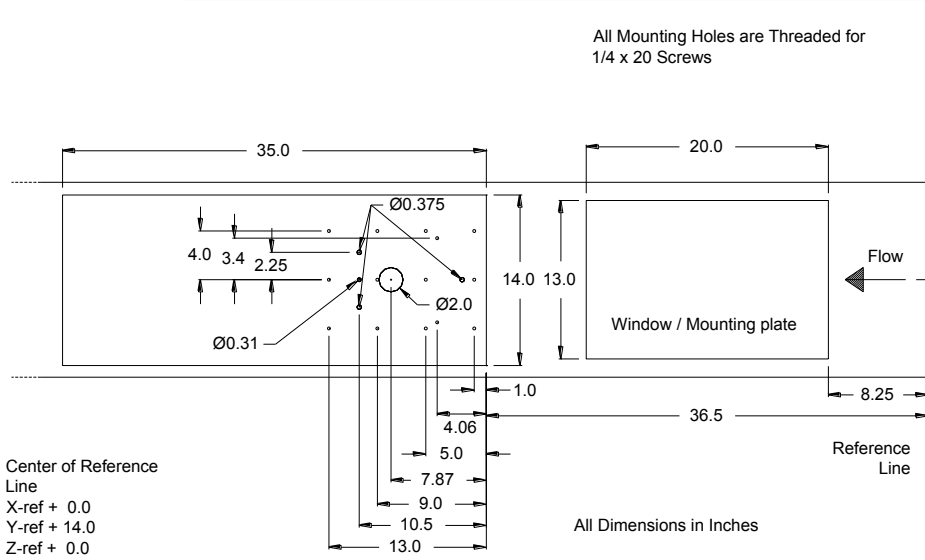
Figure 9.3: TS1, floor diagram, courtesy of Cox & Company Inc.

the forces imposed upon each of the platform wings. The second part of the adapter is the mounting structure (henceforth denoted the virtual fuselage (VF)), which serves as a unit that mimics the aircraft fuselage of each platform. The VF is a box designed to fit perfectly into the floor casing. Further, holes and trenches were drilled for each platform wing ensuring a strong and compatible VF. For an illustration of the adapter with a Dragon Eye wing mounted see Figures 9.4(c) and 9.4(d), while Figures 9.5(a) and 9.5(b) display the wing of and X8 Skywalker mounted through the adapter in the wind tunnel of the LeClerc Icing Research Laboratory (LIRL).

9.1.2 Controlled Atmospheric Conditions

The atmospheric conditions that have the largest potential impact on aircraft performance can be quantified by three parameters, ambient temperature T_∞, liquid water content (LWC) in the surrounding air, and median volume diameter (MVD) of liquid water droplets in the surrounding air stream. Henceforth, in this chapter, these parameters will be denoted the LIRL parameters. For the test scenarios presented here an approach similar to the use of a test matrix (see [13]) was adopted, with parameter values influenced by [13, 33, 100], which also abide by the restrictions of the wind icing tunnel facility. The relevant values of the LIRL parameters are $T_\infty = \{-5, -10, -15\}$ °C, LWC= $\{1.20, 1.60, 2.00, 2.50\}$ g/m^3, and MVD= $\{0, 20, 50\}$ μm. The airspeed for all experiments is limited to $V_\infty \in [15, 20]$ m/s. Icing conditions are introduced into the tunnel area by activating the "cloud", which is produced through nozzles that ensure conditions with specified parameter values. Figures 9.6(a) – 9.6(f) display the effects of icing on an X8 Skywalker platform wing element, with LIRL parameters $T_\infty = -15$ °C, LWC= 2.50 g/m^3,

(a) Two part adapter (birds-eye-view).

(b) Two part adapter (front view).

(c) Adapter with DE wing (birds-eye-view).

(d) Adapter with a DE wing mounted (front view).
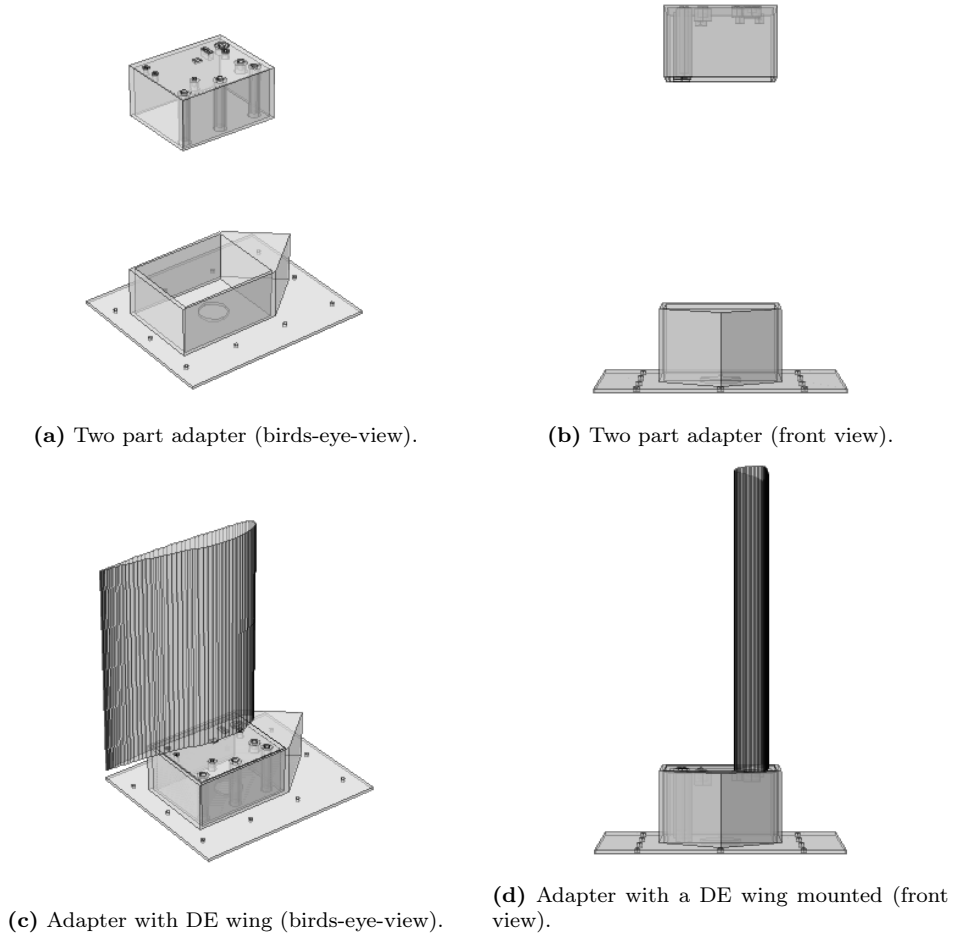
Figure 9.4: Two-part adapter for icing tunnel floor mounting.

MVD= 50 μm, and airspeed $V_\infty \approx 20$ m/s. The wing element was subjected to the specified conditions for a duration of 20 minutes, with initial test time $t_0 = 0$ seconds.

It should be noted that the wind icing tunnel facility was designed with the intent to investigate icing occurrences on elements of larger aircraft, generally travelling at much higher airspeeds then that of the UAV platforms applied for the work presented in this monograph. Hence the inner workings of the wind icing tunnel functionality imposes limitations (particularly lower boundaries) upon the initial desired LIRL parameters resulting in the alternative test matrix presented in the previous paragraph. The icing conditions these parameters entail range from severe to extremely severe for any type and size aircraft [4, 9–12, 15, 100–102].

Figures 9.6(a) – 9.6(f) have been introduced here for illustrious purposes alone and are used to clarify how and where icing forms under the given circumstances,

(a) Lower side of a wing element of the X8 Skywalker platform.
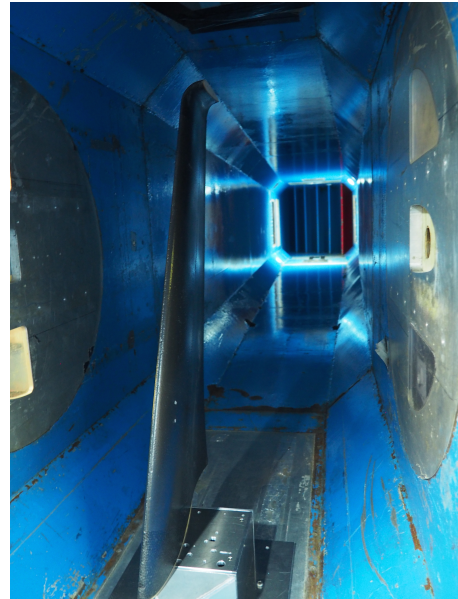
(b) High side of a wing element of the X8 Skywalker platform.

Figure 9.5: X8 Skywalker platform wing element, mounted through the adapter in the wind tunnel of the LeClerc Icing Research Laboratory.

with LIRL parameters $T_\infty = -15°$C, LWC= 2.50 g/m^3, and MVD= 50 μm. The cloud was activated at $t = 5$ seconds, immediately thereafter the leading edge of the wing element display signs of icing, noticeable by the matte expression of the wing element surface. At $t = 60$ seconds a layer of ice has formed on the leading edge of the wing element of approximately 1 mm. As no ice protection solution is active the icing becomes more distinct and at $t = 20$ minutes the ice layer, comprised of mixed icing, is approximately 3 cm thick at certain locations, with a rough rime icing surface.

9.2 Results

The experimental results obtained at the LeClerc Icing Research Laboratory are divided into three categories, here presented in individual subsections. The first revolves around the results appertaining the *icing detection*, the second presents the results obtained regarding *anti-icing*, and finally the closing subsection presents the experimental results concerning *de-icing*.

9.2.1 Icing Detection

As described previously the data obtained in the icing detection category are used to validate the electro-thermal-based icing detection algorithm. Two datasets are

(a) X8 Skywalker wing element in icing conditions ($t = 0$ seconds).

(b) X8 Skywalker wing element in icing conditions ($t = 30$ seconds).

(c) X8 Skywalker wing element in icing conditions ($t = 60$ seconds).

(d) X8 Skywalker wing element in icing conditions ($t = 5$ minutes).

(e) X8 Skywalker wing element in icing conditions ($t = 10$ minutes).

(f) X8 Skywalker wing element in icing conditions ($t = 20$ minutes).
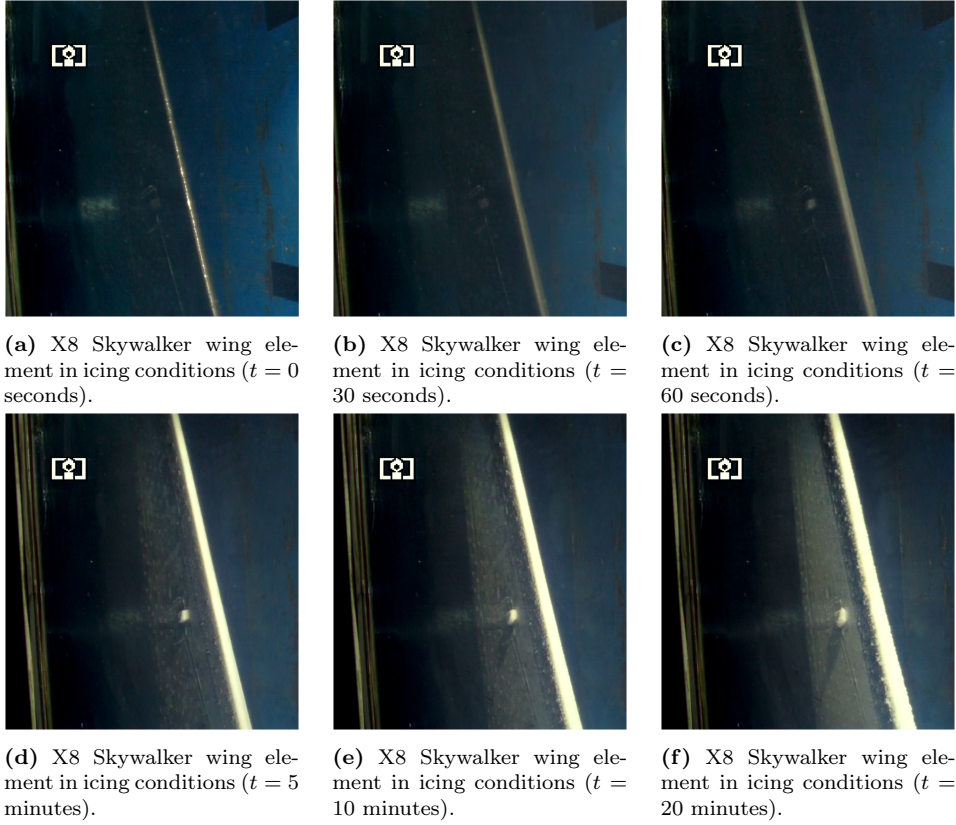
Figure 9.6: X8 Skywalker platform wing element subjected to icing conditions.

required, one where the atmospheric conditions do not sustain icing, and one where icing is present. The temperature profiles necessary are induced by a momentary (duration of 10 seconds) and periodical (separated by 50 seconds) activation of the electro-thermal source. Data from the icing detection category experiments have been obtained with LIRL parameters $T_\infty \in [-17.5, -12.5]$ °C, LWC= $\{0, 2.50\}$ g/m^3, and MVD= $\{0, 50\}$ μm, while the airspeed for all experiments is limited to $V_\infty \in [15, 20]$ m/s. Figures 9.7 and 9.8 display the results from the icing detection category experiments obtained for the electro-thermal-based icing detection algorithm. The icing detection category experiments presented here are all conducted on the X8 Skywalker platform.

LIRL parameters and airspeed for the responses displayed in Figure 9.7 are $T_\infty \approx -16$ °C, LWC= 0 g/m^3, MVD= 0 μm, and $V_\infty \approx 17$ m/s. I.e. the responses are obtained in non-icing conditions. Maximum power supplied to the electro-thermal source, in active periods, is $P_{ETS} \approx 92$ W. Test time is 5 minutes with five periods (lasting 10 seconds each), where the electro-thermal source is active five times. Each active period is followed by a 50 second period of inactivity, a 'cool down' period.

Figure 9.7: Icing detection experiment in **non**-icing conditions, where 1) is the airspeed, 2) signify whether the cloud is on or off, 3) is the temperature of the electro-thermal source, and 4) is the applied power. The red (–) vertical line signify the start time of this specific test and the yellow (–) line represents the end time.

The responses displayed in Figure 9.7 are the consequences of the thermodynamic system, introduced in Chapter 2, being brought out of thermal equilibrium. The thermodynamic system enters a transient phase as the electro-thermal source is activated, forcing the temperature of the electro-thermal source to rise. Once the electro-thermal source is deactivated, the thermodynamic system asymptotically enters a state of equilibrium once again. It is the resultant temperature profile of the electro-thermal source that is essential to the electro-thermal-based icing detection algorithm, and it is the data obtained in the non-icing conditioned experiments that serve as a reference.

Figure 9.8 displays responses obtained in icing conditions, with LIRL parameters $T_\infty \approx -16.00$ °C, LWC= 2.00 g/m^3, MVD= 50 μm, and $V_\infty \approx 17$ m/s. Maximum power supplied to the electro-thermal source, in active periods, is $P_{ETS} \approx 92$ W. Test time is 5 minutes. This experiment is identical to the one presented previously and (responses displayed in 9.7), with the exception that the prior experiment is conducted in non-icing conditions.

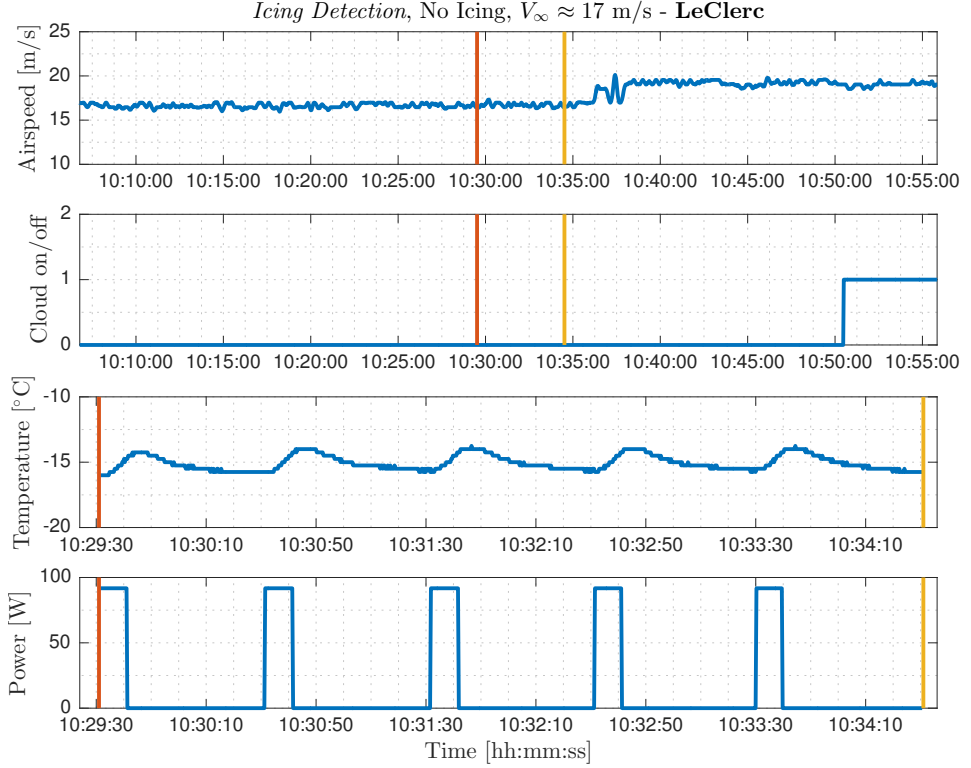Comparing the two experiments it becomes clear that the ice layer on the lead-

Figure 9.8: Icing detection experiment in icing conditions, where 1) is the airspeed, 2) signify whether the cloud is on or off, 3) is the temperature of the electro-thermal source, and 4) is the applied power. The red (–) vertical line signify the start time of this specific test, and the yellow (–) line represents the end time.

ing edge of the wing element has a considerable impact on the temperature profile of the electro-thermal source. A quantifiable measure of this impact is the electro-thermal source temperature rise and fall times. For the experiment in non-icing conditions the average temperature increase identified, while the electro-thermal source is activated, is 1.75 °C from -15.75 °C to -14.00 °C. The average rise time for this increase is 9 seconds, and the average fall time is 21 seconds. Conversely, the experiment conducted in icing conditions results in a temperature profile that reveals an average temperature increase of 0.75 °C from -15.75 °C to -15.00 °C. The average rise time required to achieve this increase is identified as 6 seconds, while the fall time is 26 seconds. This distinction is also illustrated in Figure 9.9, where the temperature profiles from each experiment is displayed in a comparable manner.

Note that rise times presented in the above paragraph are defined as *the required time for the response to rise from x% to y% of its final value* [103], where $x = 0$ % and $y = 100$ % in the presented results. The same definition applies for fall times. Typically these percentiles are 10% and 90%, however, here the
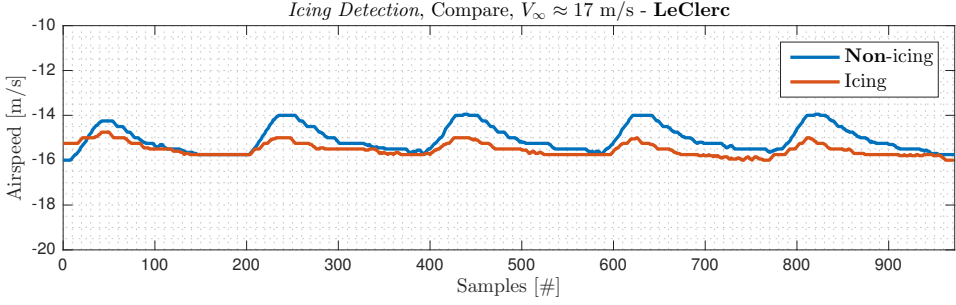
Figure 9.9: Icing detection responses comparison between data obtained in **non**-icing conditions and data obtained in icing conditions.

difference between equilibrium temperature and attained temperature, while the electro-thermal source is active, combined with a temperature sensor resolution of ± 0.25 °C renders that practice moot.

Here it should be noted that the electro-thermal-based icing detection algorithm presented in Chapter 5 has been developed after the experiments presented in this chapter, and that the responses obtained at the LeClerc wind icing research laboratory served as inspiration to that icing detection approach. The electro-thermal-based icing detection algorithm requires an average temperature over the surface area of the electro-thermal source. However the temperature responses obtained during the experiments were for a specific location on the electro-thermal source. Hence, attempts at validating the icing detection algorithm against experimentally obtained data have not been fully concluded.

9.2.2 Anti-Icing

The data obtained in the anti-icing experimental category is used to demonstrate the feasibility of the proposed solution, i.e. that any electro-thermal source temperature required to prevent ice from forming on the leading edge of the aircraft wings, is successfully achieved and maintained for whatever time period required.

The LIRL parameters applied for the anti-icing category experiments are $T_\infty \in [-6.00, 6.00]$ °C, LWC= $\{0, 2.50\}$ g/m^3, and MVD= $\{0, 50\}$ μm, while the airspeed for all experiments is limited to $V_\infty \in [15, 20]$ m/s.

The desired electro-thermal source temperature for the experiments presented here is $T_{set} = 5$ °C. Figures 9.10 and 9.11 display the results from the anti-icing category experiments. These experiments were performed using the PUMA platform.

LIRL parameters and airspeed for the responses displayed in Figure 9.10 are $T_\infty \approx -6$ °C, LWC= 0 g/m^3, MVD= 0 μm, and $V_\infty \approx 17$ m/s. Maximum power used to achieve the set point temperature of $T_{set} = 5$ °C is approximately 260 W and to maintain the set point temperature the power stabilises at approximately 140 W. Test time is 5 minutes.

Figure 9.10 displays the response of the anti-icing experiment conducted in non-icing conditions. Initially, to achieve the desired set temperature, the electro-
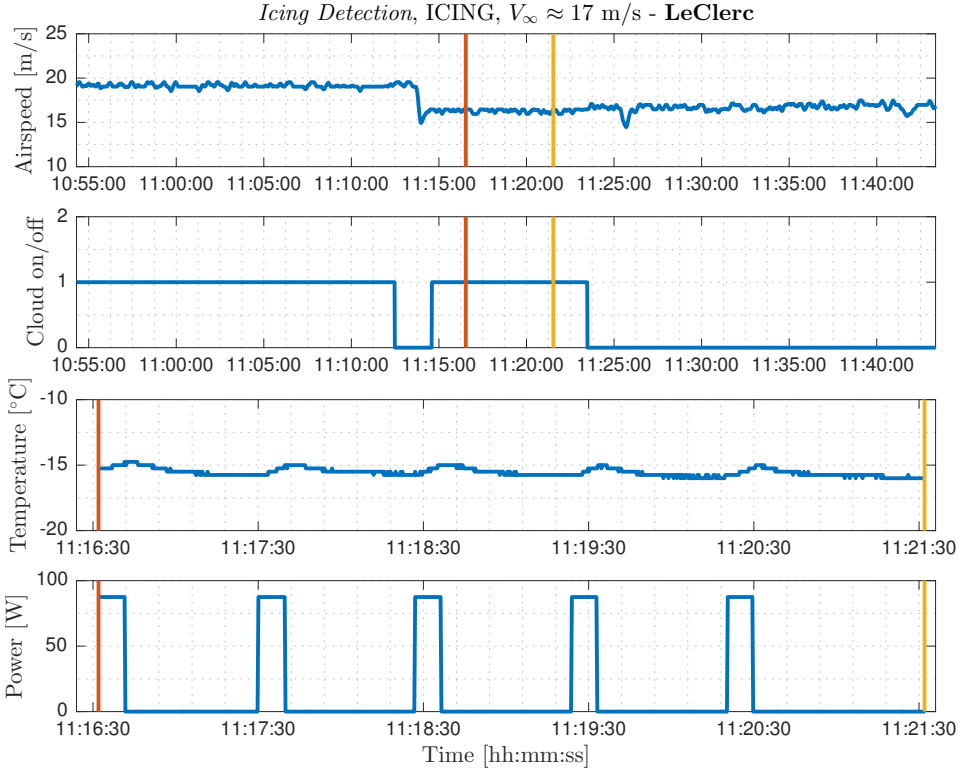
Figure 9.10: Anti-icing experiment in **non**-icing conditions, where 1) is the airspeed, 2) signify whether the cloud is on or off, 3) is the temperature of the electro-thermal source, and 4) is the applied power. The red (–) vertical line signify the start time of this specific test, and the yellow (–) line represents the end time.

thermal source is supplied with the maximum power (approximately 260 W) available for this experiment. Once the desired set temperature is reached the power requirement to maintain said temperature is significantly reduced to approximately 140 W. Once power is no longer supplied to the electro-thermal source its temperature decreases to ambient, here approximately -6 °C.

Prior to activating the cloud, the responses displayed in Figure 9.11 are for non-icing conditions, where LIRL parameters, airspeed, and power profile are close to identical to the anti-icing experiment, conducted in non-icing conditions, presented previously. The primary difference is the power level available, where it was limited to 260 W in the previous experiment, here it is 340 W. This difference is expressed as a faster temperature increase of the electro-thermal source when 340 W is supplied as opposed the temperature increase when 260 W is supplied. For the duration of non-icing conditions the solution performs as expected.

However, once the cloud is activated (icing conditions are introduced) the power required to maintain the desired set temperature of the electro-thermal source, increases drastically to an extent where the available power is not enough to maintain

Figure 9.11: Anti-icing experiment in icing conditions, where 1) is the airspeed, 2) signify whether the cloud is on or off, 3) is the temperature of the electro-thermal source, and 4) is the applied power. The red (–) vertical line signify the start time of this specific test, and the yellow (–) line represents the end time. The dashed light blue (- -) vertical line represent the beginning of icing conditions and the dashed green (- -) vertical line is the end of icing conditions.

the temperature at the desired level. Supplying the maximum available power (340 W) to the electro-thermal source enables for a stable temperature, but at a lower level than the desired set temperature. LIRL parameters and airspeed for the responses displayed in Figure 9.11 are $T_\infty \approx -5$ °C, LWC= 2.5 g/m^3, MVD= 50 μm, and $V_\infty \approx 17$ m/s.

Fascinatingly when icing conditions cease after 14:40:37, the power supplied to the electro-thermal source is not enough to completely shed the ice that has formed, which is the cause for the continued struggle to reach the desired set temperature. It should be noted ice formed at a considerably slower rate once anti-icing was active.

Test time for the anti-icing experiment, in icing conditions, is 16 minutes and 17 seconds.

9.2.3   De-Icing

As for the previously presented anti-icing experiments the data obtained in the de-icing category of experiments is needed for demonstrating the viability of the proposed solution.

The LIRL parameters applied for the experiments presented here are $T_\infty \in [-10.00, 10.00]$ °C, LWC= $\{0, 1.60\}$ g/m^3, and MVD= $\{0, 20\}$ μm, while the airspeed for all experiments is limited to $V_\infty \in [15, 20]$ m/s.

It is important to note that atmospheric conditions, where $T_\infty \approx -10.00$°C, LWC$\approx$ 1.6 g/m^3, and MVD$\approx$ 20 μm indicate severe icing conditions. Unfortunately, due to the limitations of the wind icing tunnel facility, these conditions are some of the least severe icing conditions attainable.

For this category of experiments the objective of the IPS is to mitigate occurrences of icing, i.e. initially allow for a small icing layer to form and then rapidly increase the temperature of the electro-thermal source. This will create a liquid boundary between the electro-thermal source and the ice, which in turn will enable aerodynamic shedding of the accumulated ice layer. In many respects the de-icing program routine is not that different from the icing detection, as both rely on rapid heating of the electro-thermal source, followed by a 'cool-down' period. However, the de-icing program routine applied in the experiments presented here has an electro-thermal source activation period of 60 seconds, as is the subsequent 'cool-down' period. Also it includes elements from the anti-icing program routine, specifically a desired set point temperature. For the de-icing category experiments this set temperature is $T_{set} = 10$ °C, as this has been identified as the minimum surface temperature required to shed ice layers [31]. It is important to stress that shedding the ice layer is a consequence of aerodynamic forces driven primarily by the airspeed, therefore, the desired set temperature could prove insufficient under various circumstances, as the work presented in [31] is focussed on large conventional aircraft wing elements, with airspeeds limited to approximately 78 m/s.

Figure 9.12 displays some of the results from the de-icing category experiments that are conducted in non-icing conditions, and Figures 9.13(a) – 9.13(c) are presented for illustrative purposes and display the effects of icing and the response of the de-icing mitigation. All of the experiments presented in this subsection are performed using the wing element of a PUMA platform.

The responses to the de-icing experiments conducted in non-icing conditions presented here are displayed in Figure 9.12. The LIRL parameters for the experiment are $T_\infty \approx -10.00$ °C, LWC= 0 g/m^3, MVD= 0 μm, and the airspeed is $V_\infty \approx 17$ m/s, with a test time is 8 minutes 16 seconds. Maximum power supplied is $P \approx 350$ W.

The experiment is initiated by an activation of the electro-thermal source, which in an effort to reach the set temperature of $T_{set} = 10$ °C requires maximum available power ($P \approx 350$ W). After 60 seconds of activation the temperature of the electro-thermal source reaches $T_{ETS} = 9.25$ °C, i.e. the objective to reach the set temperature is not achieved. During the 'cool down' period the temperature of the electro-thermal source stabilises at approximately ambient temperature. The pattern repeats for the duration of the experiment.

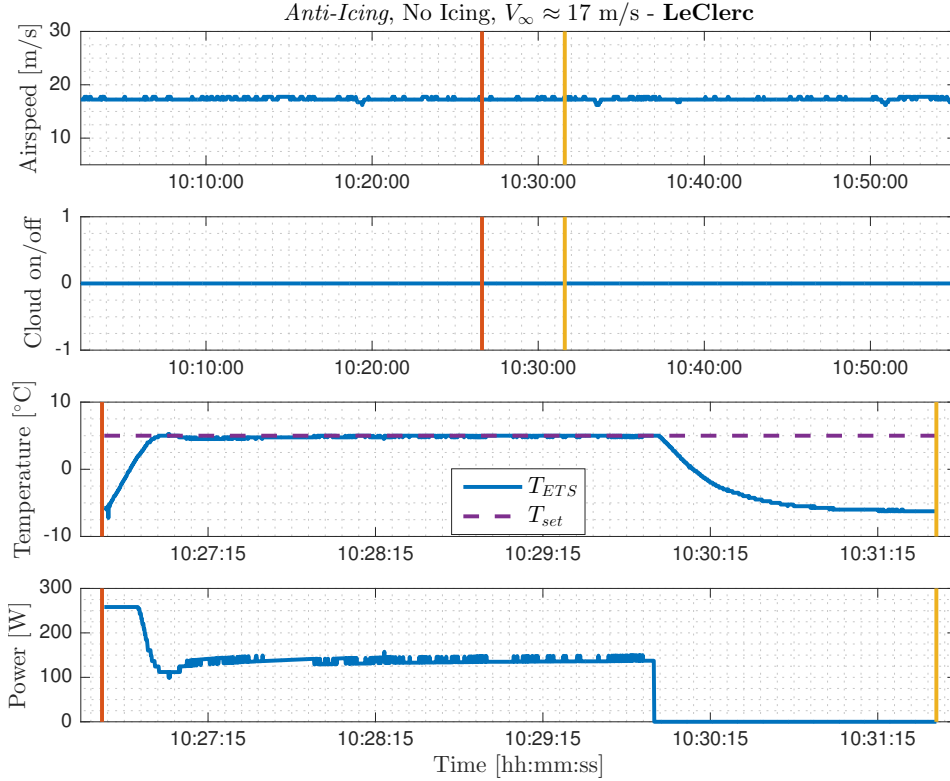The de-icing experiments conducted in non-icing conditions reveals that more
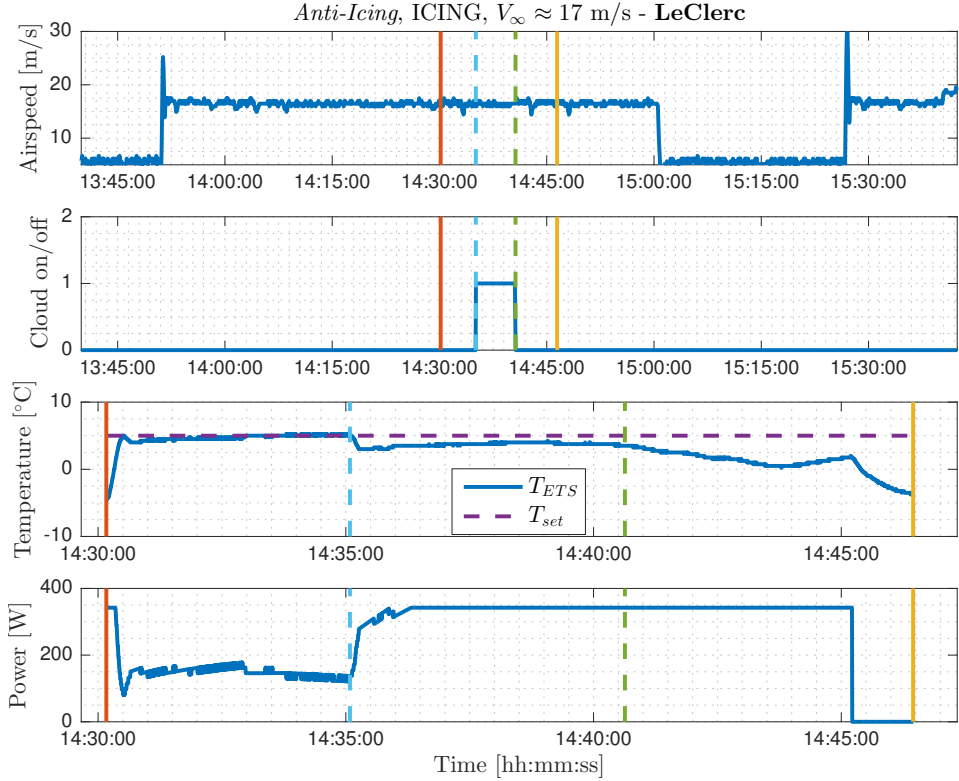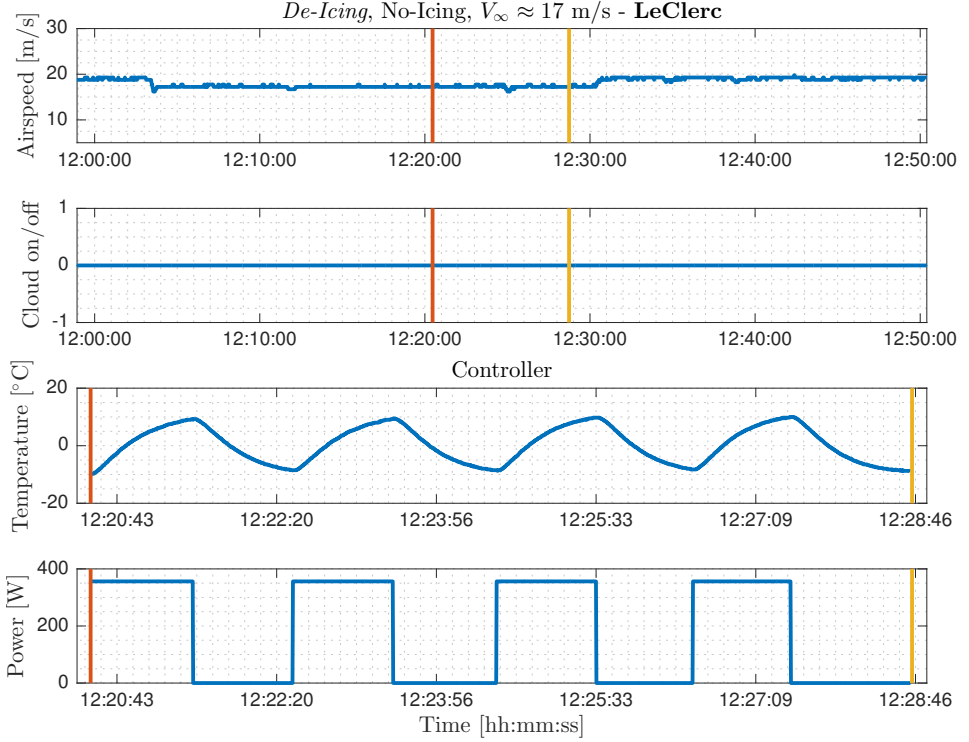
Figure 9.12: De-icing experiment in **non**-icing conditions, where 1) is the airspeed, 2) signify whether the cloud is on or off, 3) is the temperature of the electro-thermal source, and 4) is the applied power. The red (–) vertical line signify the start time of this specific test, and the yellow (–) line represents the end time.

power is required to fulfil the primary objective of rapidly achieving the desired set point temperature. The IPS was not developed to consistently perform at the power levels required. However, one experiment was conducted, not so much to investigate the overall performance of the program routine, but more it was an investigation into the power required to shed ice on the leading edge of the wing element. Images from the experiment is displayed in Figures 9.13(a) – 9.13(c). Note that for the experiments in the wind icing tunnel a power supply enabling up to 40V/40A was used.

The LIRL parameters for this final de-icing experiment, conducted in icing conditions are $T_\infty \approx -5.00$ °C, LWC= 1.20 g/m^3, MVD= 20 μm, and the airspeed is $V_\infty \approx 19$ m/s, with a test time is 19 minutes 48 seconds. Maximum power required is $P \approx 920$ W. These conditions are the least severe icing conditions attainable, by reason of wind icing tunnel facility limitations.

The experiment is initiated in icing conditions. The maximum power available initially is limited to $P \approx 385$ W. The electro-thermal source is activated and the temperature starts to rise as maximum power is supplied. In Figure 9.13(a) this is illustrated by the ice free thermal source (the black part of the leading edge
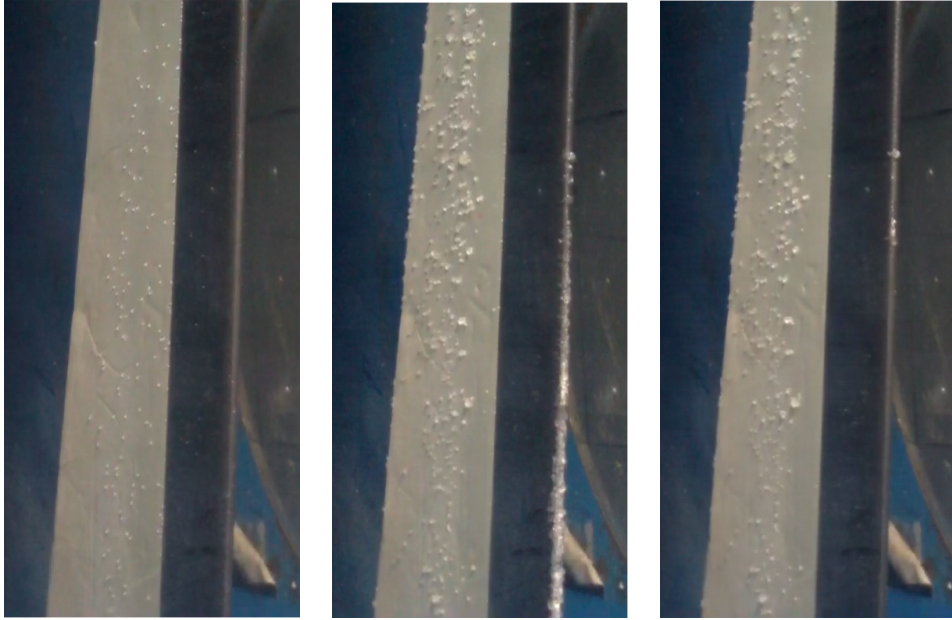
(a) PUMA wing element in icing conditions ($t = 20$ seconds).

(b) PUMA wing element in icing conditions ($t = 19$ minutes).

(c) PUMA wing element in icing conditions ($t = 19$ minutes and 1 second).

Figure 9.13: PUMA platform wing element in *De-Icing* experiment, conducted in icing conditions.

of the wing element) and the droplets that have frozen further back on the wing element. As the experiment progress icing begins to form on the leading edge of the wing element, despite an active electro-thermal source. At this time the available power is increased to $P \approx 690$ W. Still an ice layer on the leading edge of the wing element perseveres. The electro-thermal source is constantly active. At time $t = 18$ minutes 48 seconds available power is increased one final time to $P \approx 920$ W. Figure 9.13(b) display the formation of icing on the wing element 12 seconds after the final available power increase. 1 second later the ice layer on the leading edge of the wing element is shed, see Figure 9.13(b). The temperature measurement of the electro-thermal source read $T_{ETS} = 47.25$ °C at this time.

9.3 Discussion

As expected the icing detection category experiments show a clear distinction between responses from experiments conducted in icing conditions as opposed to ones conducted in non-icing conditions (see Figures 9.7 and 9.8). The distinction reveals itself as a difference in profiles of the electro-thermal source temperature in the two different conditions. More specifically activating the electro-thermal source in non-icing conditions results in a more rapid heating and higher temperature increase, but also a faster decrease in temperature once the electro-thermal source

is deactivated, compared to the experiment conducted in icing conditions. The difference is a result of a change in thermal flux, most likely this can be attributed to the fact that thermal convection (heat flow from the electro-thermal source to the surrounding airflow) in non-icing conditions changes into thermal conduction (heat flow from the electro-thermal source to the ice layer that has formed on the leading edge of the wing element) in icing conditions [67, 69, 70]. It should be noted that other thermal phenomena undoubtedly also influence the change in thermal flux, especially dissipation through impinging supercooled liquid water droplets and thermal gain associated with latent heat of fusion.

Although the distinction between responses experimentally obtained in icing and non-icing conditions are clear, it is interesting to see the difference in these experimentally obtained responses from the ones obtained through simulations, as seen in Section 5.4. As the power consumption for the experiments differ from the simulations a difference in response amplitude is expected, however the thermal time constant also show differences. One hypothesis about these differences could be that the temperature sensor used in the IPS design are slightly larger than the thickness of the electro-thermal source, i.e. the temperature measurements are influenced by the temperature of the wing core. Further, the temperature sensors have been electrically isolated from the electro-thermal source using a specific insulating membrane, hence the temperature measurements are influenced by the thickness of the membrane and the thermal conductance of the membrane material. This hypothesis has been corroborated by simulations, with insulated virtual sensor probes. In future experiments and integration procedures, these possible issues could be addressed by using alternative smaller sensors embedded in the electro-thermal source with greater precision.

The anti-icing experiment conducted in non-icing conditions demonstrates the feasibility of the proposed solution as the temperature of the electro-thermal source is a controllable quantity that can be maintained at a desired set point temperature. However, the anti-icing experiment conducted in icing conditions exposed issues related to power consumption, as the power required to maintain the temperature at the desired set point surpassed the power available.

The issue concerning power consumption is reiterated in the de-icing experiments. For the experiments conducted in non- icing conditions the available power of $P \approx 350$ W is not enough to ensure that the desired set point temperature is reached in the period of electro-thermal source activation, and as is revealed by the de-icing experiments conducted in icing conditions the required power level for successful de-icing is $P \approx 920$ W (7.97 kW/m^2).

From the above discussion it is clear that power consumption is a major concern in the electro-thermal based IPS presented in this monograph. The issue that has been presented here is in fact two different issues, as the anti-icing solution (icing prevention) requires more energy than its de-icing counterpart, as less power for longer periods are needed. Conversely the cornerstone of the de-icing solution (icing mitigation) is rapid heating and requires higher temperatures, hence a requirement for a higher level of power than the anti-icing solution, but for much shorter periods.

Naturally the issue of power requirement could be addressed by simply increasing the power supply. However, this typically entails an increase in payload weight and volume, something that is exceedingly sparse on small UAVs. Another solution

altogether is to alter the area size of the electro-thermal source, as was investigated in Chapter 7.

Another important aspect to be emphasized here is that the temperature of the electro-thermal source, while approximately uniform during any steady ground experiments, is far from uniform in an actual airflow. This is clearly illustrated by the de-icing experiment conducted in icing conditions (see Figures 9.13(a) – 9.13(c)) and indeed by several simulations presented previously in this monograph . Ice builds on the leading edge of the wing element, despite temperature measurements indicating that the electro-thermal source temperature is well above the minimum requirement for icing to shed. Note that the location of the temperature sensor is key in these findings. The issue of non-uniformity opens up for the need to optimise the layout of the electro-thermal source, possibly with a non-uniform profile. Again this corroborates the findings presented in Chapter 7.

Here it is important to clarify that the objective of the experiments conducted and presented in this chapter, have primarily been focused on studying the feasibility of the IPS functionality and that the design criteria of the electro-thermal source layout has not been optimised. Further, the range of atmospheric conditions attainable for the experiments have been greatly limited, as the wind icing tunnel is not designed for the purpose of conducting icing experiments that include small UAVs operating at low airspeeds. Consequently, the power levels required during various experiments can be used as guidelines only for any future wind icing tunnel experiments that might be performed.

9.4   Summary

This chapter has presented findings from experiments conducted in the controlled environment of the wind icing tunnel at the LeClerc Icing Research Laboratory. Three primary categories of experiments have been conducted. These are:

- *icing detection* – The objective with these experiments is to obtain electro-thermal source temperature profiles, evaluated by the electro-thermal-based icing detection algorithm
- *anti-icing* – Validate the anti-icing program routine under specific icing and non-icing atmospheric conditions
- *de-icing* – Demonstrate the feasibility of the de-icing program routine under icing and non-icing conditions

The electro-thermal-based icing detection algorithm require two datasets. The icing detection experiments are conducted to provide these two datasets. The first dataset is obtained in non-icing atmospheric conditions, which serves the purpose of reference, and the second dataset required is obtained in icing conditions. The electro-thermal source temperature profiles needed are induced by a momentary and periodical activation of the electro-thermal source. The activation period for this category of experiments is 10 seconds, which is followed by a 'cool down' period of 50 seconds. The responses of each experiment is displayed in Figures 9.7 and 9.8. The icing detection experiments are conducted on the X8 Skywalker platform. The two electro-thermal source temperature profiles obtained show a clear distinction that indicate icing on the leading edge of the wing element has a large impact. For

the experiment conducted in non-icing conditions the average temperature increase was identified as 1.75 °C from -15.75 °C to -14.00 °C. The average rise time for this increase is 9 seconds, and the average fall time is 21 seconds. Conversely, the experiment conducted in icing conditions results in a temperature profile that reveals an average temperature increase of 0.75 °C from -15.75 °C to -15.00 °C. The average rise time required to achieve this increase is 6 seconds, while the fall time is 26 seconds.

The data obtained in the anti-icing experimental category is used to demonstrate the feasibility of the proposed solution. The objective of the anti-icing program routine is to prevent icing occurrences on the leading edge of wing elements by maintaining the electro-thermal source temperature above freezing. As illustrated in Figure 9.10 the feasibility of the proposed solution has been validated as the program routine achieves its objective. However, once icing conditions are present the power requirement exceeds 340 W, which results in a stable temperature level below the desired set point temperature (see Figure 9.11).

Issues concerning power requirements are reiterated in the de-icing experiments. These issues are displayed clearly in both Figures 9.12 and 9.13(a) – 9.13(c). For the experiment conducted in non-icing conditions the available power is increased to approximately 350 W. This power increase is not sufficient and does not enable the de-icing program routine to achieve its objective. Further it is revealed by the de-icing experiments conducted in icing conditions that the required power level for successful de-icing is approximately 920 W.

One solution to the power requirement issue is to optimise the design layout of the electro-thermal source, possibly with a non-uniform profile.

Chapter 10

Flight Tests

The final step in demonstrating the feasibility of the proposed IPS is to conduct flight tests. The main contribution of this chapter is the presentation of findings obtained from flight tests conducted in Ny-Ålesund, Svalbard, Norway.

The chapter begins with a brief introduction to preliminary test flights conducted in Anchorage, Alaska, in Ny-Ålesund, Svalbard, Norway, and at Udduvoll, Norway. This is followed by the presentation of the main contribution of the chapter, more specifically it will present flight experiments conducted in Ny-Ålesund, Svalbard, Norway. The chapter is concluded by a discussion and a short summary.

Here it should be noted that all preparations regarding the flight tests conducted, i.e. hardware and software development (including testing), integration on all platforms, ground testing (including electromagnetic interference (EMI) testing), any review board documentation, etc., except piloting the aircraft, has been completed by the author himself. Though, it should also be noted that assistance has been provided by NASA engineers, United States Air Force officers, and pilots from NTNU and the United States Air Force.

10.1 Preliminary Flight Tests

To demonstrate the feasibility of the solution concept and to prove airworthiness of the retro-fitted aircraft, several preliminary test flights have been conducted. This section presents some of the processes and outcomes of these preliminary flight tests conducted with the Dragon Eye and X8 Skywalker UAV platforms.

10.1.1 A Worlds First

The preliminary test flights, of the Dragon Eye UAV platform, were the first flights in the world for any IPS for small unmanned fixed-wing aircraft. The flights themselves were preceded by an integration and ground testing process at the UAV laboratory of NASA Ames in California. The integration procedure was presented in a Chapter 8 and will not be repeated here.

Prior to the commencement of any flight tests the aircraft and all additions (such as the IPS) undergo the scrutiny of NASA-Ames' Airworthiness & Flight

Safety Review Board (AFSRB). The board receives documentation on all systems and develop a risk analysis and assessment, which form the basis for the boards recommendation, to fly or not to fly. As the IPS has been developed to be a stand-alone solution, with various fail safe measures (both hardware and software), and as the solution itself does not introduce any aerodynamic alterations of significance to the aircraft, the boards recommendation was positive. Various EMI tests were concluded with positive results, and as such the Dragon Eye, retro-fitted with a clone of the first IPS prototype was ready to be shipped off to a colder state (from California to Alaska).

The experimental site - used for the Dragon Eye preliminary test flights - was made available by courtesy of the United States Air Force and Air Force reserve officer Major Steve Wackowski. The site was Elmendorf Air Force Base, which is a United States military facility in Anchorage, Alaska (see Figure 10.1). The specific airfield used for the experiments presented in this section was located on the outskirts of Elmendorf and was approximately 40 meters wide and 500 meters long. Experiments were conducted here in early April 2015. High risk aircraft icing periods in this region is February – March and September – October.

Figure 10.1: Location of the test site in Alaska, highlighted by the blue circle (◯).

Figure 10.2 show the Dragon Eye retro-fitted with the icing protection system in pre-flight tests. The nose section (lying on top of the main fuselage) serves as payload bay and is the compartment where the control unit and power supply (here in the form of a LIPO battery) is located.

Pre-flight ground tests revealed satisfactory data acquisition and electro-thermal source temperature control, without any incidents. The test flight was conducted in non-icing conditions, but the feasibility of the IPS anti-icing program routine was demonstrated.

10.1.2   A Flying Icing Protection Solution

As one of the primary UAV platform of the NTNU-UAV laboratory the X8 Sky-walker has been subjected to numerous preliminary test flights. In late September 2015 the NTNU-UAV laboratory conducted operations together with the Northern
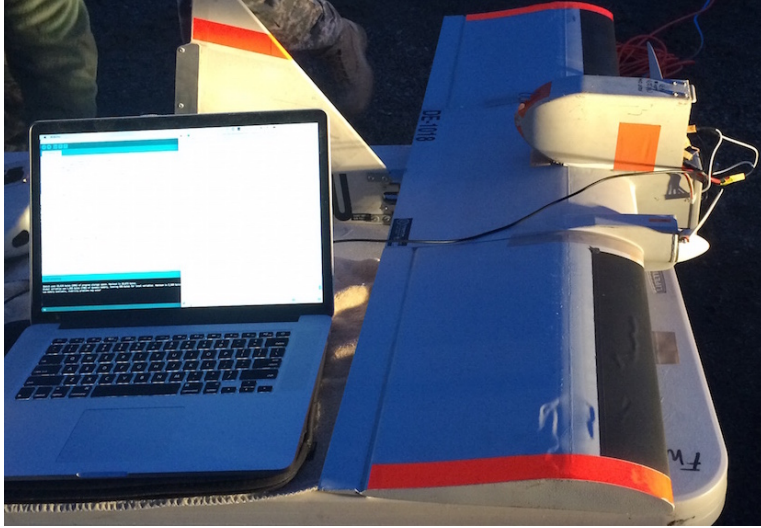
Figure 10.2: Dragon Eye UAV platform with IPS. Preparations for preliminary flight tests.

(a) Location of the test site in Svalbard highlighted by the blue circle (◯).

(b) Location of the test site in mainland Norway highlighted by the blue circle (◯).

Figure 10.3: Maps of Ny-Ålesund and Udduvoll test site locations.

Research Institute (NORUT) in Ny-Ålesund on Svalbard, Norway, and in mid-January 2016 the NTNU-UAV laboratory conducted operations at Udduvoll airfield, located outside Trondheim, Norway. See Figures 10.3(a) and 10.3(b) for maps that depict the test site locations.

The primary objective of these preliminary flight tests were to demonstrate the airworthiness of the solution when integrated onto the X8 Skywalker UAV platform, and to obtain data for various optimisation problems and safeguard investigations.

10.2   Flight Tests at Ny-Ålesund, Svalbard

In April 2016 the X8 Skywalker - equipped with the IPS - was brought back to Ny-Ålesund, Svalbard, Norway, to conduct multiple test flights. The objectives were to asses the icing-detection, de-icing and anti-icing program routines, and to obtain electro-thermal source temperature data from several sensors at various locations on the wing.

10.2.1   Test Flights Preliminaries

Three different tests were conducted, with multiple objectives. The three tests can be categorised as follows.

- *icing detection* – The objective of this test flight was twofold. One was the purpose of validating the icing detection data collection program routine. The other was to obtain data from multiple temperature sensors - located at various chord line lengths on the aerofoil - used to assess the non-uniformity of the temperature distribution during the activation icing detection program routine.

- *de-icing* – This test flight had the primary purpose of validating the de-icing program routine.

- *anti-icing* – The objective of this test flight was identical to that of the above de-icing program routine, conducted for the anti-icing program routine.

The three program routines are described in Chapter 6 and will not be repeated here.

It should be noted that the X8 Skywalker platform was retro-fitted with an electro-thermal source on both wings. However, due to an increasing focus on power consumption and electro-thermal source temperature profiles it was deemed reasonable to use all available power on just one wing for proof-of-concept study. All flights were conducted in non-icing conditions, as such this decision was not an issue.

For the purpose of assessing electro-thermal source temperature distribution in the longitudinal flight direction, temperature sensors were embedded at various chord line lengths on the aerofoil, as illustrated in Figure 10.4. The sensor used for feedback control is denoted T_{ETS}, aside from this, sensors were embedded 'atop' approximately 40 mm from the leading edge of the aerofoil, one wa s located on the very leading edge, and finally a sensor was embedded 'under' approximately 20 mm from the leading edge of the aerofoil.

Peak power supplied to the electro-thermal source was approximately 450 W and average airspeed was 17 m/s.

10.2.2   Test Flights - Results

The responses from the three test flights presented in this chapter can be found in Figures 10.5 − 10.7.

The icing detection program routine was activated three times, at three different altitudes, during the icing detection test flight. Five temperature sensor
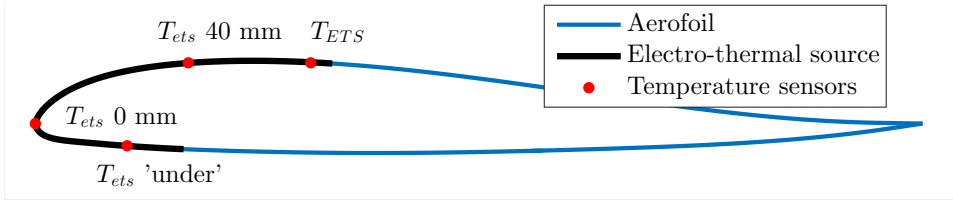
Figure 10.4: Sensor locations on the X8 Skywalker wing used during the Svalbard April 2016 flight tests.

responses were collected from sensors located as specified in Figure 10.4 and from the atmospheric sensor mounted on the main fuselage.

Figure 10.5: Responses from the icing detection program routine test flights in Ny-Ålesund, Svalbard, in April 2016.

The electro-thermal source temperature responses clearly display the expected and desired evolution of a rapid temperature increase, when the electro-thermal source is activated, and decrease, when it is de-activated. It's interesting to note the modest temperature increase of the sensor located at the very leading edge (T_{ets} 0 mm), even though approximately 450 W was supplied to the electro-thermal source.

109

This temperature profile, and the clear non-uniformity of the thermal distribution in the electro-thermal source, corresponds well with the response obtained through simulations for the electro-thermal-based icing detection algorithm presented in Chapter 5 and the findings presented in the thermodynamic analyses found in Chapter 7. It is also evident when closely investigating the response of the sensor used for feedback control (T_{ETS}) that the location of this particular sensor is sub-optimal as the temperature settles very slowly at equilibrium in periods when the electro-thermal source is de-activated.

Responses for the de-icing test flight were obtained at a an altitude of approximately 300 m, with an average airspeed of 17 m/s. The de-icing program routine was operated with a desired set point temperature of $+20°$C. Maximum available power was approximately 450W.

Figure 10.6: Responses from the de-icing program routine test flights in Ny-Ålesund, Svalbard, in April 2016.

The responses displayed in Figure 10.6 obtained during the de-icing test flights show that the power supplied to the electro-thermal source is not adequate to reach the desired set point temperature. One of the strengths of the de-icing approach is a relatively low energy consumption, despite a higher requirement for immediate power. This strength is undermined by the lack of power and the duration of the activation sequence of the electro-thermal source (as exemplified by the responses in

Figure 10.6), i.e. the 'on' period should be reduced and power increased for optimal de-icing functionality. Comparing the responses from all the electro-thermal source temperature sensors the pattern indicating a non-uniform temperature distribution in and over the electro-thermal source is maintained. Another thing to note is the initial responses (the initial spikes) of the T_{ets} group of sensors, when the electro-thermal source is activated. One explanation to this pattern deviating behaviour could be that this group of sensors are located on top of the surface of the electro-thermal source (i.e. they were fitted after the initial retro-fit), as opposed to the sensor used for feedback control, which is embedded in the electro-thermal source.

The anti-icing test flight responses were obtained under conditions similar to the ones described for the de-icing test flights, except for the desired set point temperature, which for the anti-icing test flight was set to $+5°C$. The initial power consumption needed to reach the desired set-point temperature was approximately 450W. Once the set-point was reached power consumption settled at approximately 210W. The anti-icing program routine was deliberately terminated after 300 seconds as a precaution to ensure that the limitations of the power source were not exceeded.

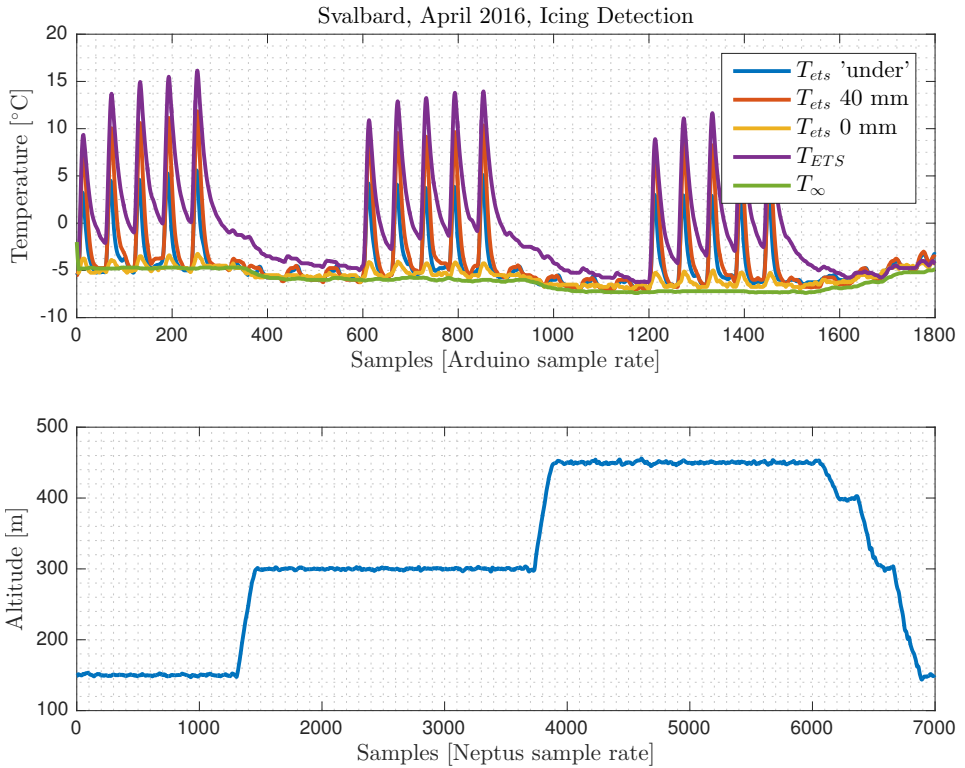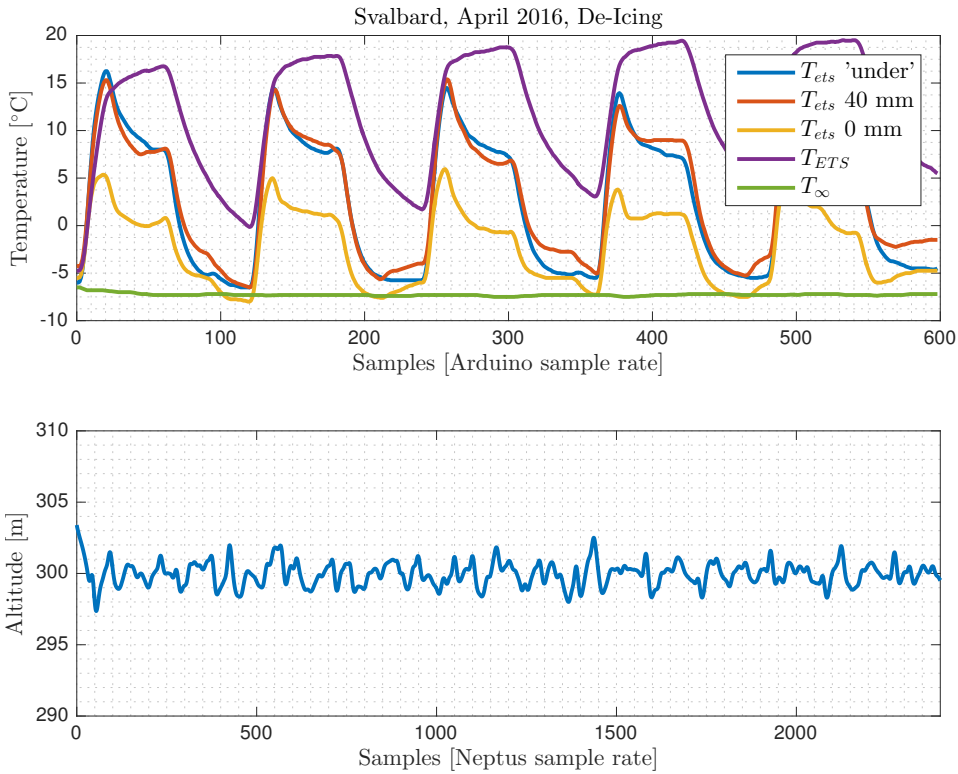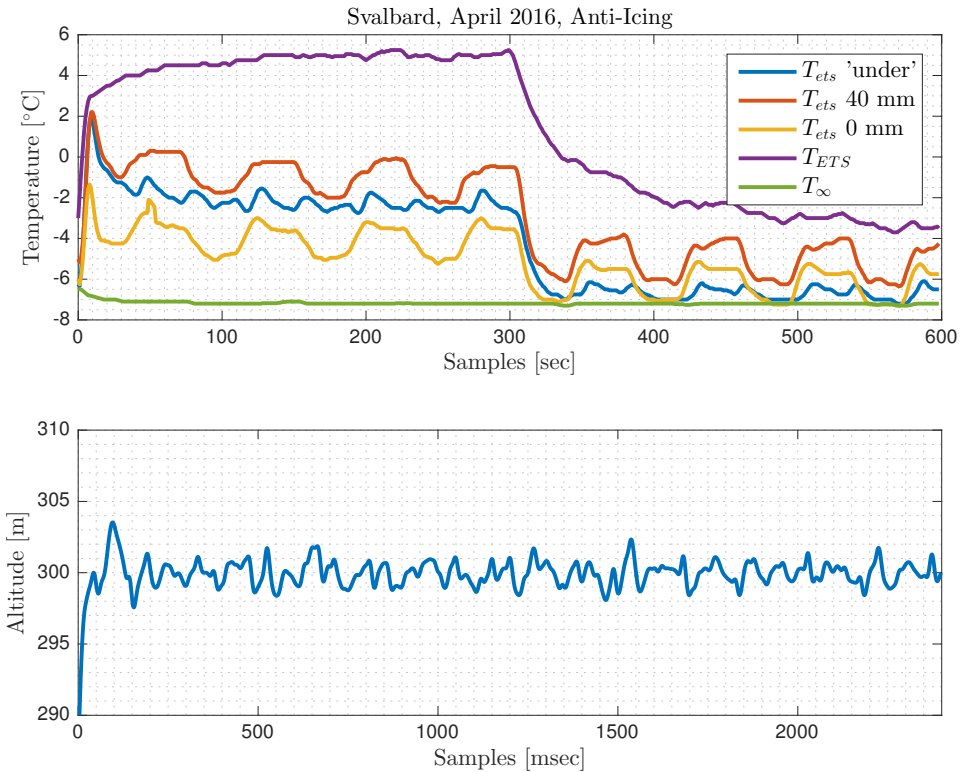
Figure 10.7: Responses from the anti-icing program routine test flights in Ny-Ålesund, Svalbard, in April 2016.

The temperature responses displayed in Figure 10.7 were obtained during the

anti-icing test flight. The temperature sensor used for feedback control (T_{ETS}) clearly shows how the objective of maintaining the desired set point temperature is achieved, thereby demonstrating the feasibility of the anti-icing program routine. Investigating the responses of the sensor group denoted T_{ets}, the non-uniformity of the electro-thermal source temperature distribution once again becomes apparent. The relative periodic decreases/increases seen in the responses of the two T_{ets} sensors located 'atop' of the aerofoil can be attributed to a directional change of the aircraft.

10.3   Summary

This chapter has presented findings from preliminary flight tests conducted at several locations around the world, and primary test flights conducted in Ny-Ålesund, Svalbard, Norway. All test flights was conducted in non-icing conditions. Three categories of the primary test flights have been conducted. These are:

- *icing detection* – The objective with these experiments is to obtain electro-thermal source temperature profiles, required by the elector-thermal-based icing detection algorithm.

- *anti-icing* – The objective with the anti-icing program routine experiments was to demonstrate its feasibility in specific icing and non-icing atmospheric conditions

- *de-icing* – The objective with the de-icing program routine experiments was identical to the anti-icing experiments, i.e. to demonstrate the feasibility of the de-icing program routine

Due to the integration of several extra temperature sensors strategically located around the leading edge of the wing, temperature responses were obtained that once again highlighted the non-uniformity of the thermal distribution over the electro-thermal source. These results corroborate the findings presented in Chapter 7. The Responses also validated that the control algorithms achieve their objective for each of the three categories of the primary test flights (i.e. icing detection, anti-icing, and de-icing).

Something worth noting in the icing detection program routine test flights, is the little impact of the imposed altitude variations on the temperature profiles obtained (see the responses from Figure 10.5). This result indicates that altitude variations, consequently ambient temperature variations, have little influence on the electro-thermal source temperature profiles when obtaining data for the electro-thermal-based icing detection algorithm.

Chapter 11

Conclusion and Future Work

This chapter provides the main conclusions inferred based on the work presented in this monograph. Further, the chapter includes a listing of possible avenues for future work.

11.1 Conclusion

The main objective of the Ph.D. project presented in this monograph has been to develop a prototype of an intelligent system that will be able to mitigate or altogether prevent icing from forming on exposed unmanned aircraft surfaces, thereby enabling safe and robust UAV operations regardless of atmospheric conditions. Icing is one of the most hazardous weather phenomenons to all of aviation, causing altered flight plans, potentially loss of control, and in extreme scenarios loss of the aircraft.

Developing an IPS for unmanned aircraft required deriving, analysing, simulating, and testing of novel models, methods, and algorithms. This monograph contains several individual contributions and it is the complete IPS concept for unmanned aircraft that is the main contribution of the work presented herein. The contributions are listed here in order of appearance.

11.1.1 Icing Protection Solution Architecture

Chapter 3 provides a description of the modular architecture of the proposed IPS. Aside from being the first system of its kind for small fixed-wing UAVs it also sets itself apart from existing systems, especially systems for conventional aircraft, as icing is prevented or mitigated autonomously.

The architecture proposed enables for autonomous on-line and in-flight icing detection, mitigation, or prevention, ensuring safe and robust UAV operations regardless of harsh atmospheric conditions. The application of two fundamentally different icing detection algorithms has been chosen to enhance robustness, where further development will be focused on increasing their operational spectrum, thereby expanding the flight envelope covered. The modular architecture of the proposed

icing protection solution itself enables for a generic design applicable to a wide range of platforms.

The architecture proposed here is one of the main contributions in [76]

11.1.2 Model-Based Icing Detection Algorithm

In Chapter 4 the model-based icing detection algorithm is presented. The proposed algorithm addresses the issue of icing on exposed aircraft surfaces by casting it in a fault diagnosis framework, applying the non-linear longitudinal model of an aircraft to diagnose wing surface changes (or faults), i.e. unexpected aerodynamic changes, inferred by icing occurrences.

The algorithm relies on estimates of aerodynamic parameters - obtained under nominal flight conditions and used as reference - and the non-linear model of the aircraft. Any unexpected change in these parameters and a wing surface fault is said to have occurred, hence icing is forming on exposed aircraft surfaces, and the algorithm raises an alert.

The proposed algorithm displays promising detection capabilities for both residuals generated. For the test statistics for the residual primarily concerned with lift force icing penalties ($T_{r_2}(\mathbf{x})$), numerical analyses demonstrate a 99% probability of detection inside 2 seconds, with a negligible probability of raising a false alarm for imposed icing penalties, quantified as a 10% decrease in lift and a 10% increase in drag. The test statistics for the other residual ($T_{r_1}(\mathbf{x})$), concerned with drag force penalties, numerical analyses reveal a 97% probability of detection, but requires 10 seconds to detect the fault. The probability of raising a false alarm for the imposed icing penalties is again negligible. The algorithm should be robust to a large flight envelope. However, issues arising as a result of possible correlated noise and measures to address these, such as pre-whitening, necessitate further investigation.

To enhance robustness of the proposed algorithm a combination of the two residuals could be an interesting avenue for further development. Other such avenues, could include expanding the fault diagnosis array to also encompass pitot-tube icing, icing penalties experienced by the engine, though a decrease in thrust and airspeed, etc.

The proposed algorithm has been presented in [75], published in the fall of 2015.

11.1.3 Electro-Thermal-Based Icing Detection Algorithm

In Chapter 5 a second novel approach to icing detection is presented. This approach has been designated the electro-thermal-based icing detection algorithm, as it uses the electro-thermal source actively to achieve its objective. As the model-based icing detection algorithm so does the electro-thermal-based icing detection algorithm cast the issue in a fault diagnosis framework. However, where the prior is based on the non-linear model of an aircraft the latter employs a thermodynamic system comprised of the electro-thermal source, the core structure of the aircraft, and atmospheric conditions.

The proposed algorithm requires an electro-thermal source control pattern that allows for rapid and short temperature increases of said source, enabling the detection algorithm to obtain estimates of wing surface temperature gradients (one

for each wing). For reference these gradients are estimated under nominal flight conditions. If these temperature gradients change unexpectedly a fault is said to have occurred and the algorithm produces an alert signal.

Through simulations this novel icing detection approach display promising results, with residual responses clearly illustrating occurrences of icing. Due to time constraints the algorithm is at an early developmental stage and therefore detection strategies (thresholding, parameter estimation, etc.) is yet to be formalised.

The constraints that assumptions regarding atmospheric conditions impose on the proposed algorithm, need further analysis, as they could limit the flight envelope for feasible icing detection.

The algorithm proposed here is presented in [79] and one serves as one of the main contributions in [76].

11.1.4 Control Unit

Chapter 6 provides a presentation of the central control unit of the developed IPS, which consists of both hardware and software systems.

Microcomputers, active components, sensors, and PCBs comprise the hardware, and icing detection algorithms, various data collection and processing algorithms, and temperature control algorithms, make up the software.

Design objectives have been listed and achieved through the development of a PCB that serves as a connectivity and data gathering hub for various sensors, a data collection component, a microcomputer, electro-thermal sources, and the power source.

Several control procedures represent the purpose of the control unit. These procedures rely on the control algorithm generating appropriate PWM signals to two transistors, the enable power control and consequently temperature control of the electro-thermal source.

The current IPS design does not include any dedicated autonomous decision algorithm, to decide which of the two control strategies to employ. This decision is presently user specified (pre-flight) and should be based on; weather forecasts; operational area, altitude, and objectives. An autonomous control strategy decision algorithm, could enable for dynamic icing prevention and mitigation, enabling for adaptive IPS power requirements during certain flight patterns.

The collective work of the central control unit serves as a contributing part to [76].

11.1.5 Thermodynamic Analyses

Chapter 7 is a presentation of a proof-of-concept study based on analyses of the thermodynamic system comprised of an aircraft wing, an electro-thermal source, and the surrounding airflow. The analyses are based on numerical simulations applying a transient finite element approach to account for the multidimensional boundary conditions that vary along the chord of a specific aerofoil.

When aircraft operations occur in non-icing conditions the aforementioned thermodynamic system is in thermal equilibrium. However, if ambient conditions change and the aircraft suddenly operate in potential icing conditions the IPS will

drive the thermodynamic system out of equilibrium by increasing the temperature of the electro-thermal source. The analyses presented are conducted to investigate the thermal heat transfer and temperature profiles when the electro-thermal source is activated in a virtual flight environment. Special attention is granted to the developed hypothesis that there exists an inverse proportionality between electro-thermal source area size and power consumption, where several simulations are conducted to verify the hypothesis.

The findings presented in this chapter highlight the intricate nature of the thermodynamics relating to an electro-thermal source on the leading edge of an aircraft wing, which again emphasise the importance of temperature sensor locations and the significant impact caused by electro-thermal layout and aerofoil design.

The work related to the thermodynamic analyses is presented [80], and serve as an extension to the published work found in [77].

11.1.6   Integration Procedures

Appropriate integration procedures are a necessity to accommodate specific UAV platforms, while abiding by flight readiness and airworthiness requirements. Chapter 8 provides a presentation of this very topic

The process of integrating the IPS is specific to each platform UAV. This chapter begins with a presentation of the integration procedures that have been developed to accommodate the structural design of each specific platform, while ensuring that the IPS performs as required. Aside from this the chapter includes an introduction to various test sites used for preliminary test flights and a presentation of some of the obtained results.

Some of the results presented in this monograph indicate that the location of the temperature sensors, embedded in the wings, should be prioritised, likewise should the electro-thermal layout. Weight penalties imposed by the integration of the IPS onto the platforms is an issue that could be addressed by further developments to the prototype, where the introduction of small satellite units, one for each wing, and a smaller, lighter central control unit, could be an avenue to pursue. The present architecture includes one large central control unit, where all data, power and processing is collected, transferred, controlled, and completed. Another avenue to be investigated for future prototypes is IPS power requirements, how these requirements impact the overall performance of the aircraft (given an IPS dependence on an aircraft engine power supply), and how this can be mitigated through intelligent IPS design considerations.

The integration procedures and results obtained have not previously been published.

11.1.7   Wind Icing Tunnel Experiments

Chapter 9 presents findings from wind icing tunnel experiments of the developed IPS, integrated onto several test bed UAV platforms.

The chapter includes an introduction to the test facility, a presentation of the preceding work required, including the development of mounting units and an extensive test plan. Results include electro-thermal source temperature responses

from experiments conducted for the purpose of evaluating the icing detection, de-icing, and anti-icing program routines and demonstrating their feasibilities, in both non-icing and icing conditions.

The test matrix (range of icing relevant parameter values) was limited by the functional constraints of the wind icing tunnel, hence icing conditions were limited to varying degrees of severity above what is generally recognised as very severe icing conditions ($T_\infty \leq -5°\text{C}$, LWC ≥ 1.2 g/m^3, and MVD ≥ 20 μm).

The distinction between responses experimentally obtained in icing and non-icing conditions are clear, however, it is worth noting that the difference in the experimentally obtained responses from the ones obtained through simulations. Amplitude differences were expected as the power consumption for the experiments differ from the simulations, however the thermal time constant also display differences. A hypothesis regarding these, could be that the temperature sensor used in the IPS design are slightly larger than the thickness of the electro-thermal source, i.e. the temperature measurements are influenced by the temperature of the wing core. Further, the temperature sensors have been electrically isolated from the electro-thermal source using a specific insulating membrane, hence the temperature measurements are influenced by the thickness of the membrane and the thermal conductance of the membrane material. This hypothesis has been corroborated by simulations, with insulated virtual sensor probes. In future experiments and integration procedures, these possible issues could be addressed by using alternative smaller sensors embedded in the electro-thermal source with greater precision.

For the de-icing category experiments the desired set temperature $T_{set} = 10$ °C, which is identified as the minimum surface temperature required to shed ice layers in [31], could prove insufficient under various circumstances. The reason for this is that shedding the ice layer is a consequence of aerodynamic forces driven primarily by the airspeed, where the work presented in [31] is focussed on large conventional aircraft wing elements, with airspeeds limited to approximately 78 m/s, well outside the cruise airspeeds of the small UAV platforms used for the work presented in this monograph. However, experimental results have show that shedding was achieved, where the measured temperature was $T_{ETS} = 47.25°\text{C}$. Here it is important to stress that the temperature distribution over the electro-thermal source is non-uniform and large temperature differences over the leading edge of wings have been presented, combined with the location of the sensor obtaining the specific temperature measurement for T_{ETS}, it is likely that the temperature at the very leading edge of the electro-thermal source (and wing), at the time of ice shedding, was within the temperature range presented in [31] for de-icing.

Anti-icing experiments conducted in non-icing conditions successfully demonstrated the ability of the system to maintain electro-thermal source temperatures at a desired set temperature. Experiments conducted in icing conditions revealed similar results, although the desired set temperature was not maintained, a stable temperature was achieved, indicating that the anti-icing routine operates as needed when enough power is available.

The work presented in this chapter has not previously been published.

11.1.8 Flight Tests

Chapter 10 provides a presentation of - and findings from - flight tests conducted in various location around the World. As the flights presented are a World-first for an IPS on any small fixed-wing UAV platform, they are significant in demonstrating the feasibility of the complete icing protection solution. The responses from flight tests corroborate the findings from simulations and experiments conducted prior, and they show that the proposed solution, given enough available power and energy, will be able to achieve the objectives set out. The flight tests also revealed a non-uniformity in the temperature distribution through the electro-thermal source, once again corroborating the findings from prior simulation studies. This revelation indicate a need to focus on sensor location and electro-thermal source layout, as design optimisation strategies are being formalised.

Flight tests from Ny-Ålesund in Svalbard, conducted in April 2016, were completed in non-icing conditions, where results obtained display a system that operates as expected.

A particularly interesting result from the icing detection test flights, was the little impact of the imposed altitude variations had on the temperature profiles obtained. These can be found in Figure 10.5). This would indicate that changes in altitude, even rapid ones, which result in ambient temperature variations, have very little influence on the electro-thermal source temperature profiles when obtaining data for the electro-thermal-based icing detection algorithm.

The work presented in this chapter has not previously been published.

11.1.9 Concluding Remarks in a Larger Perspective

The work presented in this monograph is related to the development of a prototype for an intelligent IPS for small unmanned aircraft. Contributions range from system architecture, through specific icing detection solutions, control strategies, thermodynamic analyses, integration procedure development, proof-of-concept studies, includes wind icing tunnel experiments and flight tests.

The developed IPS has the potential to become an enabling technology in the UAV industry that have experienced a rapid growth in the last decade. However, integrating the IPS onto UAV platforms includes certain penalties, i.e. added weight and energy consumption. These penalties influence platform capabilities, hence operational range. Added weight limits payload capacity and therefore options, especially so for small UAV platforms, where operations typically include scientific monitoring, search and rescue, and reconnaissance, all of which require one or more on-board cameras. If the IPS is dependant upon power supplied by the aircraft engine power supply, endurance suffers, greatly limiting the operational airspace. Other considerations required, related to IPS integration, is the retrofit solution currently employed, as opposed to an embedded solution, where the electro-thermal source, temperature sensors, and all wires and cables are added in the production phase of any given UAV platform. The retro-fit solution includes adding a surface material (the electro-thermal source) to only parts of the aircraft wings. This material, although relatively smooth, adds a different texture to the surface that will influence the airflow over a wing. Routing wires and cables in the

wings, post production, will influence the structural integrity of the aircraft wings somewhat. These issues and the penalties mentioned could implicate any attempts at achieving airworthiness certification. Further, a retro-fit solution includes man-hour expenses as each platform requires the integration to be performed manually. An embedded solution would, to an extent, address these issues; as the electro-thermal source would be embedded underneath the skin of the aircraft; wire and cable routing would be optimised to suit the design of any specific platform; and finally, integration could, most likely, be performed autonomously.

The IPS is a feasible solution for small UAV platforms and will enable the industry to expand into application areas otherwise inaccessible. With efforts to further develop, optimise the design and implementation of the IPS, the solution could become an integral part of future aircraft design

11.2 Future Work

The time to complete a Ph.D. is limited, and many aspects of a viable icing protection solution could not be completed in the time allotted. As such, there are several avenues that are open to further research. The following is a listing of some possibilities.

- The model-based icing detection algorithm should be verified against experimental data.

- The same algorithm could be expanded to include other icing induced faults, such as pitot-tube, control surfaces, stabilisers, etc. And indeed it could be expanded to include non-icing faults, enabling robust UAV performance, not only in harsh atmospheric conditions, but in general.

- The electro-thermal-based icing detection algorithm should also be verified against experimental data.

- Further thermodynamic analyses are required and the simulation environment should be expanded to 3-dimensional space to investigate electro-thermal source layout optimisation (power consumption minimisation).

- The protective regions of the aircraft should be increased to also mitigate possible runback water/icing.

- Optimal layout design of the electro-thermal source, possibly with non-uniform thickness and size.

- Optimising IPS operations and performance, i.e. activation thresholds, adaptive temperature set-points, etc.

- Investigating aircraft performance penalties for optimised IPS dependant on power supplied from aircraft engine.

- Introduce icing forecasting into the solution for autonomous control strategy decision algorithm.

- Investigate embedded IPS design potential

- Optimise IPS design, i.e. better sensors, investigate other electro-thermal source materials, lighter design with optimised central control unit and possible satellite power units, etc.

References

[1] Farzaneh M, editor. Atmospheric Icing of Power Networks. 1st ed. Springer Publishing Company, Incorporated; 2008.

[2] Sankar LN, Ali M. In: In-Cloud Ice Accretion Modeling on Wind Turbine Blades Using an Extended Messinger Model. American Institute of Aeronautics and Astronautics; 2015. .

[3] Rosenfeld D, Woodley WL. Deep convective clouds with sustained super-cooled liquid water down to -37.5°C. Nature. 2000;405(05):440–442.

[4] Politovich MK. Aircraft icing caused by large supercooled droplets. Journal of Applied Meteorology. 1989;28(9):856–868.

[5] Battisti L. Wind Turbines in Cold Climates. 1st ed. Springer Publishing Company, Incorporated; 2015.

[6] Fikke SM, Kristjánsson JE, Nygaard BEK. Modern meteorology and atmospheric icing. In: Atmospheric Icing of Power Networks. Springer; 2008. p. 1–29.

[7] Bernstein BC, Wolff CA, McDonough F. An inferred climatology of icing conditions aloft, including supercooled large drops. Part I: Canada and the continental United States. Journal of Applied Meteorology and Climatology. 2007;46(11):1857–1878.

[8] Bernstein BC, Le Bot C. An inferred climatology of icing conditions aloft, including supercooled large drops. part II: Europe, Asia, and the Globe. Journal of Applied Meteorology and Climatology. 2009;48(8):1503–1526.

[9] Siquig R. Impact of icing on unmanned aerial vehicle (UAV) operations. DTIC Document; 1990.

[10] Lewis W, Kline DB, Steinmetz CP. A further investigation of the meteorological conditions conducive to aircraft icing. National Advisory Committee for Aeronautics. Ames Aeronautical Lab.; Moffett Field, CA, United States; 1947.

[11] Lewis W. A flight investigation of the meteorological conditions conducive to the formation of ice on airplanes. National Advisory Committee for Aeronautics. Ames Aeronautical Lab.; Moffett Field, CA, United States; 1947.

[12] Hacker PT, Dorsch RG. A Summary of Meteorological Conditions Associated with Aircraft Icing and a Proposed Method of Selecting Design Criterions for Ice-Protection Equipment. Lewis Flight Propulsion Laboratory; Cleveland, Ohio, United States; 1951.

[13] Hansman RJ, Breuer KS, Hazan D, Reehorst A, Vargas M. In: Close-up Analysis of Aircraft Ice Accretion. American Institute of Aeronautics and Astronautics; 1993. .

[14] Gent RW, Dart NP, Cansdale JT. Aircraft icing. Philosophical Transactions of the Royal Society of London A: Mathematical, Physical and Engineering Sciences. 2000;358(1776):2873–2911.

[15] Bernstein BC, Omeron TA, McDonough F, Politovich MK. The Relationship between Aircraft Icing and Synoptic-Scale Weather Conditions. Weather and Forecasting. 1997;12(4):742–762.

[16] Jacob EN. Airfoil section characteristics as affected by protuberances. National Advisory Committee for Aeronautics. Langley Aeronautical Lab.; 1934.

[17] Jones R, Williams DH. Effect of surface roughness on characteristics of aerofoils N.A.C.A. 0012 and R.A.F. 34. A.R.C. Technical Report. Defense Technical Information Center; 1936.

[18] Gulick BG. Effects of simulated ice formation on the aerodynamic characteristics of an airfoil. National Advisory Committee for Aeronautics. Langley Aeronautical Lab.; 1938.

[19] Harold E Addy J. Ice Accretions and Icing Effects for Modern Airfoils. United States Department of Transportation and National Aeronautics and Space Administration (NASA), Glenn Research Center; 2000.

[20] Lynch FT, Khodadoust A. Effects of ice accretions on aircraft aerodynamics. Progress in Aerospace Sciences. 2001;37(8):669–767.

[21] Whitlock C. When Drones Fall From the Sky. The Washington Post; 2014. http://www.washingtonpost.com/sf/investigative/2014/06/20/when-drones-fall-from-the-sky/.

[22] Marwitz J, Politovich M, Bernstein B, Ralph F, Neiman P, Ashenden R, et al. Meteorological Conditions Associated with the ATR72 Aircraft Accident near Roselawn, Indiana, on 31 October 1994. Bulletin of the American Meteorological Society. 1997;78(1):41–52.

[23] Appiah-Kubi P. U.S Inflight Icing Accidents and Incidents, 2006 to 2010.. University of Tennessee. Knoxville, Tennessee, USA; 2011.

[24] Green S. A Study of U.S. Inflight Icing Accidents and Incidents, 1978 to 2002. American Institute of Aeronautics and Astronautics; 2006.

[25] Bragg M, Hutchison T, Merret J. In: Effect of ice accretion on aircraft flight dynamics. American Institute of Aeronautics and Astronautics; 2000. .

[26] Beard RW, McLain TW. Small Unmanned Aircraft - Theory and Practice. Princeton University Press; 2012.

[27] Rutherford RB, Dudman RL, inventors; Zoned aircraft de-icing system and method. ; 2001. US Patent 6,237,874.

[28] Rutherford RB, inventor; De-ice and anti-ice system and method for aircraft surfaces. ; 2001. US Patent 6,194,685.

[29] Rauch P, Bauchet JC, inventors; Resistive Elements for Heating an Aerofoil, and Device for Heating an Aerofoil Incorporating such Elements. ; 1999. US Patent 5,971,323.

[30] Gray VH. Prediction of Aerodynamic Penalties Caused by Ice Formations on Various Airfoils. National Aeronautics and Space Administration, United States; 1964.

[31] Lewis BJP, Bowden DT. Preliminary Investigation of Cyclic De-Icing of an Airfoil Using an External Electric Heater. National Advisory Committee for Aeronautics. Ames Aeronautical Lab.; Moffett Field, CA, United States; 1952.

[32] Al-Khalil KM, Ferguson TFW, inventors; Hybrid ice protection system for use on roughness-sensitive airfoils. ; 2001. US Patent 6,196,500.

[33] Buschhorn ST, Kessler SS, Lachmann N, Gavin J, Thomas G, Wardle BL. In: Electrothermal Icing protection of Aerosurfaces Using Conductive Polymer Nanocomposites. American Institute of Aeronautics and Astronautics; 2013. .

[34] Hastings OH, Hastings OM, inventors; Electrically conductive laminate for temperature control of aircraft surface. ; 1994. US Patent 5,344,696.

[35] Heintz AM, Christiaen AC, Vijayendran BR, Elhard JD, Lalgudi RS, Robbins WB, et al., inventors; Electrically conductive coating composition. ; 2013. US Patent 8,581,158.

[36] Pourbagian M, Habashi WG. Aero-thermal optimization of in-flight electrothermal ice protection systems in transient de-icing mode. International Journal of Heat and Fluid Flow. 2015;54:167–182.

[37] Gohardani O. Impact of erosion testing aspects on current and future flight conditions. Progress in Aerospace Sciences. 2011;47(4):280 – 303.

[38] Caliskan F, Hajiyev C. A review of in-flight detection and identification of aircraft icing and reconfigurable control. Progress in Aerospace Sciences. 2013;60:12–34.

[39] Tousi MM, Khorasani K. Fault diagnosis and recovery from structural failures (icing) in unmanned aerial vehicles. In: 3rd Annual IEEE Systems Conference; 2009. p. 302–307.

[40] Tousi MM, Khorasani K. Robust observer-based fault diagnosis for an un-manned aerial vehicle. In: IEEE International Systems Conference (SysCon); 2011. p. 428–434.

[41] Cristafaro A, Johansen TA, Aguiar AP. Icing Detection and Identification for Unmanned Aerial Vehicles: Multiple Model Adaptive Estimation. In: European Control Conference; 2015. .

[42] Seron MM, Johansen TA, Doná JAD, Cristofaro A. Detection and estimation of icing in unmanned aerial vehicles using a bank of unknown input observers. In: 5th Australian Control Conference (AUCC); 2015. p. 87–92.

[43] Rotondo D, Cristofaro A, Johansen TA, Nejjari F, Puig V. Icing detection in unmanned aerial vehicles with longitudinal motion using an LPV unknown input observer. In: 2015 IEEE Conference on Control Applications (CCA); 2015. p. 984–989.

[44] Cristafaro A, Johansen TA. An unknown input observer approach to icing detection for unmanned aerial vehicles with linearized longitudinal motion. In: American Control Conference; 2015. .

[45] Rotondo D, Cristofaro A, Johansen TA, Nejjari F, Puig V. Detection of icing and actuators faults in the longitudinal dynamics of small UAVs using an LPV proportional integral unknown input observer. In: 3rd International Conference on Control and Fault-Tolerant Systems; 2016. .

[46] Cristofaro A, Johansen TA. An unknown input observer based control allo-cation scheme for icing diagnosis and accommodation in overactuated UAVs. In: European Control Conference; 2016. .

[47] Research on inflight parameter identification and icing location detection of the aircraft. Aerospace Science and Technology. 2013;29"(1):305 – 312.

[48] Kessler SS, Dunn CT, Wicks SS, de Villoria RG, Wardle BL. Carbon Nan-otubes (CNT) Enhancements for Aerosurface State Awareness. In: 8th Inter-national Workshop on Structural Health Monitoring; 2011. .

[49] Zhang YM, Jiang J. Active fault-tolerant control system against partial actuator failures. IEE Proceedings on Control Theory and Applications. 2002;149:95 – 104.

[50] Zhang Y, Suresh VS, Jiang B, Theilliol D. Reconfigurable Control Alloca-tion against Aircraft Control Effector Failures. In: 2007 IEEE International Conference on Control Applications; 2007. p. 1197–1202.

[51] Bateman F, Noura H, Ouladsine M. Actuators Fault Diagnosis and Toler-ant Control for an Unmanned Aerial Vehicle. In: 2007 IEEE International Conference on Control Applications; 2007. p. 1061 – 1066.

[52] Hansen S, Blanke M, Adrian J. A Framework for Diagnosis of Critical Faults in Unmanned Aerial Vehicles. IFAC Proceedings Volumes. 2014;47(3):10555 – 10561.

[53] Hansen S, Blanke M. Diagnosis of Airspeed Measurement Faults for Unmanned Aerial Vehicles. IEEE Transactions of Aerospace and Electronic Systems. 2013 April;.

[54] Sørensen KL, Helland AS, Johansen TA. Carbon nanomaterial-based wing temperature control system for in-flight anti-icing and de-icing of unmanned aerial vehicles. In: IEEE Aerospace Conference; 2015. .

[55] Denbigh KG. The Principles of Chemical Equilibrium. 1st ed. Cambridge University Press; 1957.

[56] IV JHL, V JHL. A Heat Transfer Textbook. Phlogiston Press; 2015.

[57] Incropera F. Introduction to heat transfer. Wiley; 2007.

[58] Welty JR, Wicks CE, Wilson RE, Rorrer GL. Fundamentals of Momentum, Heat, and Mass Transfer. 5th ed. John Wiley & Sons, Inc; 2007.

[59] Kothandaraman CP. Fundamentals of Heat and Mass Transfer. 3rd ed. New Age International Limited, Publishers; 2006.

[60] Kondepudi D. Introduction to Modern Thermodynamics. 1st ed. John Wiley & Sons, Inc; 2008.

[61] Siegel R. Thermal radiation heat transfer. Taylor & Francis; 2002.

[62] Fermi E. Thermodynamics. Dover Publications; 1936.

[63] Geankoplis C. Transport Processes and Separation Process Principles (Includes Unit Operations) Fourth Edition. 4th ed. Prentice Hall Press; 2003.

[64] Rogers D. Laminar flow analysis. Cambridge University Press; 1992.

[65] Lian Y, Shyy W. Laminar-Turbulent Transition of a Low Reynolds Number Rigid or Flexible Airfoil. AIAA Journal. 2007;45(7):1501–1513.

[66] Bergrun NR, Jukoff D, Schlaff BA, Neel J Carr B. The Calculation of the Heat Required for Wing Thermal Ice Prevention in Specified Icing Conditions. National Advisory Committee for Aeronautics. Ames Aeronautical Lab.; Moffett Field, CA, United States; 1947.

[67] Messinger BL. Equilibrium Temperature of an Unheated Icing Surface as a Function of Air Speed. Journal of the Aeronautical Sciences. 1953;20(1):29–42.

[68] Bragg MB, Broeren AP, Blumenthal LA. Iced-airfoil aerodynamics. Progress in Aerospace Sciences. 2005;41(5):323–362.

[69] Myers TG. Extension to the Messinger Model for Aircraft Icing. AIAA Journal. 2001;39(2):211–218.

[70] Özgen S, Canıbek M. Ice accretion simulation on multi-element airfoils using extended Messinger model. Heat and Mass Transfer. 2008;45(3):305–322.

[71] Cansdale JT, Gent RW. Ice Accretion on aerofoils in two-dimensional compressible: A Theoretical Model. Royal Aircraft Establishment; 1983.

[72] Hardy JK. An Analysis of the Dissipation of Heat in Conditions of Icing From a Section of the Wing of the C-46 Airplane. National Advisory Committee for Aeronautics. Ames Aeronautical Lab.; Moffett Field, CA, United States; 1945.

[73] Gelder TF, Lewis JP. Comparison of Heat Transfer from Airfoil in Natural and Simulated Icing Conditions. National Advisory Committee for Aeronautics, Lewis Flight Propulsion Laboratory, United States; 1951.

[74] Lowe PR. An Approximating Polynomial for the Computation of Saturation Vapor Pressure. Journal of Applied Meteorology. 1977 January;16(1776):100–102.

[75] Sørensen KL, Blanke M, Johansen TA. Diagnosis of Wing Icing Through Lift and Drag Coefficient Change Detection for Small Unmanned Aircraft. In: IFAC Workshop Series; 2015. p. 541–546.

[76] Sørensen KL, Johansen TA, Borup KT, inventors; Icing Control System. ; 2016. GB Patent 1614339.8.

[77] Sørensen KL, Johansen TA. Thermodynamics of a Carbon Nano-Materials Based Icing Protection System for Unmanned Aerial Vehicle. In: IEEE Aerospace Conference; 2016. .

[78] Johansen TA, Cristofaro A, Sørensen KL, Hansen JM, Fossen TI. On estimation of wind velocity, angle-of-attack and sideslip angle of small uavs using standard sensors. In: International Conference on Unmanned Aircraft Systems (ICUAS); 2015. p. 510–519.

[79] Sørensen KL, Johansen TA. Electro-Thermal Icing Detection for Small Unmanned Aircraft. IEEE Transactions on Aerospace and Electronic Systems. 2016;.

[80] Sørensen KL, Johansen TA. Thermodynamic Analyses of Electro-Thermal Anti-Icing System for Small Unmanned Aircraft. AIAA Journal of Aircraft. 2016;.

[81] Thompson G, Bruintjes RT, Brown BG, Hage F. Intercomparison of In-Flight Icing Algorithms. Part I: WISP94 Real-Time Icing Prediction and Evaluation Program. Weather and Forecasting. 1997;12(4):878–889.

[82] Korolev A, Isaac GA. Relative Humidity in Liquid, Mixed-Phase, and Ice Clouds. Journal of the Atmospheric Sciences. 2006;63(11):2865–2880.

[83] Schultz P, Politovich MK. Toward the Improvement of Aircraft-Icing Forecasts for the Continental United States. Weather and Forecasting. 1992;7(3):491–500.

[84] Bernstein BC, McDonough F, Politovich MK, Brown BG, Ratvasky TP, Miller DR, et al. Current Icing Potential: Algorithm Description and Comparison with Aircraft Observations. Journal of Applied Meteorology. 2005;44(7):969–986.

[85] Wenz AW, Johansen TA, Cristofaro A. Combining model-free and model-based Angle of Attack estimation for small fixed-wing UAVs using a standard sensor suite. In: International Conference on Unmanned Aircraft Systems; 2016. .

[86] Wenz AW, Johansen TA. Icing detection for small fixed wing UAVs using inflight aerodynamic coefficient estimation. In: IEEE Multi-Conference on Systems and Control; 2016. .

[87] Borup KT, Fossen TI, Johansen TA. A Nonlinear Model-Based Wind Velocity Observer for Unmanned Aerial Vehicles. In: 10th IFAC Symposium on Nonlinear Control Systems; 2016. .

[88] Long H, Song S. Method of Estimating Angle-of-Attack and Sideslip Angel Based on Data Fusion. In: Intelligent Computation Technology and Automation, 2009. ICICTA '09. Second International Conference on. vol. 1; 2009. p. 641–644.

[89] Stevens BL, Lewis FL. Aircraft Control and Simulation. Wiley; 2003.

[90] Blanke M, Lorentzen T. SaTool - a Software Tool for Structural Analysis of Complex Automation Systems. In: Proceedings of the 6. IFAC Symposium on Fault Detection, Supervision and Safety of Technical Processes. Elsevier Science; 2006. p. 673–678.

[91] Kay SM. Fundamentals of Statistical Signal Processing: Detection theory. Prentice Hall Signal Processing Series. Prentice-Hall PTR; 1998.

[92] Blanke M, Lorentzen T. SaTool - a Software Tool for Structural Analysis of Complex Automation Systems. In: Proceedings of the 6. IFAC Symposium on Fault Detection, Supervision and Safety of Technical Processes. Elsevier Science; 2006. p. 673–678.

[93] Langelaan JW, Alley N, Neidhoefer J. Wind Field Estimation for Small Unmanned Aerial Vehicles. Journal of Guidance, Control, and Dynamics. 2011;34(4):1016–1030.

[94] Galeazzi R, Blanke M, Poulsen NK. Early Detection of Parametric Roll Resonance on Container Ships. Control Systems Technology, IEEE Transactions on. 2013 March;21(2):489–503.

[95] Smith AG, Spalding DB. Heat Transfer in a Laminar Boundary Layer with Constant Fluid Properties and Constant Wall Temperature. Journal of the Royal Aeronautical Society. 1958 1;62:60–64.

[96]   Sun Z, Zhu C, Fu B, Zhu C. Study on thermodynamic characteristics of ice-layer accretion for airfoils. Heat and Mass Transfer. 2012;48(3):427–438.

[97]   Rodríguez-Pérez MA, Alonso O, Souto J, de Saja JA. Thermal conductivity of physically crosslinked closed cell polyolefin foams. Polymer Testing. 1997;16(3):287 – 298.

[98]   1 C. Heat Transfer Module User's Guide; 2015. Available from: http://www.ewp.rpi.edu/hartford/~collir5/MP/OTHER/Reference/ HeatTransferModuleUsersGuide.pdf.

[99]   Al-Khalil K, Salamon L, Tenison G. Development of the Cox Icing Research Facility. In: 36th AIAA Aerospace Sciences Meeting and Exhibit. American Institute of Aeronautics and Astronautics; 1998. .

[100] Ellrod GP, Bailey AA. Assessment of Aircraft Icing Potential and Maximum Icing Altitude from Geostationary Meteorological Satellite Data. Weather and Forecasting. 2007;22(1):160–174.

[101] Cober SG, Isaac GA, Strapp WJ. Characterizations of aircraft icing environments that include supercooled large drops. Journal of Applied Meteorology. 2001;40(11):1984–2002.

[102] Bernstein BC, Omeron TA, Politovich MK, McDonough F. Surface weather features associated with freezing precipitation and severe in-flight aircraft icing. Atmospheric Research. 1998;46(1–2):57 – 73.

[103] Levine WS. The Control Handbook. 2nd ed. CRC Press; 2010.